ELASTIC SCATTERING OF LONGITUDINALLY POLARIZED ELECTRONS FROM ^{4}He

A measurement of G_E^s at $Q^2 = 0.1$ (GeV/c)^2

A Dissertation

Presented to

The Faculty of the Department of Physics

The College of William and Mary in Virginia

In Partial Fulfillment

Of the Requirements for the Degree of

Doctor of Philosophy

---

by

Bryan J. Moffit

2007

APPROVAL SHEET

This dissertation is submitted in partial fulfillment of

the requirements for the degree of

Doctor of Philosophy

Bryan J. Moffit

Approved, April 2007

David S. Armstrong, Chair

Todd D. Averett

Robert E. Welsh

Robert W. Michaels, Staff Scientist
Thomas Jefferson National Accelerator Facility

Mark Pitt, Professor
Virginia Polytechnic Institute and State University

To my wife, my mother, and my father.

TABLE OF CONTENTS

Acknowledgements

My interest in physics began with the excellent teaching and inspiration from Bill Dillon and Gary Holbrook at Horizon High School in Scottsdale, AZ. This catapulted me into college, where I was fortunate to learn from the outstanding and knowledgeable professors in the Physics Department of Arizona State University. Specifically, I would like to thank David Benin, Peter Bennett, Richard Jacobs, Barry Ritchie, Otto Sankey, and Kevin Schmidt.

While at ASU, I received much academic and emotional support from my friends and colleagues in the Society of Physics Students. From the all-night studying/homework sessions, to the mellowing Friday nights spent at the local bars, there is no way I would have gotten through my undergraduate life without the time spent with these people. I also need to thank them for encouraging me to date one of the Physics Department secretaries, who eventually became my wife.

When I moved on to the College of William and Mary, I met several other graduate students who helped make me feel at home in Williamsburg, VA. I would like to thank Kevin Kramer, Paul King, Dan Steiner, Keoki Seu, Bill Brower, Justin Conroy, Herry Johnny, Sarah Phillips, Josh Moss, Wendy Vogan, Vince Sulkosky and others for friendship and for the great times we spent together. While taking classes, in the Physics Department, I was fortunate to learn from several inspiring professors (just to mention a few: Carl Carlson, Dirk Walecka and Shiwei Zhang). A special thanks goes to Paula, Diane, and Sylvia for taking care of the administrative portion of my graduate stay at William and Mary.

My graduate work was performed at Jefferson Lab with David Armstrong as my research and thesis supervisor. I would like to thank David for his practical knowledge of physics, his enthusiastic attitude, and helpful guidance throughout this research. A broader thanks goes to the 2004 HAPPEx Collaboration (listed in Appendix A) for everything between taking shifts to analyzing the data. Specifically, I would like to thank the spokespersons and main decision-makers for the experiments: Gordon Cates, Krishna Kumar, David Lhuillier, Bob Michaels, Kent Paschke, and Paul Souder. Much of the planning and the analysis effort for the experiments was lead by Kent. I thank Kent for guiding me through the easy and tough portions of these experiments and for reading and correcting this thesis.

I would like to thank my fellow PhD students Lisa Kaufman, Ryan Snyder, and Hachemi Benaoum for their help in the experiment preparation and the analysis effort. My appreciation goes to the professional and outstanding work provided by the Hall A technical staff. As well as an extended thanks to the JLab Electronics Group for versing me on the fine art of soldering and cable crimping.

My deepest gratitude goes to Bryan G. Moffit, Shelby Saussol, Stephen Mueller, to my brother Zachary Mueller, to all of my relatives, and to Michele and Lydia for everything they have done for me. I also thank Michele for the love and understanding that helped carry me through the writing of this thesis.

LIST OF TABLES

LIST OF FIGURES

ABSTRACT

We have performed the first measurement of the parity-violating asymmetry in the elastic scattering of longitudinally polarized electrons from ^{4}He. The kinematics chosen ($Q^2 = 0.1$ (GeV/c)^2) provide a direct sensitivity to the strange electric form factor G_E^s with negligible contributions from competing effects. This experiment was performed in June 2004 and July-September 2005 in Hall A at Jefferson Lab. This work represents the experimental setup and analysis of the 2004 dataset.

The final statistical precision, from the combined datasets, put stringent requirements on the systematic errors that normalize the asymmetry (e.g. Q^2, beam polarization, backgrounds). The experimental and analysis techniques, presented in this thesis, resulted in a 12.9% relative measure of the parity-violating asymmetry for the 2004 dataset, and a 4.1% relative measure for the 2005 dataset (the most precise measurement of a parity-violating asymmetry ever obtained).

The 2004 measured result, $A^{PV} = 6.72 \pm 0.84$ (stat) ± 0.21 (syst) ppm, allows for the extraction of the electric strange form factor: $G_E^s(Q^2 = 0.1) = -0.038 \pm 0.042$ (stat) ± 0.010 (syst). When combined with results from previous experiments, at nearly the same kinematics, a clear picture of the contribution of strange quarks to the nucleon's electric and magnetic form factors emerges.

CHAPTER 1

Introduction

The internal structure of the nucleon has been the subject of much study over the past century, beginning with the discovery of the larger than expected proton and neutron magnetic moment in the 1930s [1, 2]. More evidence was provided by the first measured proton cross section from electron scattering [3], indicating that the nucleon had a definite finite size (Figure 1.1).

Since then, with the emergence of Quantum Chromodynamics (QCD), the nucleon is described as being a composite object. Specifically, the proton is understood as being made up of three valence quarks [two up (u) quarks, and one down (d) quark]. Interactions between these quarks are mediated by gluons, describing what is understood as the "strong" force, in the family of universal forces.

Within the fields of the quarks and the gluons, arises the possibility of the pair production of quark and anti-quark pairs ($\bar{q}q$). These so-called "sea quarks", in principle, are pairs of quarks of all flavors (u, d, c, s, b, t). Because the strange quark (s) mass ($m_s \approx 0.1$ GeV/c^2) is on the same order as the scale of the strong interaction, it is reasonable to assume that they may have non-negligible contributions to the nucleon properties. Thus, experiments that isolate these *strange* components to

the nucleon provide a low-energy probe of the nucleon sea.

In this paper, we motivate the search for strange sea quarks by first exploring the experimental hints of their contributions to the nucleon's momentum, spin, and mass. We then investigate the possibility of contributions to the nucleon's electric and magnetic properties through derivation of the parity violating asymmetry from elastic scattering of longitudinally polarized electrons from an unpolarized target.

With the theoretical result in hand, we describe the HAPPEx-^{4}He experiment: an ambitious Jefferson Laboratory experiment to perform the first measurement of the parity violating asymmetry from the ^{4}He nucleus. Details of the analysis of the obtained data will be presented, followed by the extraction of the strange electric form factor (G_E^s). Finally, this result will be put into context with other strange form factor measurements, and compared to recent theoretical predictions.

1.1 Experimental Hints

1.1.1 Deep Inelastic Neutrino Scattering

Perhaps the most direct method of measuring the quark content of the nucleon utilizes deep inelastic lepton scattering. From the measurement of the deep inelastic cross section, parton distribution functions (PDFs) are extracted. These functions $f(x, Q^2)$ are interpreted as the probability density for finding a particle with a certain longitudinal momentum fraction x and four-momentum transfer squared Q^2.

Measurement of individual quark PDFs is aided by the charged-current exchange in neutrino and anti-neutrino interactions. Interactions with strange quarks are obtained from the two dominant processes [4]:

$$\nu_\mu + s \rightarrow \mu^- + c$$

$$\overline{\nu}_\mu + \overline{s} \rightarrow \mu^+ + \overline{c}$$

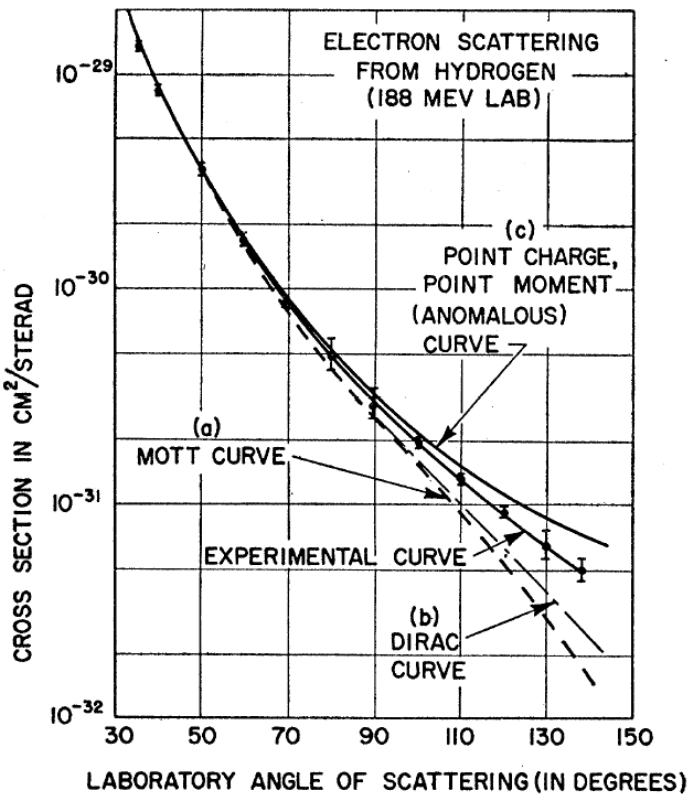

FIG. 1.1: Electron scattering cross-section of the proton as a function of laboratory scattering angle.

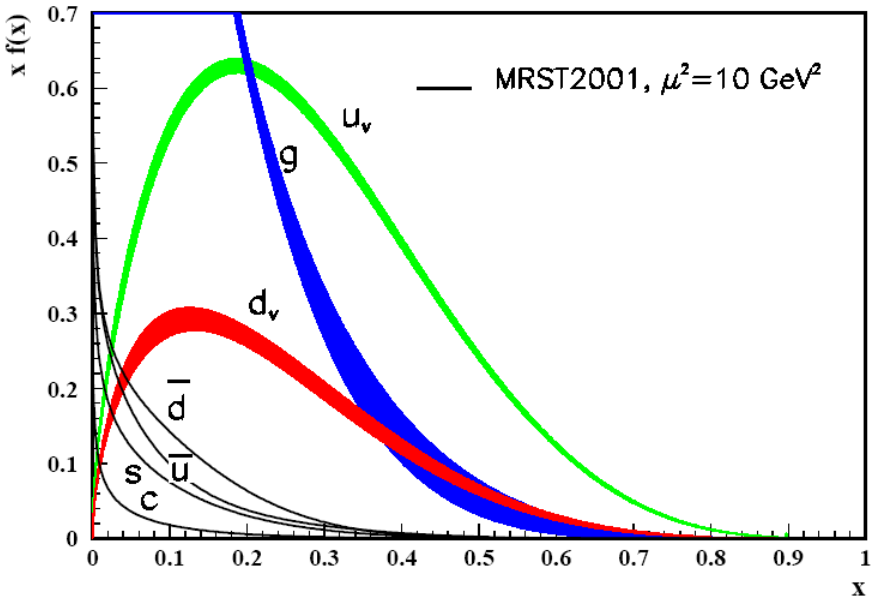

FIG. 1.2: x times unpolarized parton distribution functions versus x using the MRST2004 parameterization [5].

with the charm decay products of $\mu^+\mu^-$ pairs providing the signal of the reaction. Measurements of $f(x)$ (where $f = u, d, \bar{u}, \bar{d}, s, c, g$) have been made over large kinematic ranges of fixed target and collider experiments. Global analyses are performed in an attempt to summarize these data. An example parameterization from Ref. [5] is shown in Figure 1.2. These results indicate that $s(x)$ and $\bar{s}(x)$ are significant at low x, and that strange quarks carry roughly 2% of the nucleon's momentum.

1.1.2 Strangeness and Nucleon Spin

The spin structure of the nucleon is probed by polarized deep inelastic lepton scattering from polarized nucleon targets. Inclusive scattering, with this method, allows for extraction of the spin-dependent nucleon structure function g_1

$$g_1(x, Q^2) = \frac{1}{2} \sum_{q=u,d,s,..} e_q^2 \Delta q(x, Q^2), \tag{1.1}$$

where $\Delta q(x, Q^2)$ is a polarized PDF. Measurement of g_1 over a large kinematic range (as was done by the SMC Collaboration [6]) then allows one to evaluate the sum

rule

$$\begin{aligned}\int_0^1 g_1(x)dx &= \frac{1}{2}\sum_q e_q^2 \int_0^1 \Delta q(x)dx \\ &= \frac{1}{2}\left[\frac{4}{9}\Delta u + \frac{1}{9}\Delta d + \frac{1}{9}\Delta s\right].\end{aligned} \tag{1.2}$$

Extrapolation is used to estimate the behavior of g_1 at very low x, however results indicate that Δs may be negative with a value between 0 and -0.2 [7].

1.1.3 Strangeness in $\Sigma_{\pi N}$

Pion-nucleon scattering is of interest when looking for strange quarks in the nucleon because of its sensitivity to extract the so-called sigma-term. The pion-nucleon sigma-term is a measure of chiral symmetry breaking in QCD and is defined as [8]

$$\sigma(t=0) = \frac{\hat{m}}{2m}\langle p|\bar{u}u + \bar{d}d|p\rangle, \qquad \hat{m} = \frac{1}{2}(m_u + m_d), \tag{1.3}$$

where $t = (p' - p)^2$. This value is obtained from experiment by first obtaining the isoscalar π-N scattering amplitude extrapolated to the Cheng-Dashen point $\Sigma_{\pi N}(q^2 = 2m_\pi^2)$. This value is then extrapolated to $q^2 = 0$ using model-dependent input. In the absence of strange quarks,

$$\Sigma_{\pi N}(0) = \sigma_0 \tag{1.4}$$

where σ_0 is Equation 1.3 calculated with $SU(3)$ corrections. Deviations from the predicted value of σ_0 and the extrapolated experimental value of $\Sigma_{\pi N}$ are attributed to a contribution of $\bar{s}s$ pairs to the nucleonic mass from the strange scalar current $\langle p|\bar{s}s|p\rangle$.

An analysis of the vast πN scattering database has been performed [9], indicating that as much as 200 MeV of the nucleon mass is attributed to strange quarks. Uncertainty in this value due to extrapolation is large, as well as concern in the relationship between $\Sigma_{\pi N}$ and nucleon strangeness, which decreases the confidence in this result.

1.1.4 Strangeness and Vector Form Factors

Considerable attention, in the last decade, has been focused on the strange vector and axial-vector matrix elements. Simplistically, these quantities contribute to the distributions of charge and magnetization of the nucleon. A practical method for measuring these strange matrix elements involves the use of neutral weak interactions. Several experimental programs have dedicated themselves to measuring this process (detailed in Chapter 4).

For inclusive elastic scattering of longitudinally polarized electrons from an unpolarized nucleon, the scattering cross section may be written in terms of the electromagnetic (γ) and neutral weak (Z) scattering amplitudes ($\mathcal{M}$):

$$\sigma_i = |\mathcal{M}^{\gamma} + \mathcal{M}_i^{Z}|^2, \tag{1.5}$$

where $i = R, L$ indicates the right- or left-handedness of the incident electron helicity. The right-left asymmetry from these cross sections simplifies to

$$\begin{aligned} A_{RL} &= \frac{\sigma_R - \sigma_L}{\sigma_R + \sigma_L} \\ &= \frac{|\mathcal{M}^{\gamma} + \mathcal{M}_R^{Z}|^2 - |\mathcal{M}^{\gamma} + \mathcal{M}_L^{Z}|^2}{|\mathcal{M}^{\gamma} + \mathcal{M}_R^{Z}|^2 + |\mathcal{M}^{\gamma} + \mathcal{M}_L^{Z}|^2} \\ &\approx \frac{|\mathcal{M}^{Z}|}{|\mathcal{M}^{\gamma}|} \approx \frac{Q^2}{M_Z^2}, \end{aligned} \tag{1.6}$$

where Q^2 is the 4-momentum transfer squared, and M_Z is the mass of the Z^0 boson. The resulting asymmetry, parity-violating from the electroweak interference, is on the order of 10 ppm for the kinematical region of interest ($0.1\ (\mathrm{GeV/c})^2 \leq Q^2 \leq 1.0\ (\mathrm{GeV/c})^2$). The next section will derive this asymmetry in detail and how extraction of strange contributions is made.

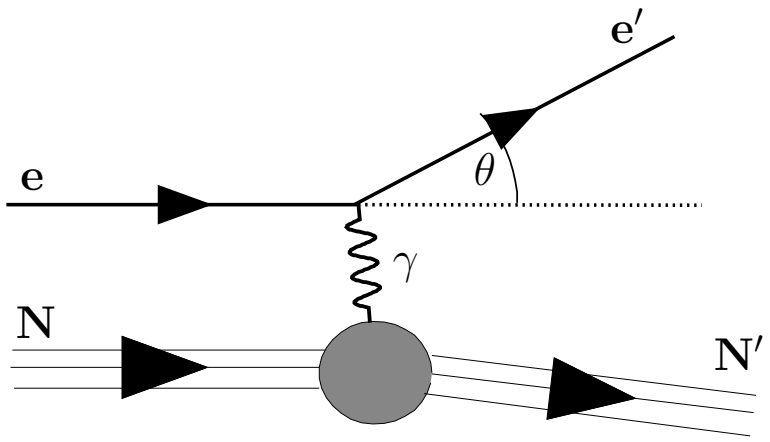

FIG. 1.3: Kinematics for electron scattering from a nucleon target with one photon exchange.

1.2 Theoretical Motivation

Electron scattering experiments probe the structure of the electromagnetic and weak neutral currents. The neutral current amplitude (mediated by the exchange of the Z^0) is several orders of magnitude smaller than the photon-exchange amplitude and is usually ignored.

The differential cross section for the process in Figure 1.3 is written in terms of a scattering matrix T_{fi} [10]

$$d\sigma = 2\pi|\overline{T_{fi}}|^2\delta(W_f - W_i)\frac{d^3k'}{(2\pi)^3}\left[\frac{\sqrt{(k\cdot p)^2}}{EE_p}\right]^{-1}, \tag{1.7}$$

where the kinematic quantities are defined in Table 1.2, W_f, W_i are the final and initial total energies. T_{fi} is determined by considering the contributing diagrams, in Figure 1.4, for the photon and Z_0 exchange. Using the standard model feynman rules,

$$\begin{aligned} T_{fi} = \quad & \frac{4\pi\alpha}{q^2}\Big\{ i\bar{u}(k')\gamma_\mu u(k)\langle p'|J^\gamma_\mu(0)|p\rangle \\ & -\frac{G_F q^2}{4\pi\alpha\sqrt{2}} i\bar{u}(k')\gamma_\mu(a+b\gamma_5)u(k)\langle p'|\mathcal{J}^Z_\mu(0)|p\rangle\Big\}, \end{aligned} \tag{1.8}$$

where, in the standard model

$$a = -(1 - 4\sin^2\theta_W) \tag{1.9a}$$

Parameter	Expression	Description
k	$(E, \vec{k})$	incident electron 4-momentum
k'	$(E', \vec{k}')$	scattered electron 4-momentum
p	$(E_p, \vec{p})$	initial target 4-momentum
p'	$(E'_p, \vec{p}')$	scattered target 4-momentum
$\vec{q}$	$(\vec{k} - \vec{k}')$	3-momentum transfer
ν,ω	$(E - E')$	energy transfer
Q^2	$\omega^2 - q^2$	4-momentum transfer squared

TABLE 1.1: Kinematic variables for the process in Figure 1.3.

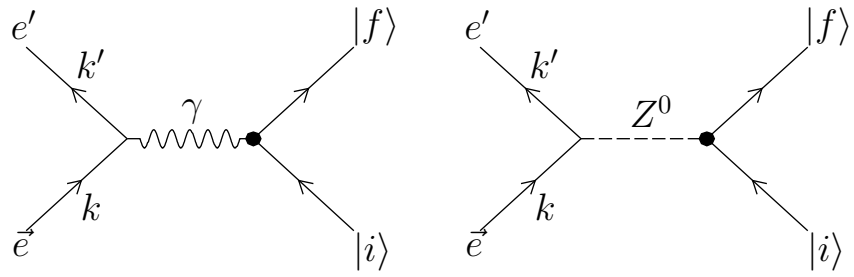

FIG. 1.4: Contributing feynman diagrams for electron scattering.

$$b = -1. \tag{1.9b}$$

$J^{\gamma}_{\mu}(0)$ and $\mathcal{J}^{Z}_{\mu}(0)$ are the electromagnetic and neutral weak hadronic currents evaluated at the interaction point. The special character $\mathcal{J}^{Z}_{\mu}$ is used to emphasize that the neutral weak current has a vector and axial-vector component (i.e. $\mathcal{J}^{Z}_{\mu} = J^{Z}_{\mu} + J^{Z}_{\mu 5}$). The ratio $-G_F q^2/4\pi\alpha\sqrt{2}$ sets the characteristic scale of the electro-weak amplitude.

In this section, we will begin with the usual treatment of ignoring the neutral weak portion of T_{fi} and derive the electromagnetic differential cross section for unpolarized electrons scattering from a nucleon. This derivation will then be extended to nuclear targets ($A \geq 1$). Finally, we return to Equation 1.8 and include the neutral weak current in the context of deriving the parity-violating asymmetry using longitudinally polarized electrons.

1.2.1 Electron-Nucleon Scattering

The form of Equation 1.8 provides the ability to separate the leptonic and hadronic contributions in the form of tensors, $\eta_{\mu\nu}$ and $W_{\mu\nu}$ respectively. The electromagnetic cross section can then be written as

$$d\sigma = \frac{4\alpha^2}{q^4}\frac{d^3k'}{2E'}\frac{1}{\sqrt{(k\cdot p)^2}}\eta_{\mu\nu}W^{\mu\nu}. \tag{1.10}$$

where the leptonic tensor and hadronic tensor are calculated for an unpolarized beam and target as

$$\begin{aligned}\eta_{\mu\nu} &= -2EE'\frac{1}{2}\sum_s\sum_{s'}\bar{u}(k)\gamma_\nu u(k')\bar{u}(k')\gamma_\mu u(k) \\ &= k_\mu k'_\nu + k_\nu k'_\mu - (k\cdot k')\delta_{\mu\nu}\end{aligned} \tag{1.11a}$$

$$W_{\mu\nu} = (2\pi)^3\overline{\sum_i}\sum_f E_p\delta^{(4)}(q+p'+p)\langle p|J^\gamma_\nu(0)|p'\rangle\langle p'|J^\gamma_\mu(0)|p\rangle. \tag{1.11b}$$

For scattering to discrete states these are typically expressed in terms of form factors. For a single nucleon target ($J^\pi = \frac{1}{2}^+$), the matrix elements of the current are given in a general form

$$\langle p'|J^\gamma_\mu(0)|p\rangle = \bar{u}(p')\left[F_1^\gamma(Q^2)\gamma_\mu + i\frac{F_2^\gamma(Q^2)}{2M_T}\sigma_{\mu\nu}q^\nu\right]u(p), \tag{1.12}$$

where $F^\gamma_{1(2)}$ are the electromagnetic Dirac and Pauli form factors of the nucleon. The usual procedure is to use the Sachs [11] form factors defined in terms of the Dirac and Pauli vector form factors:

$$G_E^\gamma(Q^2) = F_1^\gamma(Q^2) - \tau F_2^\gamma(Q^2) \tag{1.13a}$$

$$G_M^\gamma(Q^2) = F_1^\gamma(Q^2) + F_2^\gamma(Q^2), \tag{1.13b}$$

where $\tau = Q^2/4M^2$.

Contracting the leptonic and hadronic tensors from Equation 1.11, the differential cross section for unpolarized elastic scattering from a $J^\pi = \frac{1}{2}^+$ target in the

lab frame is written

$$\left(\frac{d\sigma}{d\Omega}\right)^{\rm EM}_{\rm unpol} = \sigma_M \left[\frac{(G_E^\gamma)^2 + \tau(G_M^\gamma)^2}{1+\tau} + 2\tau(G_M^\gamma)^2 \tan^2\frac{\theta}{2}\right], \tag{1.14}$$

or more compactly,

$$\left(\frac{d\sigma}{d\Omega}\right)^{\rm EM}_{\rm unpol} = \sigma_M \frac{\epsilon(G_E^\gamma)^2 + \tau(G_M^\gamma)^2}{\epsilon(1+\tau)}, \tag{1.15}$$

where $\epsilon = \left[1 + 2(1+\tau)\tan^2\frac{\theta}{2}\right]^{-1}$ and

$$\sigma_M = \frac{E'}{E}\frac{4\alpha^2 E'^2}{Q^4}. \tag{1.16}$$

The electromagnetic vector form factors for the proton and neutron are known experimentally, to varying degrees of accuracy, over a wide range of Q^2 [12] and are typically summarized using the Galster parameterization [13]

$$G_E^p = G_D^v \tag{1.17a}$$

$$G_E^n = -\mu_n \tau G_D^v \xi_n \tag{1.17b}$$

$$G_M^p = \mu_p G_D^v \tag{1.17c}$$

$$G_M^n = \mu_n G_D^v, \tag{1.17d}$$

where

$$G_D^v = (1 - Q^2/M_v^2)^{-2} = (1 + \lambda_D^v \tau)^{-2} \tag{1.18a}$$

$$\xi_n = (1 + \lambda_n \tau)^{-1}, \tag{1.18b}$$

$\mu_p = 2.79,\ \mu_n = -1.91$ are the magnetic moments of the proton and neutron, with $\lambda_D^v = 4.97$ and $\lambda_n = 5.6$. Other recent parameterizations include a phenomenological fit [14] and a "simple" fit using polynomials [15].

1.2.2 Electron-Nucleus Scattering

A general form for the cross section to allow for transitions to discrete states is obtained by performing a multipole analysis. Much detail on this can be found

in Ref [10, 16, 17]. The procedure is to expand the hadronic currents in terms of multipole projections of the charge and three-current operators. To begin, the spatial dependence is restored

$$|\langle f|J^{\gamma}_{\mu}(0)|i\rangle|^2 \rightarrow |\langle f| \int e^{-i\mathbf{q}\cdot\mathbf{x}} J^{\gamma}_{\mu}(\mathbf{x}) d^3x |i\rangle|^2. \tag{1.19}$$

This provides the charge density operator $\hat{\rho}(\mathbf{x})$ for $\mu = \nu = 0$. Insertion of spherical unit vectors, which for $\lambda = \pm 1$ satisfy

$$\begin{aligned} \mathbf{e}_{\mathbf{q}\lambda} \cdot \mathbf{e}^{\dagger}_{\mathbf{q}\lambda} &= 1 \\ \mathbf{e}^{\dagger}_{\mathbf{q}\cdot\lambda} \cdot \mathbf{q} &= 0, \end{aligned} \tag{1.20}$$

provides the three-current operator $\hat{\mathbf{J}}(\mathbf{x})$ (for $\mu, \nu = 1, 2, 3$)

$$|\langle f|J_{\mu}(0)|i\rangle|^2 \rightarrow \sum_{\lambda=\pm 1} |\langle f| \int e^{-i\mathbf{q}\cdot\mathbf{x}} \mathbf{e}^{\dagger}_{\mathbf{q}\lambda} \cdot \hat{\mathbf{J}}(\mathbf{x}) d^3x |i\rangle|^2. \tag{1.21}$$

The plane waves ($e^{i\mathbf{q}\cdot\mathbf{x}}$) are expanded in terms of spherical Bessel functions and spherical harmonics, resulting in the differential cross section in terms of nuclear matrix elements [16]:

$$\begin{aligned} \frac{d\sigma}{d\Omega} = \frac{4\pi\sigma_{\mathrm{M}}}{2J_i+1} \Bigg\{ & v_L \sum_{J=0}^{\infty} |\langle J_f \| \hat{M}^{\mathrm{coul}}_J(q) \| J_i \rangle|^2 \\ & + v_T \sum_{J=1}^{\infty} \left(|\langle J_f \| \hat{T}^{\mathrm{el}}_J(q) \| J_i \rangle|^2 + |\langle J_f \| \hat{T}^{\mathrm{mag}}_J(q) \| J_i \rangle|^2 \right) \Bigg\}, \end{aligned} \tag{1.22}$$

where the symbols $\|$ denote matrix elements that have been reduce in angular momentum, using the Wigner-Eckart theorem. v_L and v_T are the lepton kinematical factors, evaluated for $E >> m_e$:

$$v_L = \left| \frac{Q^2}{\mathbf{q}^2} \right|^2, \quad v_T = \frac{1}{2} \left| \frac{Q^2}{\mathbf{q}^2} \right| + \tan^2 \frac{\theta}{2} \tag{1.23}$$

If an initial state with good quantum numbers $J^{\pi_i}_i T_i, M_{J_i}, M_{T_i}$ and a final state with good quantum numbers $J^{\pi_f}_f T_f, M_{J_f}, M_{T_f}$ is assumed, the electromagnetic form

factors may then be defined in terms of reduced matrix elements in both angular momentum and isospin (using $\vdots\!\vdots$ symbols). E.g. for the charge form factor:

$$F_{CJ}(q) \equiv \frac{1}{\sqrt{2J_i+1}} \sum_{T=0,1} c_T(T_i, T_f, M_T) \langle J_f, T_f \vdots\!\vdots \hat{M}_{J;T}(q) \vdots\!\vdots J_i, T_i \rangle, \tag{1.24}$$

where the coefficients c_T arise from the matrix element reduction and $M_{T_i} = M_{T_f} \equiv M_T$ for neutral electroweak currents.

The differential cross section for scattering to discrete nuclear states now becomes

$$\frac{d\sigma}{d\Omega} = 4\pi\sigma_{\mathrm{M}} F^2(q,\theta), \tag{1.25}$$

where the total form factor F^2 is defined in the sum of the longitudinal and transverse contributions

$$F^2(q,\theta) = v_L \sum_{J\geq 0} F^2_{CJ}(q) + v_T \sum_{J\geq 1} \left[F^2_{EJ}(q) + F^2_{MJ}(q) \right]. \tag{1.26}$$

1.2.3 Parity-Violating Asymmetry

The parity violating asymmetry is defined by

$$A_{\mathrm{PV}} = \left\{ \frac{d\sigma^{\uparrow}}{d\Omega} - \frac{d\sigma^{\downarrow}}{d\Omega} \right\} \Bigg/ \left\{ \frac{d\sigma^{\uparrow}}{d\Omega} + \frac{d\sigma^{\downarrow}}{d\Omega} \right\}, \tag{1.27}$$

where the $\uparrow$ ($\downarrow$) indicate the incident electron spin-dependent differential cross sections. The leptonic tensor from Equation 1.11a is easily modified by noting the projections for right- and left-handed Dirac electrons:

$$P^{\uparrow} = \frac{1}{2}(1-\gamma_5) \qquad P^{\downarrow} = \frac{1}{2}(1+\gamma_5) \tag{1.28}$$

resulting in

$$\begin{aligned}
\text{for } d\sigma^{\uparrow}: \quad \eta^{\uparrow}_{\mu\nu} &= -2EE' \sum_s \sum_{s'} \bar{u}(k)\gamma_\nu u(k')\bar{u}(k')\gamma_\mu P^{\uparrow} u(k) \\
\text{for } d\sigma^{\downarrow}: \quad \eta^{\downarrow}_{\mu\nu} &= -2EE' \sum_s \sum_{s'} \bar{u}(k)\gamma_\nu u(k')\bar{u}(k')\gamma_\mu P^{\downarrow} u(k) \\
\text{for } d\sigma^{\uparrow} - d\sigma^{\downarrow}: \quad \eta^{(-)}_{\mu\nu} &= -2EE' \sum_s \sum_{s'} \bar{u}(k)\gamma_\nu u(k')\bar{u}(k')\gamma_\mu(-\gamma_5) u(k) \\
\text{for } d\sigma^{\uparrow} + d\sigma^{\downarrow}: \quad \eta^{(+)}_{\mu\nu} &= -2EE' \sum_s \sum_{s'} \bar{u}(k)\gamma_\nu u(k')\bar{u}(k')\gamma_\mu(1) u(k).
\end{aligned} \tag{1.29}$$

Many factors cancel in the ratio, making the asymmetry

$$A = \frac{G_F Q^2}{4\pi\alpha\sqrt{2}} \frac{\eta^{(1)}_{\mu\nu} W^{(1)}_{\mu\nu} + \eta^{(2)}_{\mu\nu} W^{(2)}_{\mu\nu}}{2\eta_{\mu\nu} W_{\mu\nu}}, \tag{1.30}$$

where the numerator terms are

$$\begin{aligned}
\eta^{(1)}_{\mu\nu} &= -2EE' \sum_s \sum_{s'} \bar{u}(k)\gamma_\nu u(k')\bar{u}(k')\gamma_\mu(a + b\gamma_5)(-\gamma_5) u(k) \\
W^{(1)}_{\mu\nu} &= (2\pi)^3 \overline{\sum_i} \sum_f E_p \delta^{(4)}(q + p' - p) \langle p | J^{\gamma}_{\nu}(0) | p' \rangle \langle p' | \mathcal{J}^{Z}_{\mu}(0) | p \rangle \\
\eta^{(2)}_{\mu\nu} &= -2EE' \sum_s \sum_{s'} \bar{u}(k)\gamma_\nu(a + b\gamma_5) u(k')\bar{u}(k')\gamma_\mu(-\gamma_5) u(k) \\
W^{(2)}_{\mu\nu} &= (2\pi)^3 \overline{\sum_i} \sum_f E_p \delta^{(4)}(q + p' - p) \langle p | \mathcal{J}^{Z}_{\nu}(0) | p' \rangle \langle p' | J^{\gamma}_{\mu}(0) | p \rangle,
\end{aligned} \tag{1.31}$$

and the denominator term evaluated in the previous section.

To proceed further, the neutral weak current is separated into its vector and axial-vector terms (i.e. $\mathcal{J}^{Z}_{\mu} = J^{Z}_{\mu} + J^{Z}_{\mu 5}$). Then, as was done with the electromagnetic case, the neutral weak current matrix elements are expressed in the general form for a $J^{\pi} = \frac{1}{2}^{+}$ nucleon

$$\langle p' | J^{Z}_{\mu}(0) | p \rangle = \bar{u}(p') \left[\widetilde{F}_1(Q^2)\gamma_\mu + i \frac{\widetilde{F}_2(Q^2)}{2M_T} \sigma_{\mu\nu} q^\nu \right] u(p) \tag{1.32a}$$

$$\langle p' | J^{Z}_{\mu 5}(0) | p \rangle = \bar{u}(p') \left[\widetilde{G}_A(Q^2)\gamma_\mu + i \frac{\widetilde{G}_P(Q^2)}{M_T} q^\mu \right] \gamma_5 u(p), \tag{1.32b}$$

where $\widetilde{G}_A$ and $\widetilde{G}_P$ are the axial-vector and pseudo-scalar form factors of the nucleon.

Contraction of the leptonic and hadronic tensors leads to the parity violating asymmetry

$$\boxed{A_{\rm PV} = -\frac{A^0}{2}\left(\frac{\epsilon G_E \widetilde{G}_E + \tau G_M \widetilde{G}_M - (1-4\sin^2\theta_W)\epsilon' G_M \widetilde{G}_A}{\epsilon (G_E)^2 + \tau (G_M)^2}\right)} \tag{1.33}$$

where $\epsilon' = \sqrt{1-\epsilon^2}\sqrt{\tau(1+\tau)}$ and

$$A_0 = \frac{G_F Q^2}{2\pi\alpha\sqrt{2}}. \tag{1.34}$$

Generalizing the parity violating asymmetry to include scattering from nuclear targets involves a multipole expansion of the weak neutral vector currents (as was prescribed for the electromagnetic case in Section 1.2.2). Here, the asymmetry is written in terms of the leptonic and hadronic longitudinal (L) and transverse (T, T') projections

$$A_{\rm PV} = A^0\left(\frac{v_L W^L_{AV}(q) + v_T W^T_{AV}(q) + v_{T'} W^{T'}_{VA}(q)}{F^2(q,\theta)}\right), \tag{1.35}$$

where v_L and v_T are defined in 1.23 and

$$v_{T'} = \tan^2\frac{\theta}{2}\sqrt{\left|\frac{Q^2}{\mathbf{q}^2}\right| + \tan^2\frac{\theta}{2}}. \tag{1.36}$$

The subscripts help to identify which vector currents are involved: AV for leptonic axial-vector and hadronic vector, VA for leptonic vector and hadronic axial-vector. The hadronic responses are found to be [18]

$$\begin{aligned} W^L_{AV}(q) &= \sum_{J\geq 0} F_{CJ}(q)\widetilde{F}_{CJ}(q) \\ W^T_{AV}(q) &= \sum_{J\geq 1}\Big[F_{EJ}(q)\widetilde{F}_{EJ}(q) + F_{MJ}(q)\widetilde{F}_{MJ}(q)\Big] \\ W^{T'}_{VA}(q) &= -(1-4\sin^2\theta_W)\sum_{J\geq 1}\Big[F_{EJ}(q)\widetilde{F}_{MJ_5}(q) + F_{MJ}(q)\widetilde{F}_{EJ_5}(q)\Big]. \end{aligned} \tag{1.37}$$

One example is to consider elastic scattering from $J^\pi = 0^+$ target. Such is the

case for a ^{4}He or a ^{12}C target. From Equations 1.26 and 1.37 we have

$$\begin{aligned} F^2(q,\theta) &= v_L F_{C0}^2(q) \\ v_L W_{AV}^L(q) &= v_L F_{C0} \widetilde{F}_{C0} \\ W_{AV}^T(q) &= W_{VA}^{T'}(q) = 0. \end{aligned} \tag{1.38}$$

The resulting asymmetry provides a measurement of the ratio of the weak neutral current and electromagnetic form factors

$$A_{\mathrm{PV}}(0^+ \to 0^+) = -A^0 \frac{\widetilde{F}_{C0}(q)}{F_{C0}(q)}. \tag{1.39}$$

1.2.4 Strange Quark Contributions

Since the nucleon is made of up quarks, the hadronic current is expressed in the form of its associated operator and the hadronic state:

$$J_\mu^\gamma \equiv \langle H|\hat{J}_\mu^\gamma|H\rangle \tag{1.40a}$$

$$J_\mu^Z \equiv \langle H|\hat{J}_\mu^Z|H\rangle \tag{1.40b}$$

$$J_{\mu 5}^\gamma \equiv \langle H|\hat{J}_{\mu 5}^Z|H\rangle \tag{1.40c}$$

where each operator is a sum of the contribution from each quark (q) in the nucleon:

$$\hat{J}_\mu^\gamma \equiv \sum_q Q_q \bar{u}_q \gamma_\mu u_q \tag{1.41a}$$

$$\hat{J}_\mu^Z \equiv \sum_q g_V^q \bar{u}_q \gamma_\mu u_q \tag{1.41b}$$

$$\hat{J}_{\mu 5}^Z \equiv \sum_q g_A^q \bar{u}_q \gamma_\mu \gamma_5 u_q, \tag{1.41c}$$

where the electromagnetic Q_q and neutral weak $g_{V,A}^q$ "charges" are shown in Table 1.2.4. In principle the sum in equation 1.41 is over all quark flavors (u, d, s, c, b, and t), but for the remainder of this text, it will be assumed that the structure of the nucleon is dominated by the lighter quarks (u, d, and s). It is useful to re-express

Quark	Q	g_V	g_A
u,c,t	$+2/3$	$+1-8/3\sin^2\theta_W$	-1
d,s,b	$-1/3$	$-1+4/3\sin^2\theta_W$	$+1$

TABLE 1.2: Electromagnetic and Weak charges for the quarks.

equation 1.41 in terms of SU(3) octet and singlet currents. To begin, one defines a set of vector and axial vector operators:

$$\hat{V}^a_\mu \equiv \bar{q}\frac{\lambda^a}{2}\gamma_\mu q \tag{1.42}$$

$$\hat{A}^a_\mu \equiv \bar{q}\frac{\lambda^a}{2}\gamma_\mu\gamma_5 q \tag{1.43}$$

where q represents the triplet $\begin{pmatrix} u \\ d \\ s \end{pmatrix}$, $\lambda^0 = \frac{2}{3}\mathbf{1}$, and $\lambda^{1\cdots 8}$ are the Gell-Mann SU(3) matrices normalized to $\mathrm{Tr}(\lambda^a\lambda^b) = 2\delta^{ab}$. Since equation 1.41 contains no flavor changing elements, only the diagonal terms are required (i.e. a=0,3,8):

$$\hat{V}^0_\mu = \frac{1}{3}(\bar{u}\gamma_\mu u + \bar{d}\gamma_\mu d + \bar{s}\gamma_\mu s) \tag{1.44a}$$

$$\hat{V}^3_\mu = \frac{1}{2}(\bar{u}\gamma_\mu u - \bar{d}\gamma_\mu d) \tag{1.44b}$$

$$\hat{V}^8_\mu = \frac{1}{2\sqrt{3}}(\bar{u}\gamma_\mu u + \bar{d}\gamma_\mu d - 2\bar{s}\gamma_\mu s) \tag{1.44c}$$

$$\hat{A}^0_\mu = \frac{1}{3}(\bar{u}\gamma_\mu\gamma_5 u + \bar{d}\gamma_\mu\gamma_5 d + \bar{s}\gamma_\mu\gamma_5 s) \tag{1.45a}$$

$$\hat{A}^3_\mu = \frac{1}{2}(\bar{u}\gamma_\mu\gamma_5 u - \bar{d}\gamma_\mu\gamma_5 d) \tag{1.45b}$$

$$\hat{A}^8_\mu = \frac{1}{2\sqrt{3}}(\bar{u}\gamma_\mu\gamma_5 u + \bar{d}\gamma_\mu\gamma_5 d - 2\bar{s}\gamma_\mu\gamma_5 s) \tag{1.45c}$$

At the level of strong isospin, the 0^{th} and 8^{th} components are identified as isoscalar operators and the 3^{rd} components as isovector operators. The isoscalar and isovector components of the electromagnetic hadronic current is now identified:

$$\hat{J}^\gamma_\mu(T=0) = \frac{1}{\sqrt{3}}\hat{V}^8_\mu \tag{1.46a}$$

$$\hat{J}^\gamma_\mu(T=1) = \hat{V}^3_\mu \tag{1.46b}$$

The neutral current hadronic currents is now re-written in terms of the electromagnetic hadronic current by observing the similarity between the electromagnetic and neutral expressions in equation 1.41:

$$\hat{J}^Z_\mu = \xi_V^{T=1}\hat{J}^\gamma_\mu(T=1) + \sqrt{3}\xi_V^{T=0}\hat{J}^\gamma_\mu(T=0) + \xi_V^0\hat{V}^s_\mu \quad (1.47a)$$

$$\hat{J}^Z_{\mu 5} = \xi_A^{T=1}\hat{A}^3_\mu + \xi_A^{T=0}\hat{A}^8_\mu + \xi_A^0\hat{A}^s_\mu \quad (1.47b)$$

where the strange matrix elements ($\hat{V}^s_\mu \equiv \bar{s}\gamma_\mu s$, $\hat{A}^s_\mu \equiv \bar{s}\gamma_\mu\gamma_5 s$) have been extracted for emphasis, and the coefficients defined as:

$$\xi_{V,A}^{T=1} \equiv g^u_{V,A} - g^d_{V,A} \quad (1.48a)$$

$$\xi_{V,A}^{T=0} \equiv \sqrt{3}(g^u_{V,A} + g^d_{V,A}) \quad (1.48b)$$

$$\xi^0_{V,A} \equiv g^u_{V,A} + g^d_{V,A} + g^s_{V,A} \quad (1.48c)$$

Contributions to Single Nucleon Form Factors

Assuming the nucleon to be an eigenstate of isospin, one may construct the isoscalar ($T=0$) and isovector ($T=1$) form factors

$$G_{E,M}^{T=0} = \frac{1}{2}(G^p_{E,M} + G^n_{E,M}) \quad (1.49a)$$

$$G_{E,M}^{T=1} = \frac{1}{2}(G^p_{E,M} - G^n_{E,M}), \quad (1.49b)$$

where the p and n subscripts indicate the electromagnetic Sachs form factors for the proton and neutron. From these, the single neutral weak form factors are evaluated from the matrix elements of Equation 1.47

$$\widetilde{G}_{E,M} = \tau_3\xi_V^{T=1}G_{E,M}^{T=1} + \sqrt{3}\xi_V^{T=0}G_{E,M}^{T=0} + \xi_V^0 G^s_{E,M}, \quad (1.50)$$

where τ_3 is $+1(-1)$ for a proton(neutron), and $G^s_{E,M}$ are the vector strange form factors of the nucleon. For a proton target, the neutral weak form factors from Equation 1.33 become

$$\widetilde{G}^p_{E,M} = (1 - 4\sin^2\theta_W)G^p_{E,M} - G^n_{E,M} - G^s_{E,M}. \quad (1.51)$$

Thus, the parity violating asymmetry from a proton, and using existing data for the determination of the electromagnetic form factors for the proton and neutron, provides a measure of the electric and magnetic strange form factors as well as the axial form factor.

As was done in Equation 1.17, the vector strange form factors are expressed using the Galster parameterization

$$G_E^s = \rho_s \tau G_D^v \xi_E^s \tag{1.52a}$$

$$G_M^s = \mu_s G_D^v \xi_M^s, \tag{1.52b}$$

where

$$\xi_{E,M}^s = (1 + \lambda_{E,M}^s)^{-1}. \tag{1.53}$$

ρ_s is referred to as the "strange charge density", and μ_s is the "strange magnetic moment" of the nucleon. A commonly used definition, is that of the "strange radius" which is related to ρ_s and μ_s through

$$\langle r^2 \rangle_s \equiv 6 \left. \frac{dF_1^s}{dQ^2} \right|_{Q^2=0} \tag{1.54a}$$

$$\rho_s = \left. \frac{dG_E^s}{d\tau} \right|_{\tau=0} = -\frac{2}{3} m_N^2 \langle r^2 \rangle_s - \mu_s. \tag{1.54b}$$

Contributions to Nuclear Form Factors

Evaluation of the neutral weak form factors for a nuclear target is also aided by the result of Equation 1.47. E.g. for the neutral weak charge form factor

$$\widetilde{F}_{CJ} \equiv \frac{1}{2} \left[\xi_V^{T=1} F_{CJ}^{T=1} + \sqrt{3} \xi_V^{T=0} F_{CJ}^{T=0} + \xi_V^0 F_{CJ}^s \right], \tag{1.55}$$

where the factor of $\frac{1}{2}$ is introduced to be consistent with the same factor in Equation 1.49. For a elastic scattering from a ^{4}He target, a $(J^\pi T) = (0^+0) \rightarrow (0^+0)$ transition, this form factor becomes

$$\widetilde{F}_{C0}^{T=0} = \frac{1}{2} \left[\sqrt{3} \xi_V^{T=0} F_{C0}^{T=0} + \xi_V^0 F_{C0}^s \right]. \tag{1.56}$$

The associated parity violating asymmetry from this process, is then calculated (from Equation 1.39) to be

$$A_{\rm PV}(0^+0 \to 0^+0) = -\frac{A^0}{2}\left[\sqrt{3}\xi_V^{T=0} + \xi_V^0 \frac{F_{C0}^s}{F_{C0}^{T=0}}\right]. \tag{1.57}$$

The absence of strange quark contributions to this asymmetry is in agreement with the work developed by Feinberg [19].

1.2.5 Isospin Mixing of Nuclear States

The assumption of an exact isospin symmetry at the nuclear level for elastic scattering from ^{4}He allowed for truncation of the matrix element sums in the nuclear form factor expressions to one term. This assumption is reduced to an approximate symmetry if there is the presence of charge symmetry breaking caused by Coulomb interactions between the nucleons.

A reasonable approach to calculating the correction due to isospin-mixing is outlined in detail in Ref. [18]. The main feature is to consider that the observed states $|"T_0"\rangle$ and $|"T_1"\rangle$ are mixtures are exact isospin states $|T_0\rangle$ and $|T_1\rangle$:

$$\begin{aligned} |"T_0"\rangle &\simeq |T_0\rangle + \chi|T_1\rangle \\ |"T_1"\rangle &\simeq -\chi|T_0\rangle + |T_1\rangle, \end{aligned} \tag{1.58}$$

where χ is a small mixing parameter. The dominating mixing state is expected to be $T_1 = T_0{+}1$. The nuclear form factors then become (neglecting strange contributions)

$$\begin{aligned} F_{CJ} &= \langle 0^+"0"\|\hat{M}_0(T=0) + \hat{M}_0(T=1)\|0^+"0"\rangle \\ &\approx \langle 0^+0\|\hat{M}_0(T=0)\|0^+0\rangle + 2\chi\langle 0^+0\|\hat{M}_0(T=1)\|0^+1\rangle \end{aligned} \tag{1.59}$$

$$\begin{aligned} \widetilde{F}_{CJ} &= \tfrac{1}{2}\langle 0^+"0"\|\sqrt{3}\xi_V^{T=0}\hat{M}_0(T=0) + \xi_V^{T=1}\hat{M}_0(T=1)\|0^+"0"\rangle \\ &\approx \tfrac{1}{2}\sqrt{3}\xi_V^{T=0}\langle 0^+0\|\hat{M}_0(T=0)\|0^+0\rangle + \chi\xi_V^{T=1}\langle 0^+0\|\hat{M}_0(T=1)\|0^+1\rangle. \end{aligned}$$

Keeping only terms up to order χ introduces a isospin-mixing correction term to the asymmetry

$$A_{\rm PV} = -\frac{A^0}{2}\left[\sqrt{3}\xi_V^{T=0}(1+\Gamma(q))\right], \tag{1.60}$$

where

$$\Gamma(q) = \chi(\xi_V^{T=1} - \sqrt{3}\xi_V^{T=0})\frac{\langle 0^+0\|\hat{M}_0(T=1)\|0^+1\rangle}{\langle 0^+0\|\hat{M}_0(T=0)\|0^+0\rangle}. \tag{1.61}$$

$\Gamma(q)$ has been evaluated in Ref. [20] over a wide range of q, as shown in Figure 1.5. At the kinematics for this experiment, $\Gamma(q = 0.54\ \mathrm{fm}^{-1})$ is negligible.

1.2.6 Impulse Approximation of Nuclear Currents

A connection between the single nucleon form factors and the nuclear form factors is obtained by using one-body operators in the expressions for the electromagnetic and neutral weak current matrix elements. This so-called "Impulse Approximation" is then usually corrected for using two-body operators from meson-exchange currents. In general, the matrix elements from Equation 1.24 can be expressed in the form

$$\langle J_f; T_f \vdots\!\vdots \hat{O}^{[1]}_{JT}(q) \vdots\!\vdots J_i; T_i\rangle = \sum_{a,a'} \psi^{(fi)}_{JT}(a',a)\langle a' \vdots\!\vdots \hat{O}^{[1]}_{JT}(q) \vdots\!\vdots a\rangle, \tag{1.62}$$

where the nuclear many-body dynamics are contained within the $\psi^{(fi)}_{JT}(a',a)$ coefficients. In this section, we apply this approximation for the particular case at hand: elastic scattering from ^{4}He. Since the ^{4}He nucleus can only support matrix elements of the isoscalar Coulomb operator, the multipole expansion from Equation 1.24 becomes

$$\begin{aligned} F^{(a)}_{C0}(q) &= \langle 0^+0|\hat{M}^{(a)}_{00}(q)|0^+0\rangle & \text{(1.63a)}\\ \hat{M}^{(a)}_{00}(q) &= \int d^3x j_0(qx) Y_{00}(\Omega_x)\hat{\rho}^{(a)}(\mathbf{x}) & \text{(1.63b)}\\ &= \frac{1}{4\pi}\int d\Omega_q Y_{00}(\Omega_q)\hat{\rho}^{(a)}(\mathbf{q}) & \text{(1.63c)} \end{aligned}$$

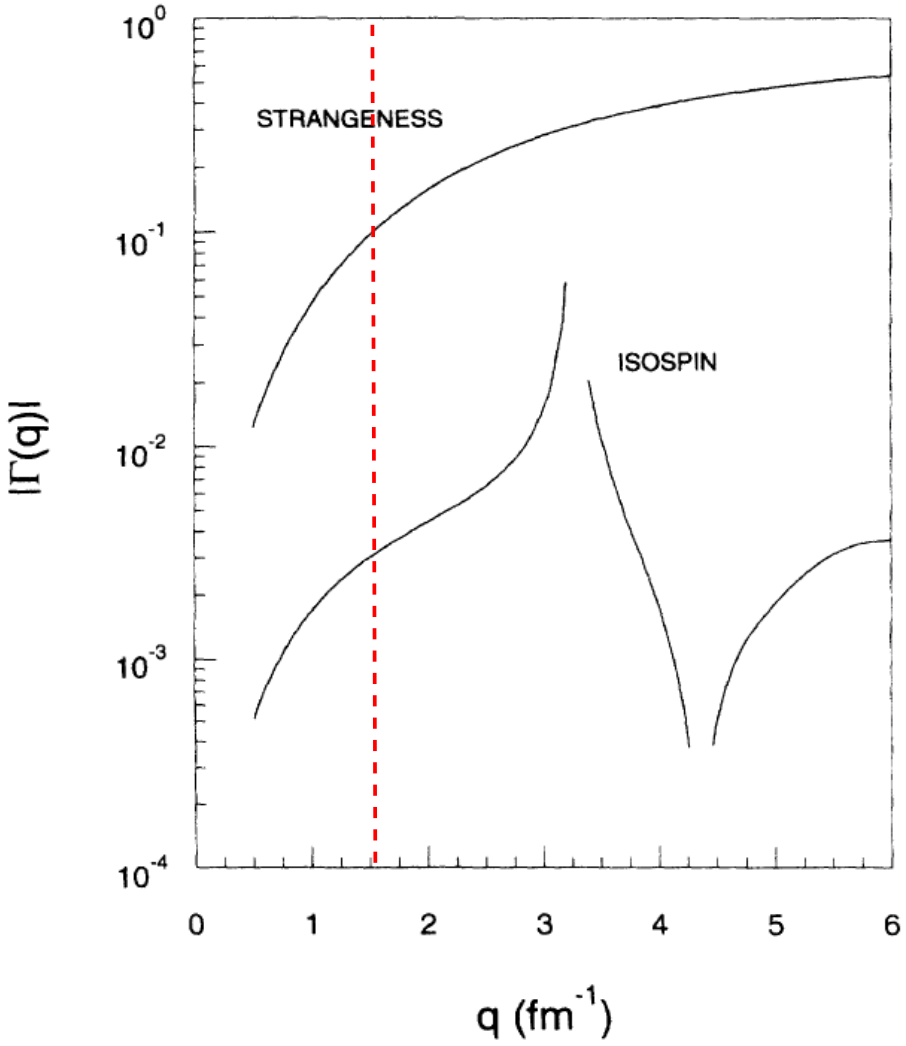

FIG. 1.5: Nuclear isospin mixing correction $\Gamma(q)$ as a function of the magnitude of the four-momentum transfer q as calculated in Ref. [20]. Strangeness solid line is computed using $\rho_s = -2, \lambda_E^s = 5.6$. Dashed line indicates the four-momentum transfer for this experiment ($q_{\rm exp} = 1.53$ fm^{-1}).

where $\hat{\rho}^{(a)}$ is the charge component of the hadronic current, and the superscript (a) refers to either the isoscalar electromagnetic current ($(a) \rightarrow T{=}0$) or the strange quark current ($(a) \rightarrow s$). Construction of $\hat{\rho}^{(a)}$ is accomplished in the Impulse Approximation (IA) by expanding the general form of the hadronic current

$$\langle p'|J_{\mu}^{(a)}(0)|p\rangle = \bar{u}(p')\left[F_1^{(a)}(Q^2)\gamma_\mu + i\frac{F_2^{(a)}(Q^2)}{2m_N}\sigma_{\mu\nu}q^\nu\right]u(p) \tag{1.64}$$

to order $1/m^2$, transforming into coordinate space, and summing over all nucleons A. The result for $\mu = 0$ is the one-body charge density operator:

$$\langle p'|\hat{\rho}^{(a)}(\mathbf{q})^{[1]}p\rangle = \sum_{k=1}^{A} e^{i\mathbf{q}\cdot\mathbf{x}_k}\left[\frac{G_E^{(a)}(\tau)}{\sqrt{1+\tau}} - \frac{i}{8m_N^2}\{G_E^{(a)}(\tau) - 2G_M^{(a)}(\tau)\}\boldsymbol{\sigma}_k\cdot\mathbf{q}\times\mathbf{P}_k\right] \tag{1.65}$$

where $\boldsymbol{\sigma}_k$ and $\mathbf{P}_k$ is the spin and momentum of the k^{th} nucleon. The Coulomb multipole operator is then obtained by substituting this expression into Equation 1.63b:

$$\langle p'|\hat{M}_{00}^{(a)}(q)^{[1]}|p\rangle = \frac{1}{2\sqrt{\pi}}\sum_{k=1}^{A}\left\{\frac{G_E^{(a)}(\tau)}{\sqrt{1+\tau}}j_0(qx_k) + [G_E^{(a)}(\tau) - 2G_M^{(a)}(\tau)]\frac{q}{2m_N}\frac{j_1(qx_k)}{m_N x_k}\boldsymbol{\sigma}_k\cdot\mathbf{L}_k\right\} \tag{1.66}$$

where $\mathbf{L}_k$ is the orbital angular momentum of the k^{th} nucleon. In the limit that the nuclear ground state of ^{4}He contains nucleons in an S state, the spin-orbit term disappears leaving the form factor ratio independent of nuclear structure:

$$\left.\frac{F_{C0}^s}{F_{C0}^{T=0}}\right|_{[1],S-waves} \longrightarrow \frac{G_E^s}{G_E^{T=0}}. \tag{1.67}$$

Two-body meson exchange currents

The leading two-body meson exchange current (MEC) corrections that arise from the impulse approximation are constructed from the diagrams in Figure 1.6.

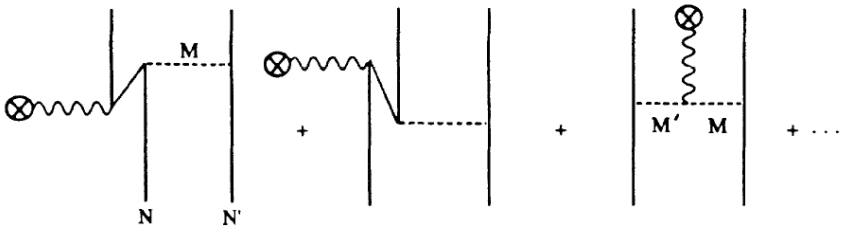

FIG. 1.6: Contributing diagrams to two-body meson exchange currents. Circles indicate experimental values.

The first two diagrams show a π- and vector meson-exchange creating an intermediate nucleonic state before or after the boson interaction. The third diagram showing the interaction of the boson with the mediating meson exchange.

The two-body current operators, from these processes, are computed by first calculating of the Feynman amplitudes from their associated diagrams. This is followed by an expansion in powers of $1/m^2$ and transformation into coordinate space, as was done in the one-body case. This calculation is described in detail in Ref. [21].

The resulting ^{4}He charge form factor, as calculated by Ref. [21], with and without the two-body correction is shown in Figure 1.7. It is evident, from this plot, that the inclusion of the two-body currents is required for better comparison with the data near the diffraction minimum. However, the correction is of negligible size at the experimental kinematics. Figure 1.8 shows the individual MEC and spin-orbit contributions, from this calculation.

Most importantly is the calculation of the form factor ratio (Equation 1.67) that is shown in Figure 1.9. A large discrepancy between the IA and IA+MEC calculation, here, would indicate a proportional correction to the theoretical parity violating asymmetry. At the kinematics of this experiment, this discrepancy is negligible.

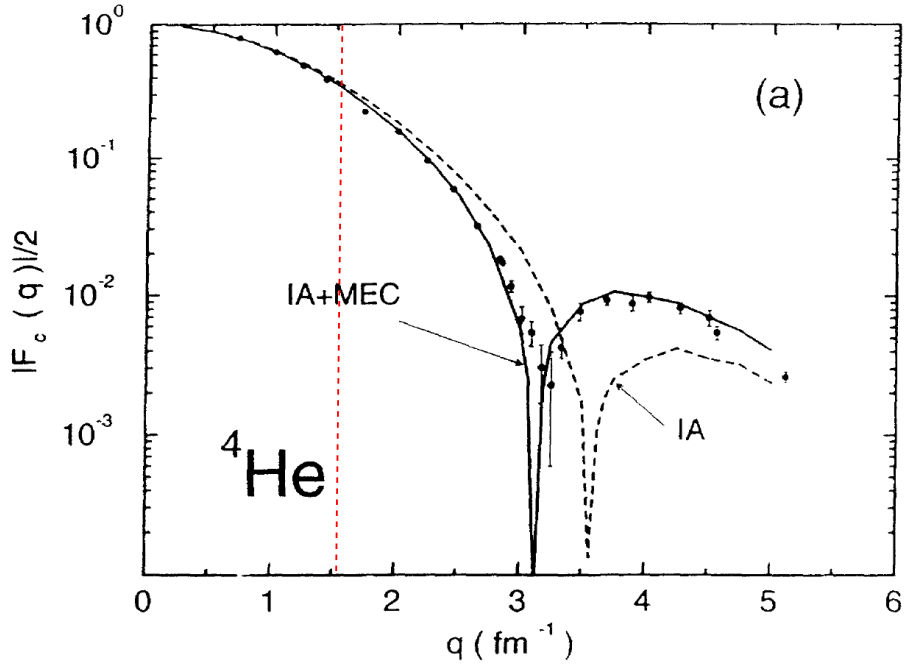

FIG. 1.7: ^{4}He form factor versus the magnitude of the four-momentum transfer . Dashed line indicates the calculation using the impulse approximation (IA), where the solid line includes the correction from meson exchange currents (MEC). Vertical dashed line indicates the value of q for this experiment.

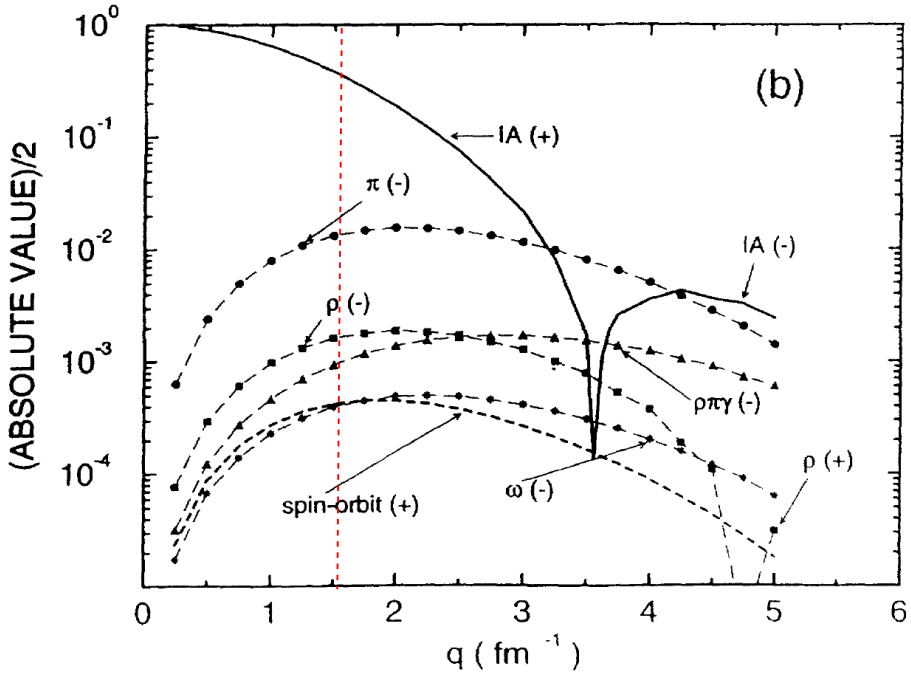

FIG. 1.8: Contributions to ^{4}He form factor from meson exchange currents and spin-orbit versus the magnitude of the four-momentum transfer. Vertical dashed line indicates the value of q for this experiment.

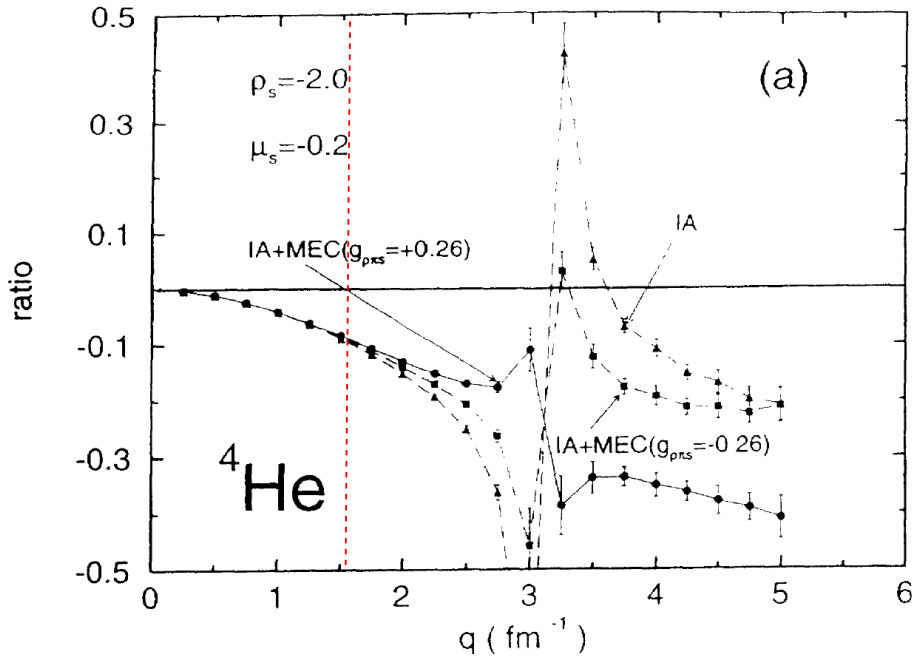

FIG. 1.9: Ratio of strange form factor to isoscalar electromagnetic form factor versus the magnitude of the four-momentum transfer. Vertical dashed line indicates the value of q for this experiment.

1.2.7 Final Theoretical Asymmetry

The summarize, the parity violation asymmetry from elastic scattering of longitudinally polarized electrons from ^{4}He is

$$\boxed{A_{\rm PV} = -\frac{A^0}{2}\left\{\sqrt{3}\xi_V^{T=0}\left[1+\Gamma(q)\right] + \xi_V^0 \frac{2G_E^s}{G_E^p+G_E^n}\right\}}. \tag{1.68}$$

Including the electroweak radiative corrections, we express the ξ coefficients as

$$\sqrt{3}\xi^{T=0} = -4\rho'\kappa'\sin^2\theta_W - 6\lambda_{1u} - 6\lambda_{1d} \tag{1.69a}$$

$$\xi_V^0 = -\left[\rho' + 2(\lambda_{1u}+\lambda_{1d}+\lambda_{1s})\right], \tag{1.69b}$$

where the ρ', κ', λ coefficients are obtained from Ref. [22]. Interestingly, the overall sign of this asymmetry is opposite of that from the proton (Equation 1.33). We have shown that the nuclear corrections to this result is either small or negligible, indicating that an experimental measurement of this asymmetry provides a clean measure of G_E^s.

CHAPTER 2

Experimental Apparatus

Experiments that measure parity-violating asymmetries on the order of a few parts-per-million (ppm) must overcome various critical challenges if the systematic errors are to be kept below the level of the statistical uncertainty. A result of this type provides high nfidence in the experimental method and the techniques used to achieve this goal are useful in designing future experiments endeavoring to measure even smaller asymmetries. The Jefferson Lab experiment E00114, referred to in this paper using it's nickname "HAPPEx-^{4}He", employs three basic philosophies in order to obtain a small absolute and relative measure of the parity-violating asymmetry and at the same time being statistics limited. The first is to keep all corrections to the detected asymmetry as small as physically possible. The second is to accurately measure these corrections. Finally, to obtain a result in a reasonable amount of time the rate of the detected particles must be maintained as high as possible, while at the same time keeping small the factors that may dilute the asymmetry.

We begin this chapter by providing an overview of the experimental technique that utilizes the above mentioned philosophies. This is followed by a more detailed view of the experimental apparatus, starting with a description of the Jefferson

Lab accelerator and its polarized electron source. We then briefly describe electron beam diagnostic equipment that measure its polarization, intensity, and position. Finally, we summarize the use of the Hall A cryogenic target and High Resolution Spectrometers, and conclude with an explanation of the focal plane detectors and data acquisition system used during HAPPEX-^{4}He.

2.1 Experimental Technique

In this experiment, the parity-violating asymmetry is measured by detecting scattered longitudinally polarized electrons from the unpolarized ^{4}He target. Experimentally, this asymmetry is defined as

$$A_{\text{det}} = \frac{S_R - S_L}{S_R + S_L}, \tag{2.1}$$

where the subscripts R and L, of the measured scattered flux S (normalized to the incident flux), indicate the right- and left-handedness of the incident electrons (referred to, in this paper, as right- and left-helicity electrons). At Jefferson Lab, the polarization (or helicity) of the electrons is changed every 33.3 ms providing the capability of measuring this asymmetry at 15 Hz. In this section, we summarize the technique in which HAPPEx-^{4}He measured this asymmetry in the context of issues and corrections that are typical for parity-violating asymmetry measurements.

Counting versus Integrating

Measurement of the scattered flux S is typically made by counting individual electrons with scintillator or Cherenkov detectors after they pass through a spectrometer. The signal created by a incident electron is then used to "trigger" the data acquisition system (DAQ) to digitize various characteristics of this detected signal. When used in parallel with drift chambers (or other position sensitive detec-

tors), this approach has the advantage of being able to reconstruct the kinematics of the interaction. The detected rates, in this method, are directly proportional to the incident flux until a rate threshold is reached.

One particular threshold arises from limitations in data transfer speeds within the DAQ. In this situation, a trigger may arrive while the DAQ is still processing a previous event. While this trigger may still be counted, the characteristics of the detected signal are not digitized. This effect, referred to as DAQ "dead-time", may be alleviated and corrected for by "prescaling": accepting and digitizing a predefined subset of the total amount triggers. This dead-time correction is a dilution to the detected scattering asymmetry and affects the fractional precision of its measurement.

A more serious threshold manifests itself with overlapping event triggers caused by two signals arriving at a detector very close in time and position. This not only presents a problem for counting individual electrons, but for obtaining their characteristics from position sensitive detectors. For very high rates many overlapping pulses cause a nearly constant detector signal, which is impossible to count.

HAPPEx-^{4}He uses a proven technology, utilized by the first HAPPEx [23], called the "Integrating Method". Calibration and measurement of the experimental kinematics and backgrounds is performed using the above mentioned counting method at an electron beam current that has a correctable amount of dead-time ($< 20\%$). However, when it comes to measuring the experimental asymmetry all tracking detectors are turned off and a special detector and integrating DAQ is used. The total (integrated) signal from all electrons is stored in a capacitor over each 33 ms beam helicity state. At the end of this state (or "helicity window") the capacitor is discharged and the charge digitized by an ADC. This provides a direct measure of the scattering flux intensity for the kinematic region of interest, weighted by the energy deposited into the detector. This method provides the means for mea-

suring the detected asymmetry at extremely high rates with zero rate thresholds. The expected scattered rate of about 10 MHz, at the experimental kinematics and beam current, provides a measurement of the asymmetry to the $\sim 0.15\%$ (1500 ppm) level at 15 Hz. For this experiment, this asymmetry was then measured 3 million times to gain a ~ 0.8 ppm absolute measure of its central value.

Details of the special detectors and DAQ are mentioned in Section 2.5.3 and 2.6.2, respectively.

False Asymmetries

In a perfect experiment, the asymmetry in Equation 2.1 would provide a direct measure of the parity-violating asymmetry as theorized from Equation 1.68. Unfortunately, even small variations in the setup lead to variations in the amount of flux incident on the target, and differences in the position of the beam, that are correlated with the difference of the helicity of the beam. These helicity-correlated differences create a scattered flux asymmetry that is not correlated with the parity-violating asymmetry (a so-called "false asymmetry"). Understanding how these helicity-correlated beam properties are created and how to minimize them, is a topic of great interest. Nearly all are traced back to the polarized beam source. Section 2.2.1 will describe this portion of the experimental apparatus in this context.

Despite all of the hard work and time that goes into minimizing helicity-correlated beam parameters, they cannot be eliminated completely. Correcting for false asymmetries, where

$$A_{\text{false}} = \sum_{i=x,y,\phi,\theta} \frac{dS}{dx_i} \Delta x_i, \tag{2.2}$$

involves precise measure of each helicity-correlated parameter ($\Delta x = x_R - x_L$) and accurate knowledge of the experimental sensitivity to those parameters (dS/dx). Measurement of the sensitivity is commonly made in two different methods. The

first method, called "Regression" (Appendix B), obtains the sensitivity by observing the correlation between the helicity-correlated detected rate and the natural helicity-correlated motion of the beam. The second method, called "Beam Modulation" (Section 3.1.3), involves deliberately perturbing the beam in a slow and non-helicity-correlated way and measuring the detector rate response. HAPPEx-^{4}He uses both methods as a systematic check on the correction for false asymmetries.

Backgrounds and Dilution Factors

The final issues concerning most parity-violation measurements are those of minimizing and measuring backgrounds and dilutions factors. The final experimental asymmetry in terms of these quantities is defined as

$$A_{\text{phys}} = \frac{KL}{P_b} \frac{A_{\text{corr}} - P_b \sum_i A_i f_i}{1 - \sum_i f_i}, \tag{2.3}$$

where K is an effective kinematics factor, L is a correction factor for nonlinearity, P_b is the beam polarization, and f_i and A_i are the background fraction and asymmetry, respectively. The effective kinematics factor K deals with the fact that the observed central scattering angle and Q^2 of the scattered electron may be altered significantly from those at the interaction vertex due to radiative losses and multiple scattering in the target. An accurate simulation of the experimental setup provides a means for obtaining K, with the details found in Section 3.6.

The factor L is a correction for nonlinearities in the measurement of the electron beam properties and the detection of scattered flux. As shown in Ref. [24], a measurement or detection non-linearity results in a modification of the measured asymmetry

$$A_{\text{meas}} = A_{\text{det}} + \epsilon F (A_{\text{det}} + A_I), \tag{2.4}$$

where ϵF is the first nonlinear term in the measured response, and A_I is the helicity-

correlated beam intensity asymmetry

$$A_I = \frac{A_R - A_L}{A_R + A_L}. \tag{2.5}$$

From Equation 2.4, it is apparent that this correction can be made small if A_I is kept much smaller than the detected asymmetry. Furthermore, the nonlinear term ϵF enters directly into the total systematic error as a fractional error, indicating that the uncertainty in the non-linearity must be small compared to the relative statistical uncertainty of the measurement.

Precise measurement of the beam polarization P_b is important because of it's weighting in the overall systematic error in the measurement. A higher beam polarization also serves to create a smaller dilution factor, leading to less beam time required to perform a relative asymmetry measurement. For this reason HAPPEx-^{4}He utilized the SuperLattice GaAs photo-cathode that produced an average beam polarization of 87%. This is to be compared to the strained GaAs cathode, used during the first HAPPEx during its 1999 run, that obtained an average beam polarization of 69% [23].

Any detector signal that results from physics other than that of which is being measured, is considered a background. For this experiment, in which the measurement is of elastically scattered electrons, this background may come from inelastic and quasielastic scattering. For this reason, backgrounds are treated as a dilution to the measured asymmetry, as seen in the denominator term $(1 - \sum_i f_i)$ of Equation 2.3. An added complication arises when any of these backgrounds is associated with a parity-violating asymmetry. This leads to the correction term $(-P_b \sum_i f_i A_i)$, where the background asymmetry A_i, in this experiment, is calculated from a simple theoretical model assuming a 100% polarized electron beam (thus requiring the measured polarization P_b scaling). Minimization of the background fractions f_i is aided through the use of the High Resolution Spectrometers (described in Section

2.5.2) that performs a kinematic separation of scattered particles at the target into a position separation due to its magnetic dispersion and focusing properties. For this reason, HAPPEx measurements provide results nearly free of backgrounds that may obscure the final results.

2.2 Accelerator

This experiment was performed at Jefferson Laboratory (JLab), utilizing the Continuous Electron Beam Accelerator Facility (CEBAF) shown in Figure 2.1. The recirculating linear electron accelerator is capable of providing up to 200 μA of continuous-wave electron beam which may be simultaneously shared between three experimental halls (Hall A, Hall B, and Hall C). Polarized electrons are produced by illuminating a photo-cathode with 1497 MHz laser light, and then accelerated up to 45 MeV. Each of the two superconducting linacs are capable of further acceleration up to 570 MeV and the beam can by recirculated up to four times. This provides an extraction beam energy of up to 5.7 GeV. Electrons to a specific experimental hall are peeled off using RF separators and a septum magnet.

Of particular interest to this experiment is the minimization of helicity-correlated beam systematics, which for the most part are tracked back to how the beam is created at the polarized source.

2.2.1 Polarized Source

The polarized source at Jefferson Lab begins with the source laser table. Figure 2.2 shows an illustration of the various optical elements found on this table. An understanding and careful setup of the laser light transport through this system is important for minimizing helicity-correlated beam systematics.

If one considers the beam intensity asymmetry (defined in Equation 2.5) to be a

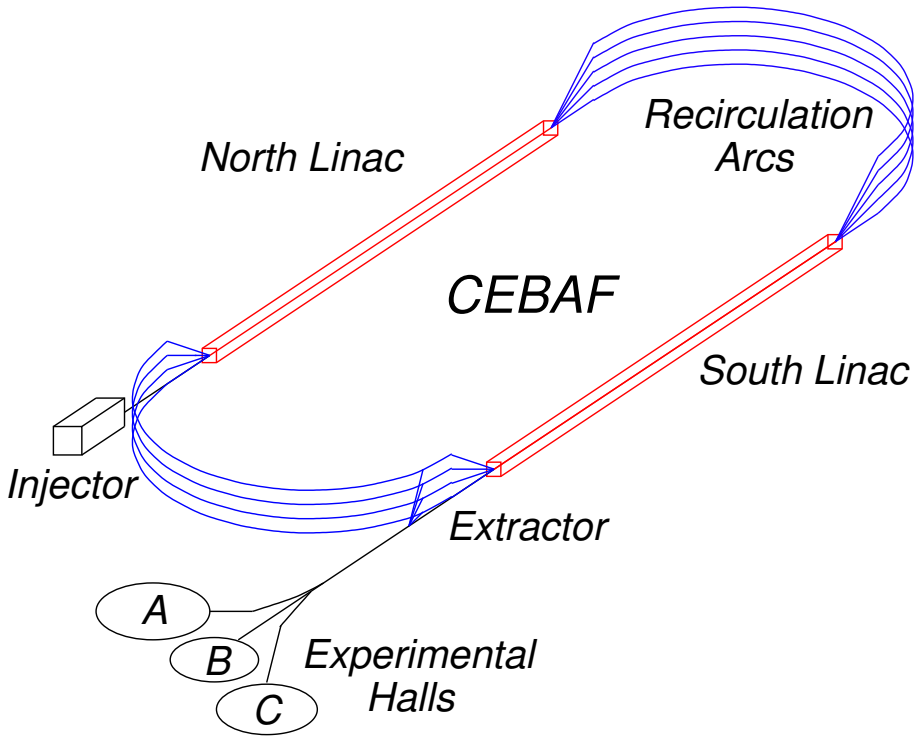

FIG. 2.1: Schematic overview of the CEBAF accelerator.

"zeroth-order" effect on helicity-correlated beam systematics, the first-order effects are the beam position differences. Much research and work has been done to study and minimize these effects [25, 26, 27]. Careful alignment of the laser transport through the laser table optical devices was performed [28] to minimize the effects of beam steering, birefringence gradients of the Pockels Cell, and gradients in the photo-cathode, all of which can contribute to helicity-correlated effects.

Ti:Sapphire Laser

The Hall A laser, used during this experiment, was a high powered Ti:Sapphire laser tuned to deliver a wavelength of 851 nm required to exploit the band-gap splitting of specific electron energy states in the photo-cathode. This laser was designed and built specifically for Jefferson Lab by Time-Bandwidth Products.

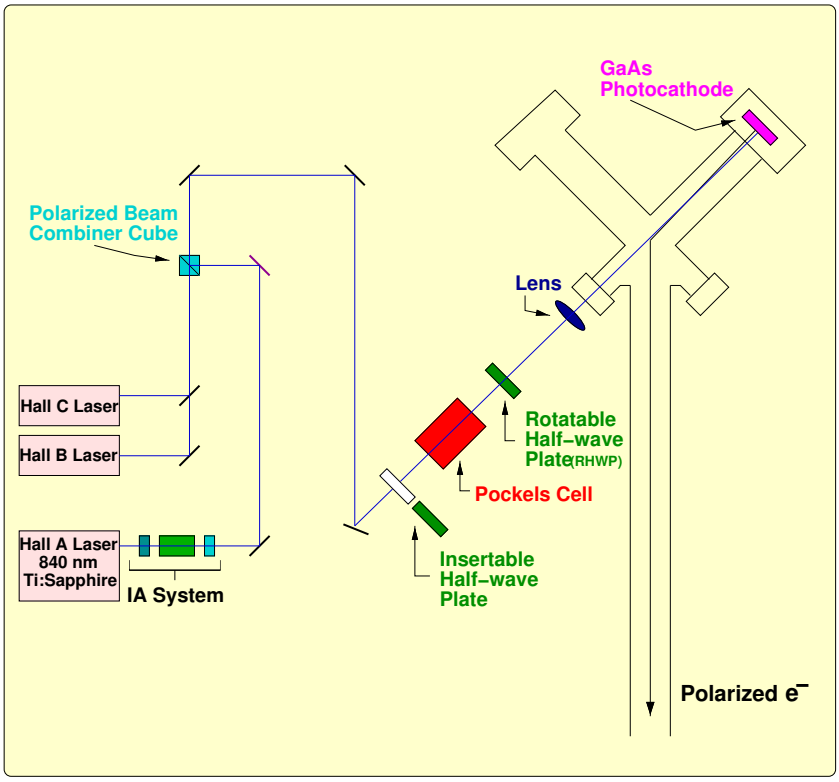

FIG. 2.2: Schematic of the optical elements on the source laser table.

Pockels Cell

The Pockels Cell is used as a voltage-controlled, rapidly switching $\lambda/4$-plate to convert linearly polarized light into circularly polarized light. The degree to which the beam wavelength is retarded can be adjusted through application of an appropriate high voltage to provide control over the phase difference between the outgoing polarization states.

SuperLattice GaAs Cathode

Circularly polarized light produces polarized electrons from a strained super-lattice Gallium-Arsenide (GaAs) cathode through photo-emission. This cathode is made up of several layers of material containing GaAs with varying amounts of phosphorus doping, grown on a substrate [29]. Photons of a specific helicity excite

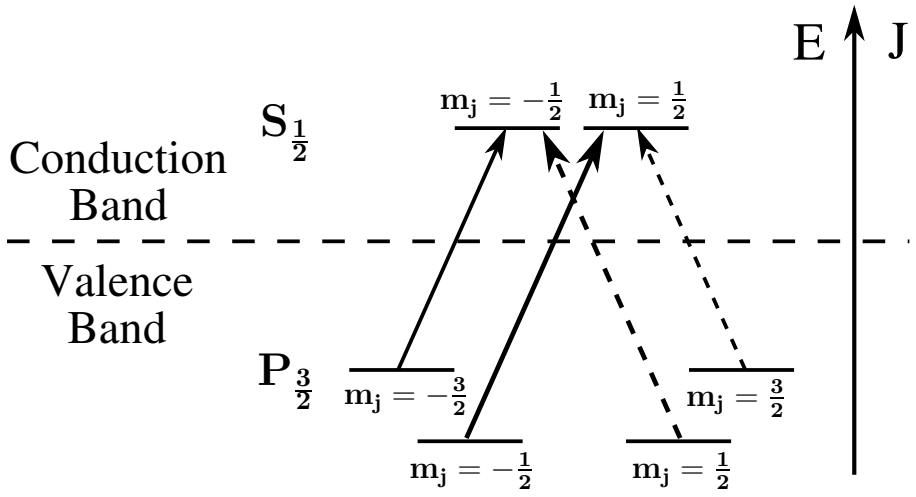

FIG. 2.3: The photo-emission process. Solid and dashed arrows indicate the helicity of the photon needed to cause the transition.

electrons in the valence band ($P_{3/2}$, $m_j = \pm 3/2$) into an available energy state in the conduction band ($S_{1/2}$, $m_j = \pm 1/2$) (Figure 2.3). Electrons escape from the conduction band through a negative work function in the surface. This work function is made negative using a chemical treating process utilizing Cesium.

The main difference between the superlattice cathode, and the bulk and strained layer cathodes used during the first HAPPEx, is the control of the phosphorus doping. This doping is important in splitting the degeneracy that exists for the $P_{3/2}$ levels (e.g. $m_j = -3/2, -1/2$). For the bulk crystal, which lacks this phosphorus doping, beam polarization is limited to 50% because of this degeneracy. The strained cathode introduces a straining substrate layer of GaAsP, below a thin layer of GaAs, sufficient to break this degeneracy. The theoretical beam polarization from the strained layer then becomes 100%, although typically measured around 75%. The main reason for this lower value is understood to be caused by a relaxation of the strain past a certain critical layer thickness, which is about 10 nm. Layers in the superlattice cathode are each smaller than this critical thickness, and are thus less susceptible to this depolarization effect.

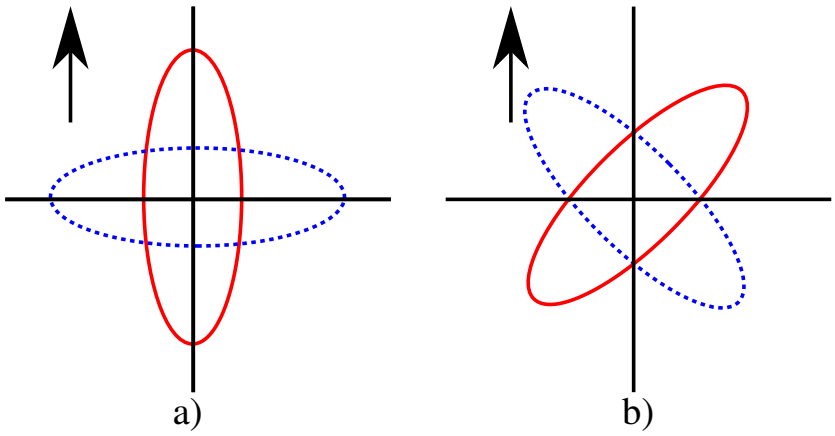

FIG. 2.4: GaAs with a quantum efficiency sensitive to linear polarization with respect to the indicated analyzing power axis (arrow). **a)** Polarization ellipses for positive (solid, red) and negative (dashed, blue) resulting in maximum beam intensity asymmetry. **b)** Polarization ellipses for positive (solid, red) and negative (dashed, blue) resulting in minimum beam intensity asymmetry.

Rotatable half-wave plate

Strain in the superlattice layers cause a quantum efficiency (QE) that is dependent on the orientation of linearly polarized light. This effectively creates an "analyzing power" with respect to an axis lying in the plane of the cathode's surface. Residual linear polarization aligned with this axis can therefore lead to an intensity asymmetry. To minimize this effect, a rotatable half-wave plate (RHWP) is placed just downstream of the Pockels cell, and acts to rotate the major axis of the polarization ellipse with respect to the cathode's analyzing power axis. Figure 2.4 illustrates this technique. An example calibration of this device to determine an optimal RHWP angle is shown in Figure 2.5.

Insertable Half-wave plate

Complementary to the rapid helicity flip provided by the Pockels Cell, an insertable half-wave plate (IHWP) is inserted into or extracted from the laser beamline on a much larger timescale ($\sim$ 1/day). The purpose of this device is to rotate the linear polarization state incident on the Pockels cell by 90°, thereby reversing the fi-

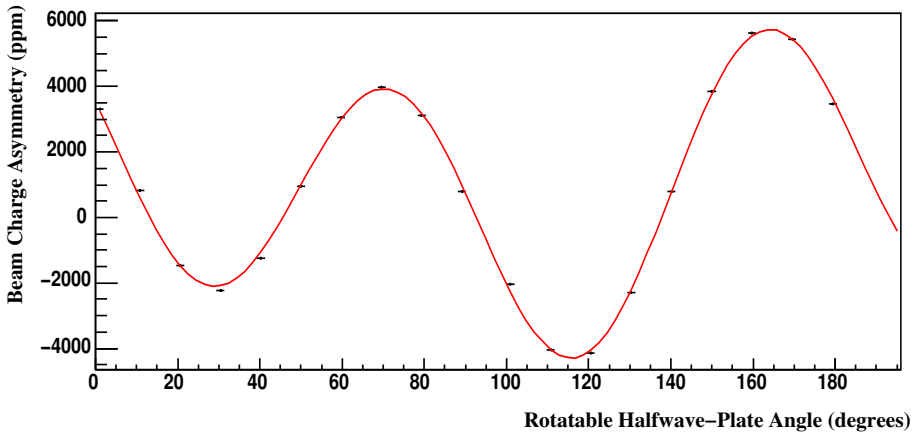

FIG. 2.5: A typical result for the beam Intensity Asymmetry versus Rotatable Half-wave plate Angle.

nal circular polarization of the laser, and thus the polarization of the electron beam, relative to the voltage applied to the Pockels cell. In the absence of any false asymmetries, this action would flip the sign of the measured parity-violating asymmetry observed in the hall. Many possible helicity-correlated systematics are insensitive to the change in IHWP state, so this procedure also provides a means for systematic cancellation.

Intensity Attenuator System

The Intensity Attenuator (IA) is a system devised to control the amount of light that traverses through the laser table optical elements, in a helicity correlated manner. Its main component is a Pockels Cell that operates at a lower voltage than the main Pockels cell. The voltage is varied for specific helicity states by supplying a digital-to-analog (DAC) control offset voltage to the high voltage supply. A rotatable $\lambda/10$-plate, just upstream of the cell, provides a means of control over the maximum amount of attenuation that the system provides, and thus provides a means of changing the system's lever arm over the helicity-correlated laser intensity asymmetry. Linear polarizers are used before and after this system to clean up the linear polarization.

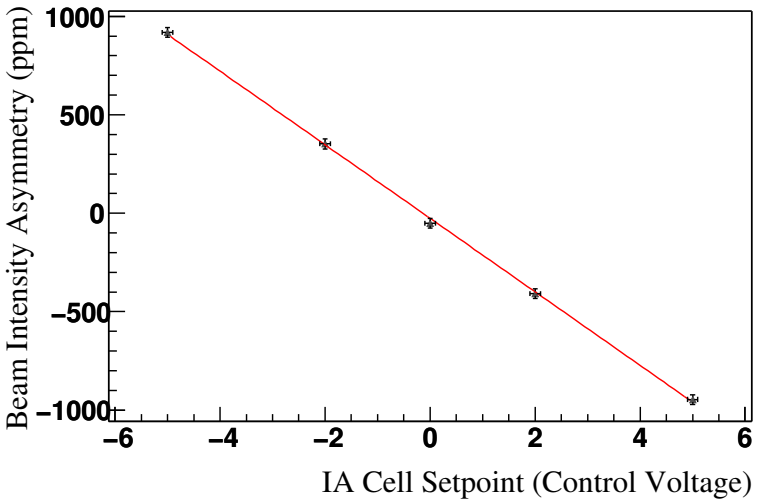

FIG. 2.6: Typical result for the beam intensity asymmetry versus IA control voltage.

A typical relationship between the beam intensity asymmetry and the IA control voltage is shown in Figure 2.6. A similar IA system is also found along the Hall C laser path (not shown in Figure 2.2). Control over the Hall C charge asymmetry is prudent to help minimize helicity-correlated beam systematics that may arise from beam loading in the accelerator.

2.2.2 Spin Precession

The presence of the recirculating arcs in the accelerator and the bending arc along the Hall A beamline introduces a Thomas precession [30] of the beam polarization. This effect takes place whenever there is a component of acceleration that exists perpendicular to the velocity of the particle. The dipole magnets, present along all bending arcs, induce a spin precession angle χ_s according to:

$$\chi_s = \gamma(\frac{g-2}{2})\Delta\theta \tag{2.6}$$

where $\gamma = (1 - v^2/c^2)^{-1/2}$, g is the g-factor of the electron, and $\Delta\theta$ is the bend angle of the beam trajectory. Maximization of the longitudinal polarization observed at the Hall A target (as required for this experiment) is obtained by the operation of

a Wein Filter [31], located in the injector. It operates using a dipole magnetic field to rotate the beam polarization and a perpendicular electric field to zero the net Lorentz force.

2.3 Polarimetry

2.3.1 The 5 MeV Mott Polarimeter

The Mott polarimeter is based on the scattering of high energy electrons scattering from a target with high nuclear charge [32]. A spin-orbit term in the scattering potential arises from the electron experiencing a magnetic field in its rest frame due to the motion of the electric field of the target nucleus. This results in a scattering cross-section that is dependent on the spin of the incident electron:

$$\sigma_{\text{Mott}}(\theta, \phi) = \sigma_u(\theta)(1 + S(\theta)\vec{P} \cdot \hat{n}) \tag{2.7}$$

where $\sigma_u(\theta)$ is the unpolarized cross-section

$$\sigma_u(\theta) = \left(\frac{Ze^2}{2mc^2}\right)^2 \frac{(1-\beta^2)(1-\beta^2\sin^2(\frac{\theta}{2}))}{\beta^4 \sin^4(\frac{\theta}{2})} \tag{2.8}$$

$S(\theta)$ is the Sherman function, and $\vec{P}\cdot\hat{n}$ is the electron polarization component normal to the scattering plane. The Sherman function contains the angular scattering amplitude which includes the spin state of the incident electron and is calculated from the basic electron-nucleus cross-section.

The magnitude of the vertical polarization (P) is gained through the scattering asymmetry, defined as the fractional difference between the number of electrons scattered right versus left:

$$A_{\text{Mott}} = \frac{N_r - N_l}{N_r + N_l} = PS(\theta). \tag{2.9}$$

In practice the Sherman function is corrected for atomic electron screening, and extended target effects.

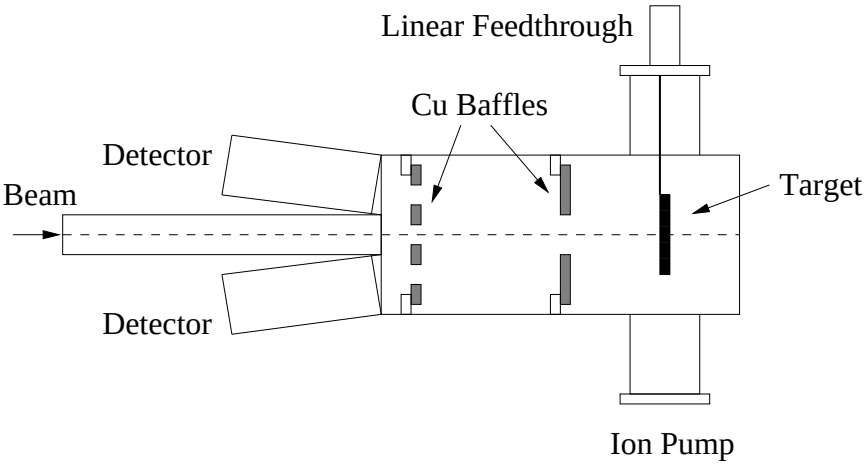

FIG. 2.7: Schematic of the Mott Polarimeter.

The Mott polarimeter (see Figure 2.7) is composed of a dipole magnet (not shown) which deflects electrons in the 5 MeV region of the injector into a scattering chamber. Within the scattering chamber is an aluminum target ladder which contains a standard 0.1 μm gold foil target. Backscattered electrons are measured in four detectors, two in the horizontal and two in the vertical, to measure the right-left and up-down asymmetry, respectively. This provides a simultaneous measurement of P_x and P_y. This measurement, with the aid of the Wein Filter, can be used to infer P_z. Measurement of the beam polarization, using the Mott Polarimeter, is invasive and requires the interruption of beam delivery to all of the experimental halls.

2.3.2 Hall A Møller

Møller polarimetry is based on the scattering of two polarized electrons ($\vec{e}+\vec{e} \rightarrow e' + e'$). The scattering cross-section, in the extreme relativistic limit, depends intrinsically on the beam polarization P^b and target polarization P^t:

$$\sigma_{\text{Møller}} \propto [1 + \sum_{i=X,Y,Z} (A_{ii} P_i^b P_i^t)] \tag{2.10}$$

where $i = X, Y, Z$ are orthogonal projections of the polarization. The analyzing power, defined in the center-of-mass frame, for scattering in the XZ plane is:

$$A_{ZZ} = -\frac{\sin^2\theta_{\rm CM}(7+\cos^2\theta_{\rm CM})}{(3+\cos^2\theta_{\rm CM})^2} \tag{2.11a}$$

$$A_{XX} = -\frac{\sin^4\theta_{\rm CM}}{(3+\cos^2\theta_{\rm CM})^2} \tag{2.11b}$$

$$A_{YY} = -A_{XX} \tag{2.11c}$$

where the Z-axis is defined along the incident electron momentum.

In the Hall A Møller [33], Møller scattering events are produced using a ferromagnetic foil target, where its electrons are polarized in a 24 mT holding field generated by a set of Helmholtz coils. The target foil orientation may be adjusted to measure transverse components of the beam polarization. The target polarization is measured in a dedicated offline procedure, and its uncertainty is the largest of the beam polarization measurement systematics. During the running of this experiment, a target polarization of $(7.95 \pm 0.24)\%$ was used.

Scattered electrons are focused to the Møller detector using a spectrometer (shown in Figure 2.8), consisting of a series of quadrupole magnets and a dipole. This setup allows of a center-of-mass scattering angle range of $75^\circ < \theta_{CM} < 105^\circ$, providing a central A_{ZZ} of about 7/9. After the spectrometer, the electrons are detected in a pair of lead-glass calorimeters where the beam-helicity-correlated detected rate is used to calculate the beam polarization.

Measurement of the beam polarization with the Møller polarimeter is an invasive procedure that takes roughly an hour to acquire a 0.2% statistical accuracy. Beam heating of the target foil, and data acquisition dead-time, limit the beam current to a maximum of about 0.2 μA.

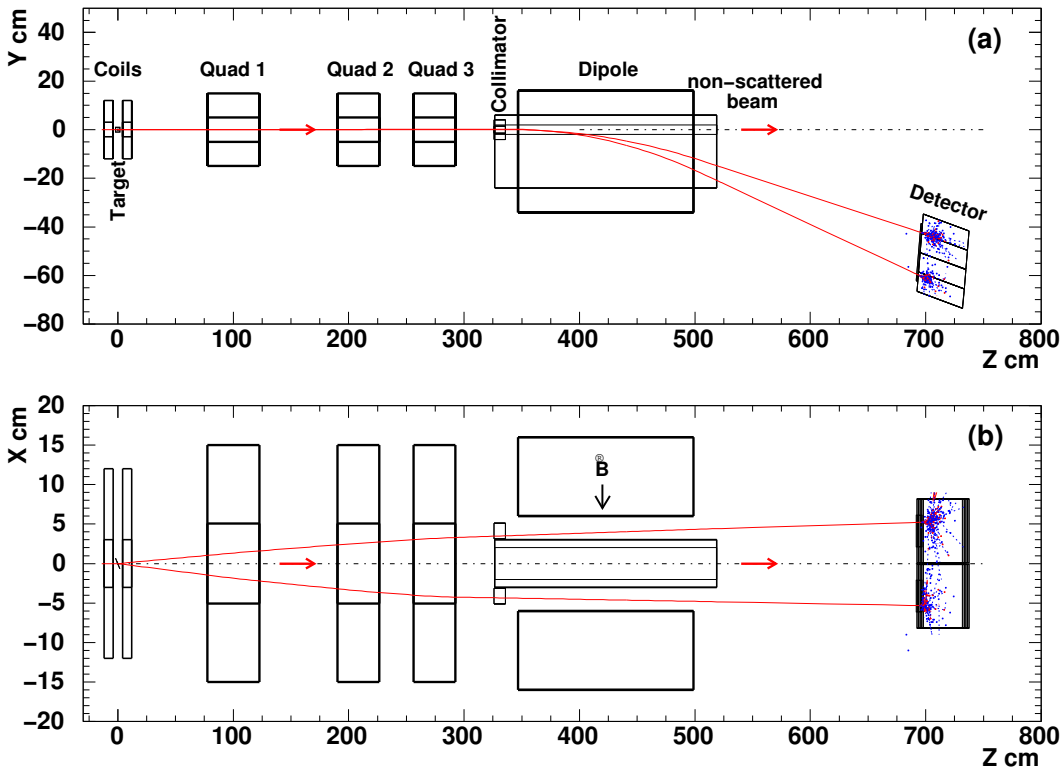

FIG. 2.8: Schematic of the Hall A Møller Polarimeter.

2.3.3 Compton Polarimeter

The Compton polarimeter [34, 35] (Figure 2.9) provides a continuous, non-invasive measurement of the beam polarization using the well-known QED Compton scattering cross-section. The electron beam is diverted into the Compton chicane and interacts with circularly polarized photons. Scattered electrons are deflected into an electron detector using the third dipole, and backscattered photons detected by an electromagnetic calorimeter [36]. The measured beam-helicity-correlated counting rate asymmetry A_{meas} allows for measurement of the beam polarization P_e via:

$$A_{\text{meas}} = \frac{N_+ - N_-}{N_+ + N_-} = A_c P_\gamma P_e \tag{2.12}$$

where A_c is a calculation of the cross-section asymmetry A_c, and P_γ is the photon polarization.

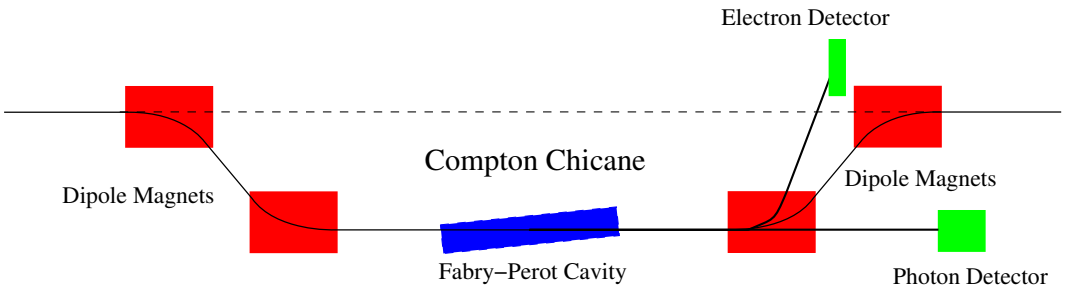

FIG. 2.9: Schematic of the Compton Polarimeter.

To obtain a high signal-to-noise ratio and $\sim 1\%$ statistical accuracy of the beam polarization within 30 minutes, a high photon flux is achieved using a resonant Fabry-Pérot laser cavity [37]. The primary beam from a 230 mW Nd:YaG laser is amplified through this 85 cm cavity using two high-finesse mirrors. The resulting laser power, within the cavity, has been measured to be as high as 1.68 kW.

Maximum luminosity is achieved by optimizing the crossing-angle between the two beams. A designed crossing-angle of 23 mrad places the cavity mirrors about 5 mm from the electron beam. The vertical position of the electron beam is scanned, by varying the dipole fields, until both beams cross at the center of the cavity. Data is acquired for two states of the laser polarization (flipped using a rotatable half-wave plate) as well as states when the cavity is on and off (providing a measure of the background rate). A single electron, a single photon, or a coincidence can trigger the acquisition.

The photon calorimeter (shown in Figure 2.10) is made up of a matrix of 5×5 lead tungstate ($PbWO_4$) crystals (2 cm$\times$2 cm$\times$25 cm) doped with niobium. These crystals were chosen for their fast response (85% of the charge in 25 ns), dense (8.28 g/cm^3), and have a small Moliere radius (2.19 cm). Each are optically isolated and read by a single photomultiplier tube. The energy response of the photon detector is calibrated in a special reference data run using the electron detector as an energy tagger.

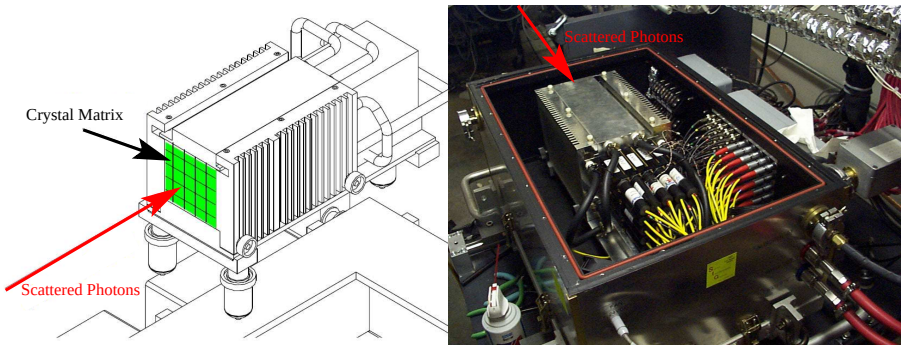

FIG. 2.10: Schematic (left) and photograph (right) of the Compton Photon Calorimeter.

Scattered electrons are detected using four micro-strip planes (shown in Figure 2.11), located just before the fourth dipole. The position within each micro-strip is calibrated to the electron energy using the measured magnetic field integral of the third dipole. Systematic errors that arise from the beam polarization using the electron detector include precise knowledge of this field integral, position of the detector above the beam line, and relative spacing of the micro strips within the detector. The Compton polarimeter thus provides two separate means of determining the electron polarization, with entirely separate systematics.

2.4 Beam-line

2.4.1 Current Monitors

The beam current in Hall A is measured using an Unser monitor and two RF cavities. These devices are enclosed together in a temperature-stabilized box located 25 m upstream of the target. The two cavities are placed symmetrically upstream and downstream of the Unser. The Unser monitor [38] is a parametric current transformer that provides an absolute measure of the beam current. Since the output signal of the Unser is unstable over a period of a few minutes, it is unreliable as a continuous measure of the beam current. It is instead used to calibrate the RF

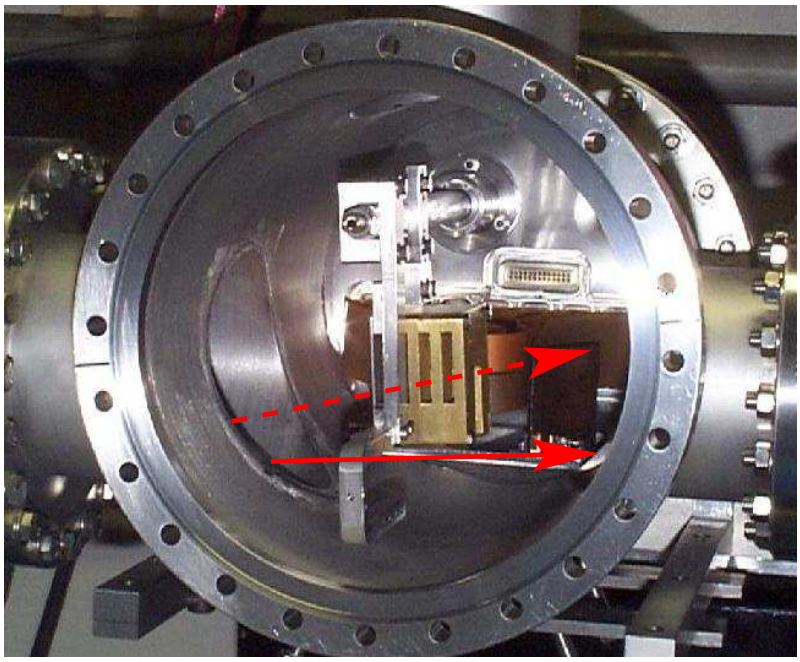

FIG. 2.11: Photograph of the Compton Electron Detector. Red dashed (solid) line indicates the path of electrons that are (not) scattered by the compton process.

cavities.

The RF cavities are two cylindrical waveguides made of stainless steel. The electron beam passing through the cavity excites the resonant transverse electromagnetic mode TM010 at the frequency of the beam. A magnetic field probe is coupled to one of the cavity's resonant modes and provides a signal proportional to the beam current. This signal is processed through a down-converter to obtain a 1 MHz signal, to avoid attenuation from the long cable length to the counting house. The signal in the counting house is passed to an RMS-to-DC converter, whose analog output is then directed to the counting and integrating data acquisition systems.

2.4.2 Position Monitors

Beam position is measured along several points in the 100 keV and 5 MeV region of the injector and five points along the beamline that leads into Hall A. The position of the beam is measured using beam position monitors (BPMs) composed

of four wire antennas oriented parallel to the direction of the electron beam as shown in Figure 2.12 [39, 40]. The antenna are arranged in a square, rotated by 45° from horizontal (except for those located in the 100 keV region).

The RF signal from each wire is processed electronically and yields a DC signal that is proportional to the beam current times the distance between the wire and the beam. Since the antenna signals are proportional to beam current, the signals from opposing wires are multiplexed through the same electronics channel. A gain switching is then used for each channel to keep the DC output signal of approximately constant size regardless of beam current. This method is effective in maintaining similar pedestals and gains between the wires. The beam position (X' and Y') along the axis of the wires is then calculated by a difference over sum of each opposing wire:

$$X' = \frac{\kappa}{2}\left(\frac{X_+ - X_-}{X_+ + X_-}\right), \qquad Y' = \frac{\kappa}{2}\left(\frac{Y_+ - Y_-}{Y_+ + Y_-}\right) \tag{2.13}$$

where the physical distance between the antenna is $\kappa = 37.52$ mm. All of the BPMs, in the injector 5 MeV region and on the Hall A beamline, then require a rotation of 45° to coincide with the lab coordinate system:

$$\begin{pmatrix} X \\ Y \end{pmatrix} = \begin{pmatrix} \cos(45°) & -\sin(45°) \\ \sin(45°) & \cos(45°) \end{pmatrix} \begin{pmatrix} X' \\ Y' \end{pmatrix}. \tag{2.14}$$

2.4.3 Modulation Coils

The electron-helium scattering cross-section is dependent on the beam energy and the detected scattering angle of the incident electron. Since the scattering angle depends on the incident position and angle, small changes in these quantities will create an apparent change in cross-section. If these parameters are beam helicity dependent, this will present itself as a false component to the physics asymmetry.

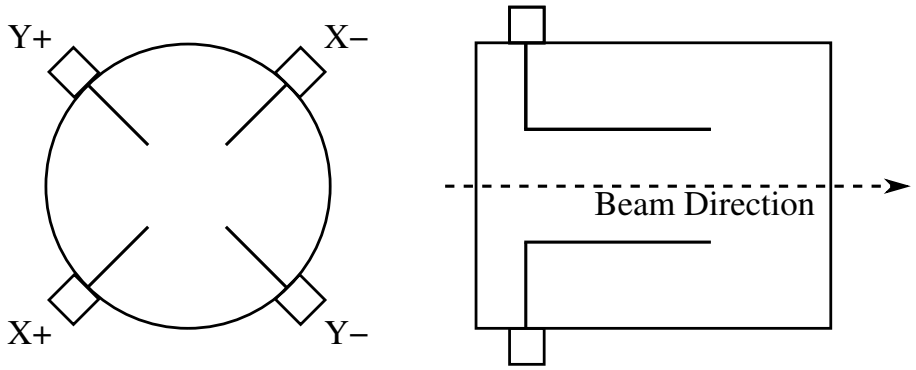

FIG. 2.12: Schematic of a stripline beam position monitor. Left view is looking along the beam axis, right is a side view of the monitor.

Although the goal of the experiment was to keep these helicity-correlated parameters small, it was also necessary to measure the sensitivity of the measured cross-section due to changes in beam parameters in order to make corrections to the physics asymmetry.

To measure the sensitivity of the cross-section to these beam parameters, an automated procedure called beam modulation is used. This procedure uses 7 magnetic coils located several meters upstream of the main bend in the Hall A beamline, and an energy vernier of a cryo-module in South Linac of the accelerator. Every 10 minutes of a production run, the procedure begins what is called a supercycle. Within each supercycle, each modulation coil has its current ramped up and down (Figure 2.13). The final cycle of the supercycle is the modulation of the energy vernier. Each cycle is programmed to be about $3s$, or 100 helicity windows. The response of the beam position monitors and detectors is measured, then deconvoluted to find the detector response to changes in position using the beam modulation analysis (see Section 3.1.3). One of the standard features of the accelerator is the use of Fast Feedback (FFB) to maintain a steady beam position. Because beam modulation causes abrupt changes, FFB was disabled during each supercycle.

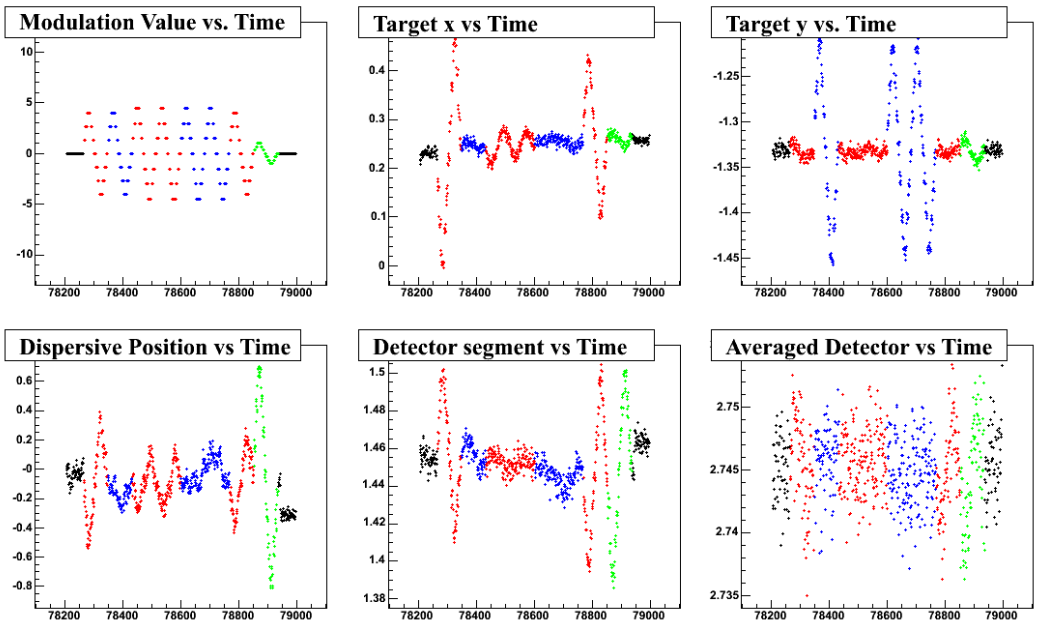

FIG. 2.13: Sample plots of a beam modulation supercycle versus 33.3 ms window number. Red (blue) indicates the modulation of horizonal (vertical) modulation coils. Green indicates the modulation of the energy vernier.

2.4.4 Raster

At high beam intensity, the intrinsic size of the beam (about 100 μm) can produce local heating within the target cell, with the possibility of inducing large density fluctuations. These fluctuations act to increase the detected asymmetry width beyond that expected for counting statistics. Local heating also may compromise the integrity of the target's thin aluminum endcaps. To reduce both of these effects, the heat load is swept over a small area of the target by use of a device called the raster [41].

The raster consists of two magnetic coils located about one meter downstream of the beam current monitor. The coils are oriented to provide a horizontal and vertical deflection. Each coil current is driven with triangular waveforms at different frequencies, with amplitudes set to deliver a rectangular pattern at the target. The width and height of this pattern are set according to the needs and constraints of the

running experiment. For this experiment, the raster dimensions used where 3.5 mm by 3.6 mm.

2.5 Hall A

2.5.1 Cryogenic ^{4}He Target

The electron beam exits the Hall A beamline into a 1.2 m diameter scattering chamber positioned 0.8 m upstream of the spectrometer pivot. To minimize multiple scattering, this chamber is maintained at a 10^{-6} torr vacuum that is vacuum-coupled to the septum magnets and spectrometer (described in Section 2.5.2) entrances.

Scattered electrons from a target pass through a transfer box that connects the chamber to the septum entrance apertures. The box houses a pair of acceptance-defining apertures made of tungsten, designed to limit the amount of direct heating to the septum coils from scattered electrons outside of the acceptance of the septum. Additionally, small ports at the top of the transfer box allow for insertion of a pair of sieve slits used in optimizing the spectrometer reconstruction matrix elements (as described in Section 3.2).

The top of the scattering chamber supports the mechanics for the target ladder and the cryogenic loops. The target ladder (shown in figure 2.14) is made of an aluminum frame, mounted on a motor assembly that allowed for remote control over which target was in position to take beam. The topmost targets are contained within cell blocks, which each block containing a target cell coupled to one of the cryogenic loops. Below the cell blocks, a variety of solid target foils were mounted. A list of the targets used during this experiment is shown in Table 2.1.

The production target, for this experiment, was the 20 cm ^{4}He racetrack cell (the topmost target in Figure 2.14). This cell, specifically designed for this ex-

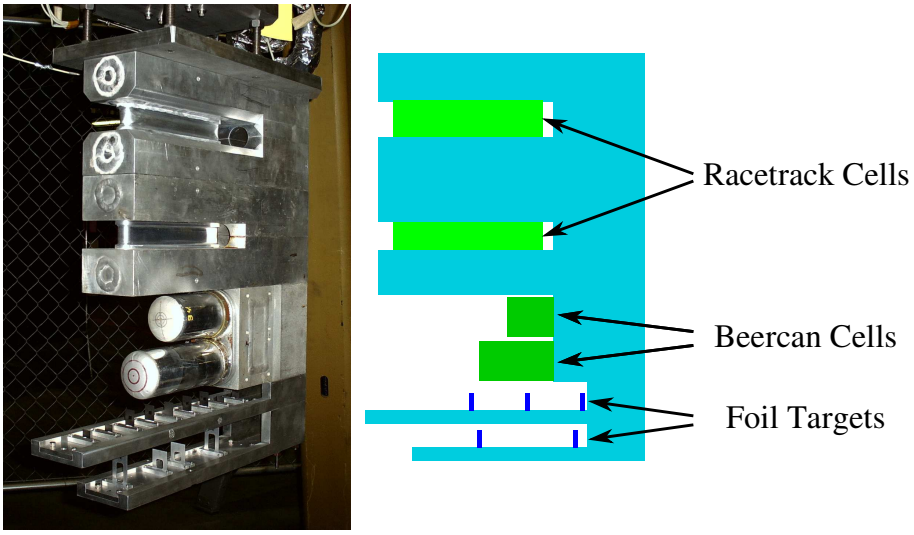

FIG. 2.14: Picture and Schematic of the Target Ladder.

Target	Thickness (mm)	Length (mm)
20 cm ^{4}He	(entr) 0.178 ± 0.02 (exit) 0.213 ± 0.02 (side) 0.290 ± 0.02	19.81 ± 0.02
20 cm LH_2	(entr) 0.178 ± 0.02 (exit) 0.071 ± 0.02 (side) 0.137 ± 0.02	19.95 ± 0.02
Carbon Foils	0.173 ± 0.001	± 12 cm
Aluminum Foils	1.00 ± 0.02	± 10 cm
Single Carbon Foil	0.173 ± 0.001	
BeO	1	

TABLE 2.1: Dimensions of the targets used in this experiment. Thickness values shown for the 20 cm cells are those from the aluminum walls. The BeO target is only used to insure proper beam tune, thus it's thickness is unimportant.

periment [42], features a cryogenic flow transverse to the incoming beam direction. 15 cm and 4 cm beercan cells, used during the first HAPPEx [23], were also included as a standby in case of catastrophic failure of the racetrack cell.

The loop that supplies that target gas, is filled at room temperature with either gaseous ^{4}He or $^1H_2$. This gas is cooled through a heat exchanger that is supplied 4 K ^{4}He from the Central Helium Liquefier (CHL) for the ^{4}He target loop. To maintain a stable target temperature, a fan is used to regulate the target cryogen flow rate. A heater is also inserted into this loop, to maintain the target temperature when beam is not on target.

Changes in the target temperature from the power deposited by the electron beam may lead directly to fluctuations in the target density. The primary result, and the usual concern, is a decrease in the effective target length. This leads to a drop in the experimental detected rate. A greater concern, for this experiment, are density fluctuations that occur on the time scale of the beam helicity flip (30 Hz). Fluctuations of this type result in an additional contribution to the detected asymmetry width of

$$\sigma^2_{\text{meas}} = \sigma^2_{\text{stat}} + \sigma^2_{\text{fluct}}, \tag{2.15}$$

where σ_{stat} is the expected width from counting statistics ($1/\sqrt{N}$) and σ_{fluct} is the width increase due to target density fluctuations.

Dedicated studies were performed [43] during the commissioning of this experiment, in order to determine the optimal operating parameters of the target heater, fan, and density at production beam current. The conclusion of these studies was to operate the target at a sufficiently higher temperature over the 4 K supply, in order to increase the total amount of cooling power. To accomplish this, within the pressure limitations of the cell, the target density was decreased. This amounted to a tradeoff between the decrease in σ^2_{fluct} and loss of rate, causing an increase in σ^2_{stat}.

Parameter	Value
Temperature	6.6 (7.0) K
Pressure	175(195) psi
Density	0.128 g/cm^3
Fan Speed	48 Hz
CHL 4 K Flow	17(4) g/s
Typical Total Power Deposition	$\sim$ 205 W

TABLE 2.2: Operating parameters for the ^{4}He Target. Numbers in parenthesis indicate the operating parameters that changed, halfway through the experiment, due to the cooldown and commissioning of an experiment in Hall C.

The analysis of the asymmetries acquired from the HAPPEx Detectors (Section 2.5.3) and luminosity monitors (Section 2.5.4) determined that the increase in the detected asymmetry width over counting statistics due to target density fluctuations was 2% [44].

2.5.2 Septum Magnets and High Resolution Spectrometers

Hall A is home to a pair of identical High Resolution Spectrometers (HRSs) capable of a momentum resolution at the 10^{-4} level in the 0.8 to 4.0 GeV/c momentum range [33]. Both are capable of switching polarity, offering the ability to investigate, for example, the $(e, e'p)$ reaction. However, this experiment kept both spectrometers at the same polarity and at nearly the same angle of 12.5° in order to double the counting statistics, as well as to provide a left-right cancellation in helicity-correlated beam systematics. A basic schematic of one HRS is shown in Figure 2.15.

Particles entering the HRS are first focused using two superconducting $\cos(2\theta)$ quadrupoles (Q1 and Q2). They then enter a 6.6 m superconducting indexing dipole that features a 45° vertical bend. This bend provides a first order decoupling between a measurement of the position along the target from one of the momentum. Further focusing from a third quadrupole (Q3) is made to provide better resolution of the

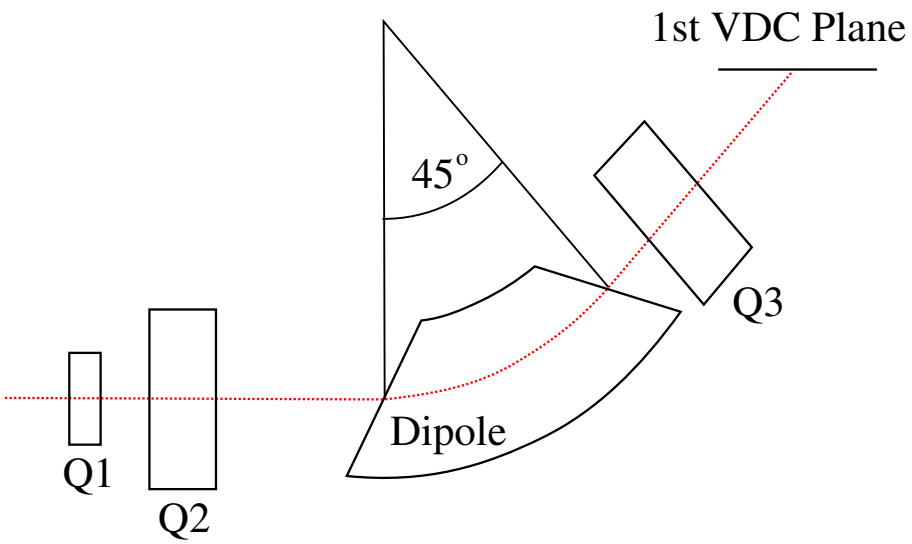

FIG. 2.15: Schematic of the High Resolution Spectrometer from Hall A.

target's horizontal and angular coordinates.

The large size of the HRSs allows only for a minimal central scattering angle of 12.5°. To provide the means for detecting scattered particles at 6°, a pair of pre-bending septum magnets [45] were installed, just upstream of the first quadrupole, and the scattering chamber was moved upstream from its nominal position by 0.8 m (as shown in Figure 2.16). Each septum is made up of superconducting coils with a cryogenically cooled iron yoke. They are designed to have an acceptance of 24 × 54 mSr and provide an central field of up to 4.23 T while preserving an overall spectrometer dp/P resolution of 1×10^{-4}.

Due to space constraints, the upper and lower coils of each septa, were cooled by their yoke via conduction. The consequence of this design was that coil heating from high luminosity targets became an issue. Studies using the ^{4}He racetrack cell determined that the temperature of the coils increased by as much as 4 K, from 4.3 K, at a beam current of 30 μA. The coil temperature trip point was determined to be $\sim$ 7.7 K, so that ultimately production asymmetry measurements were limited to a beam current of about 30 μA.

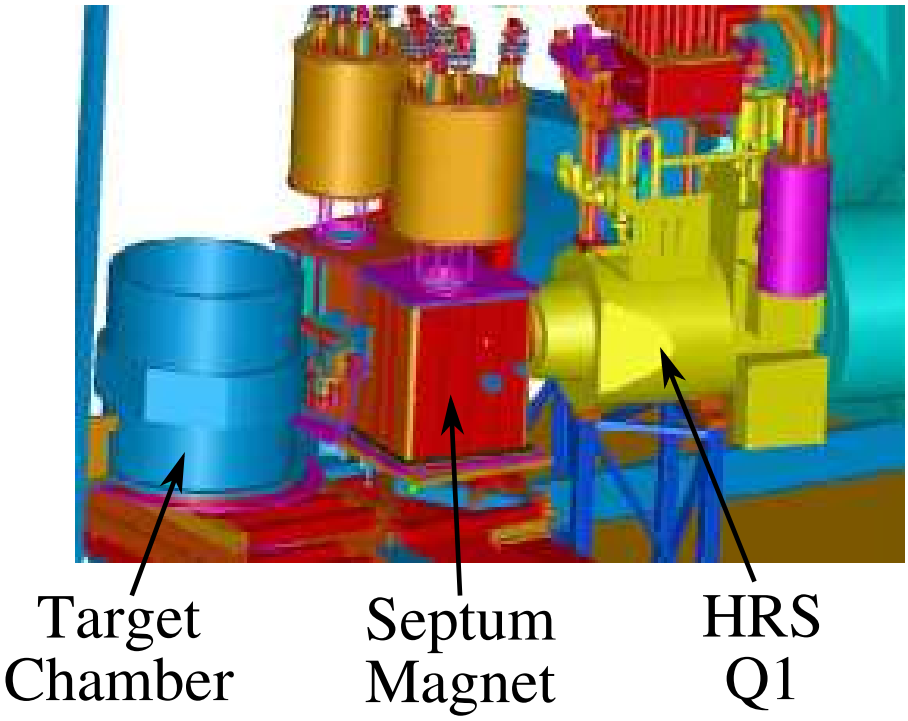

FIG. 2.16: Schematic of the target chamber, septum magnetic, and spectrometer setup to allow for detection of scattered electrons at $\pm 6^{\circ}$.

2.5.3 The Detector Package

The detector packages of the two spectrometers are designed to provide a trigger to activate the data acquisition electronics in order to collect tracking information. Many of the detectors that are used for particle identification (Cherenkov type detectors and lead-glass counters, mentioned in Ref. [33]), were either removed from the detector hut or remained off during this experiment. Figure 2.17 shows a schematic of those detectors used during HAPPEx-^{4}He.

For measurement of Q^2 and backgrounds, individual events are defined as the logical OR of a detected signal from the HAPPEx detector and the scintillator plane. This triggers the read out of the vertical drift chambers (VDCs) to provide the event tracking information. The data taken in this measurement is acquired using the "Counting Mode" data acquisition system, described in Section 2.6.1. For the asymmetry measurement, performed with the "Integrating Mode" data acquisition

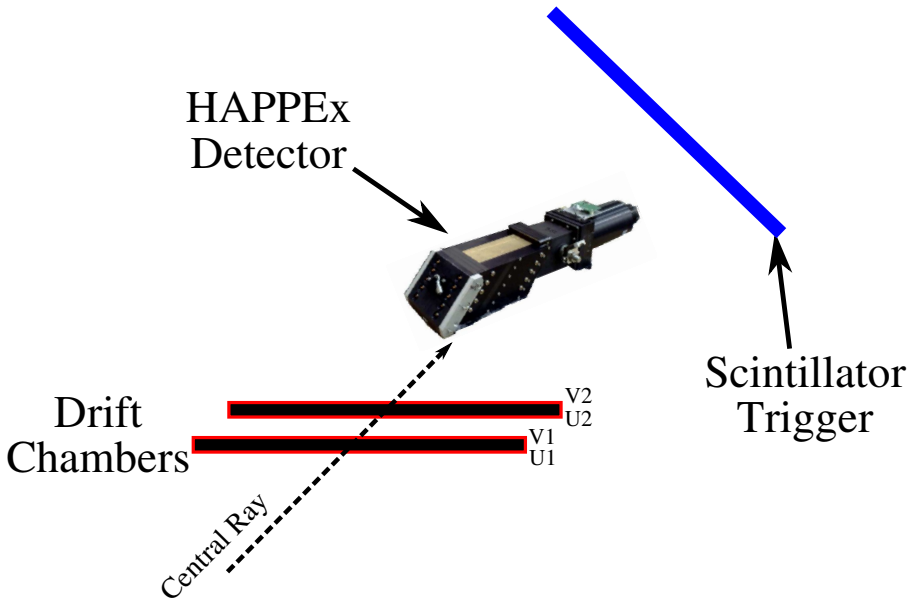

FIG. 2.17: Schematic of the focal plane detectors used during HAPPEx-^{4}He. Drawing is not to scale.

system (Section 2.6.2), the VDCs and scintillator detector are turned off and the HAPPEx detector signal is integrated by a HAPPEx ADC (also described in Section 2.6.2).

Vertical Drift Chambers

The vertical drift chambers [46] serve to provide information on the position and direction of the charged particles that pass through them. Each spectrometer is fitted with a pair of VDCs separated by 335 mm, with each successive plane oriented 90° to one another and inclined such that the nominal particle trajectory crosses them at 45°. The VDCs are filled with a gas mixture of argon (62%) and ethane (38%) with the electric field shaped by gold-plated Mylar planes, kept nominally at −4.0 kV.

Charged particles that pass through the VDCs produce electrons and ions that are accelerated by the negatively charged mylar. As the electrons draw closer to a sufficiently large electric field, they cause additional ionizations of the gas atoms.

A sufficient number of positive ions in the vicinity of a wire drift away, inducing a negative detectable signal. A particle that passes through a VDC typically creates a signal in up to 5 wires. However, due to inefficiencies, only 3 wires are required to provide good track information in that plane.

Scintillator Detectors

The trigger scintillator plane used during this experiment is referred to as S2. It is composed of six overlapping 5 cm plastic scintillator paddles. Each paddle directs light, from a charged particle passing through it, to two photomultiplier tubes (PMTs) situated on opposite sides of the paddle. The S2 plane is oriented such that it is normal to the nominal central particle trajectory.

HAPPEx Detectors

The HAPPEx detectors (shown in Figure 2.18) are total absorption Cherenkov detectors. They are composed of alternating layers of optical and absorbing material [fuzed quartz (SPECTROSIL 2000) and brass, respectively] as shown in Figure 2.19. Each layer is 10 cm wide and 30 cm long. The first brass layer is 4.5 cm thick (3 radiation lengths), with the rest at 1.5 cm. The quartz layers have a thickness of 1 cm. Electrons enter the first absorber and start an electromagnetic shower. When the secondary charged particles of the shower cross the optical medium, they generate Cherenkov photons. These are then reflected through a $\sim$ 20 cm long air light guide and collected into a single Burle 5 inch photo-multiplier tube.

The number of quartz plates were chosen to minimize the energy resolution ($\Delta E/E$) of the detector, as it directly has an impact on the statistical error on the parity-violating asymmetry:

$$\sigma(A_{\mathrm{PV}}) = \frac{1}{\sqrt{N_s}}\sqrt{1+\left(\frac{\Delta E}{E}\right)^2} \tag{2.16}$$

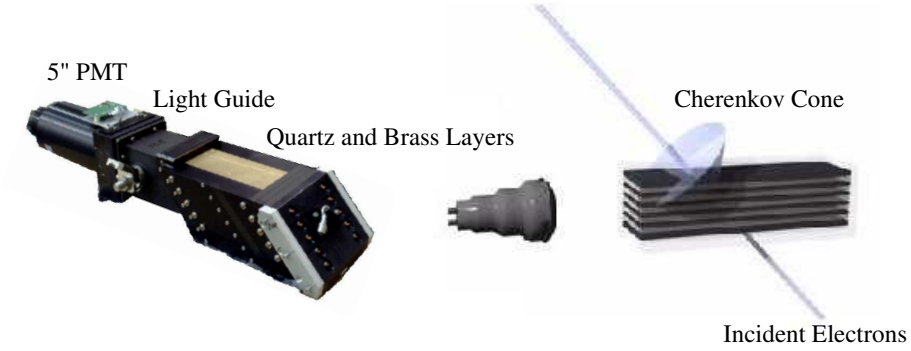

FIG. 2.18: Profile view and schematic of the HAPPEx detector.

FIG. 2.19: Cutaway view of the HAPPEx detector quartz and brass layers.

where N_s is the number of detected scattered electrons. A GEANT3 simulation of the detector with varying number of plates was performed with 3 GeV electrons. A fractional energy resolution ($\Delta E/E$) of 17% was found [47] for 5 quartz plates, contributing about 1.4% to the statistical error.

2.5.4 Luminosity Monitor

The luminosity monitor is made up of 8 Cherenkov detectors located 7 meters downstream of the target. They are symmetrically oriented around the exit beam pipe at intervals of 45°, as shown in Figure 2.20. Each detector utilizes a synthetic quartz radiator ($Si0_2$: Spectrosil 2000) to generate Cherenkov photons directed by a polished aluminum air light-guide into an R7723 photo-multiplier tube. The analog pulse from the PMT is then digitized by a HAPPEx ADC (see Section 2.6.2).

Particles scattered at 0.5° to 0.7° into the luminosity monitor provide the capability of monitoring the effects of target density fluctuations and helicity-correlated beam systematics concurrent with production asymmetry acquisition. Analysis of the central value of the asymmetries acquired from this device is complicated by the magnetic elements that exist, close to the beamline, between the target and this monitor. This is primarily due to electrons that scatter from polarized electrons in magnetized iron having a large asymmetry (as evident in the Møller Polarimeter in Section 2.3.2). For this reason the luminosity monitor in this experiment could not be used to normalize the HAPPEx detector signal, as was done by Ref. [48, 49] to correct for target density fluctuations.

2.6 Data Acquisition

Data for this experiment is acquired utilizing two separate systems, depending on the intended purpose. For alignment of the elastic peak onto the detector,

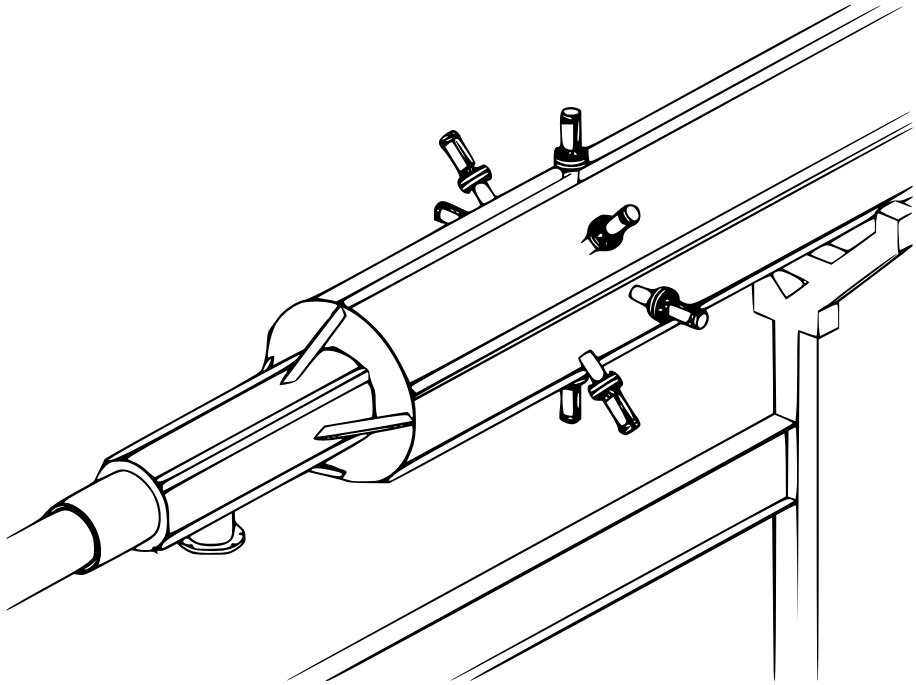

FIG. 2.20: Profile view of the Luminosity Monitor system

measurement of Q^2, and determination of the background caused by rescattering of inelastically-scattered electrons, dedicated low-current ($\sim$ 1 μA) runs are acquired with the standard Hall-A data acquisition system [33] (DAQ). This is the so-called "Counting Mode". For standard HAPPEx asymmetry data acquisition and measurement of the aluminum endcap background contribution, runs are acquired with the HAPPEx DAQ (the so-called "Integrating Mode").

Both DAQs utilize the Jefferson Laboratory data acquisition software package, CODA (CEBAF Online Data Acquisition) [50]. This package, designed specifically for nuclear physics applications, serves to communicate with embedded VME controllers running VxWorks and transfer and encode their acquired data onto a PC running Linux.

HRS Arm	Detector	Trigger Data Mask (hex)
Right	S2	0x2
Right	HAPPEx	0x4
Left	S2	0x8
Left	HAPPEx	0x10
Both	1024 Hz Pulser	0x100

TABLE 2.3: Definition of the Counting Mode triggers.

2.6.1 Counting Mode

The main purpose of the standard Hall A DAQ is to use the S2 scintillator plane and HAPPEx detectors to trigger the readout of the VDCs, in order to provide track reconstruction to the focal plane and to the target. The trigger system is constructed from commercial CAMAC and NIM modules (discriminators, delay units, logic units, and memory lookup units). The S2 trigger is defined from a coincidence detected between two PMTs for a scintillator paddle for any paddle in the S2 plane. The HAPPEx detector trigger is just a detected signal from the detector that provides a voltage over a set threshold. A diagnostic trigger, formed from a 1024 Hz pulser, provides measurement of ADC pedestals. These triggers go to the trigger supervisor module which starts the DAQ readout. Each defined trigger input can be individually prescaled. A summary of the triggers used during this experiment is shown in Table 2.3.

When a trigger is received, integration gates and common-stops are created for the ADCs and TDCs, respectively. Digitized values from these modules are readout for each detector as well as integrated voltage signals from the beam position monitors. These values, as well as a data word containing information on which detector created the trigger, are then encoded to a storage disk.

Additionally, data were acquired using 200 MHz VME scalers and voltage-to-frequency converters (V2Fs) from the beam current monitors. Counts from these scalers are injected into the datastream once every 1-2 minutes.

2.6.2 Integrating Mode

The asymmetry measurement (the so-called "Production Mode" of the experiment) was performed with the Integrating DAQ. The key feature of this mode is the integration of individual beam diagnostic signals (BCMs and BPMs) and detector signals (HAPPEx detector and luminosity monitor) over a large portion of the beam helicity window.

The beam helicity is first determined by an electronics module located near the polarized source. A pseudo-random number generates a binary sequence at roughly 15 Hz, with the beginning line-locked to the 60 Hz phase of the power-line. A resulting "1" generates a NIM voltage level that is transmitted to the Pockel's Cell voltage control electronics, where a "0" is the absence of that voltage. This level is held for 33 ms. The compliment of this binary signal then determines the helicity of the next window. The combination of these two windows defines a helicity pair. To distinguish between the first and second window of this pair, a secondary NIM signal named "PAIRSYNC", is on during the first of the windows and off during the second. A final NIM signal, named "MPS", signals the start of a helicity window and is held for 300 μs. The time width of this signal provides time for the DAQ to allow for the Pockel's Cell to settle into it's helicity voltage. The timing of these signals is summarized in Figure 2.21.

To minimize the possibility for electronics cross-talk, the helicity signal that is sent to the Pockel's Cell is not sent anywhere else in the accelerator. Instead, information about the helicity is delayed by 8 helicity windows, and generates a "Delayed Helicity" signal that is delivered to various DAQs around the accelerator. A simple test to assure oneself that they are receiving and re-sequencing the helicity signal, is to analyze data taken with an intentionally large ($>$ 10000 ppm) beam charge asymmetry. This test also serves to determine the absolute sign of the measured

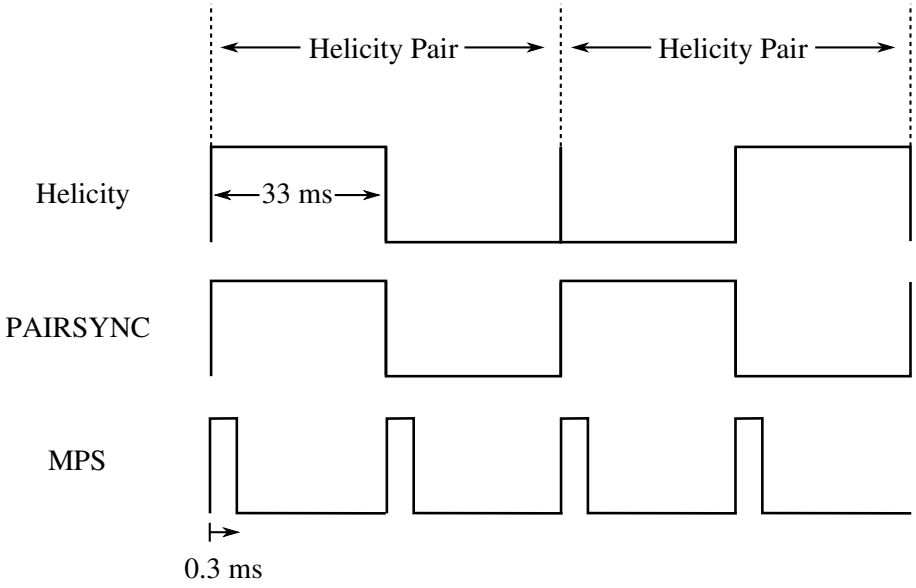

FIG. 2.21: Schematic of Helicity Signals.

detected asymmetry.

The helicity signals, beam diagnostic signals, and detector signals are directed to four HAPPEx DAQ VME crates. Each crate is strategically placed in various parts of the accelerator to provide measurement of various helicity-correlated beam properties and detector asymmetries, while minimizing the induced signal noise that arises from long cable lengths. A rough schematic of the positioning of these crates is found in Figure 2.22.

Each HAPPEx DAQ VME crate contains slots for several 6U and 9U type modules. The signals processed through the VME bus to and from these modules are controlled via a Motorola MVME5100 running a VxWorks 5.4 kernel. This input/output controller (IOC) also facilitates communication with a Linux machine running CODA. In CODA terminology, these are referred to as Read Out Controllers (ROCs). Because of the unique nature of this DAQ, and because the author was heavily involved in the design and implementation of this system, more detail on each module used is provided below.

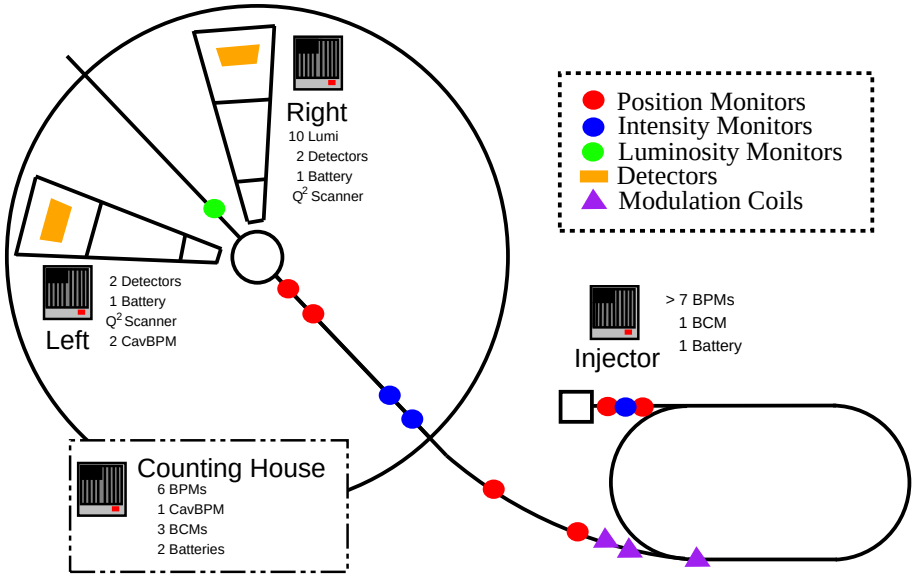

FIG. 2.22: Schematic of HAPPEx Data Acquisition.

HAPPEx timing boards

These modules are a printed circuit board version of the timing boards used during the original HAPPEx experiment [24]. Given the "MPS" signal, in TTL form, the module generates ECL levels indicating the integration gate timing for the HAPPEx ADCs, as well as providing an equivalent integration gate for the scalers. A final ECL output signal "Trigger" is sent to the TIR to trigger readout of a CODA event.

FlexIOs

Designed and constructed at Jefferson Lab, this VME module provides the ability to latch standard ECL input signals, at any point of the helicity window, to be later retrieved during a trigger readout. This module was used to read out the delayed helicity and PAIRSYNC, at the beginning and end of the integration gate. This provides a redundancy check, to insure that the helicity signal did not change in the middle of the gate. Also provided is the ability to send output ECL signals to other data acquisition systems (Compton DAQ, Hall B and Hall C DAQs), in order

to inform them of whether or not a Beam Modulation Cycle (described in Section 2.4.3) was in progress.

V2Fs and Scalers

Voltage to Frequency converters (V2Fs) were designed and constructed for parity experiments done at TRIUMF. An input voltage of $0 - 10$ V is converted to a pulse train whose frequency is proportional to that input voltage. This frequency is fed into a SIS3801 buffering scaler, whose input control provides the capability to provide a veto signal (thus providing a means for an integration gate). These were primarily used in the readout of Injector BPMs and BCMs, a few Hall A BPMs, as well as used in the Synchronization Monitor (Appendix C).

HAPPEx ADCs

The custom analog-to-digital converters (ADCs), designed for the first HAPPEx measurement, performed the primary integration for the signals from the BPMs, BCMs, and detectors. Using the timing signals from the HAPPEx Timing Board, it provides integration of an input analog signal utilizing a "Sample and Hold" technique. A simplistic circuit diagram of the front-end electronics is shown in Figure 2.23. Much more detail of this module is found in Ref [24]. The incoming signal charges one or two capacitors (gain is software selected) in the Integrator stage. The beginning of the charge ramp is sampled first by the Baseline stage and at the end of the ramp with the Peak stage (the sample window is based on the 2.5 μs gate obtained from the Timing Board). The held voltage levels from the Baseline and Peak stages are processed through the Difference stage, which outputs the difference of those two input voltages.

A final summing stage is provided to introduce a pseudo-random voltage from a Digital to Analog Converter (DAC). Special runs are taken to calibrate this pseudo-

random voltage to the corresponding ADC value. This calibration slope is then used to subtract the "DAC" noise in the analysis software. The resulting signal from this summation is converted to a digital number using an ADC. A RESET signal, from the timing board, discharges all of the relevant capacitors so that the process can begin again.

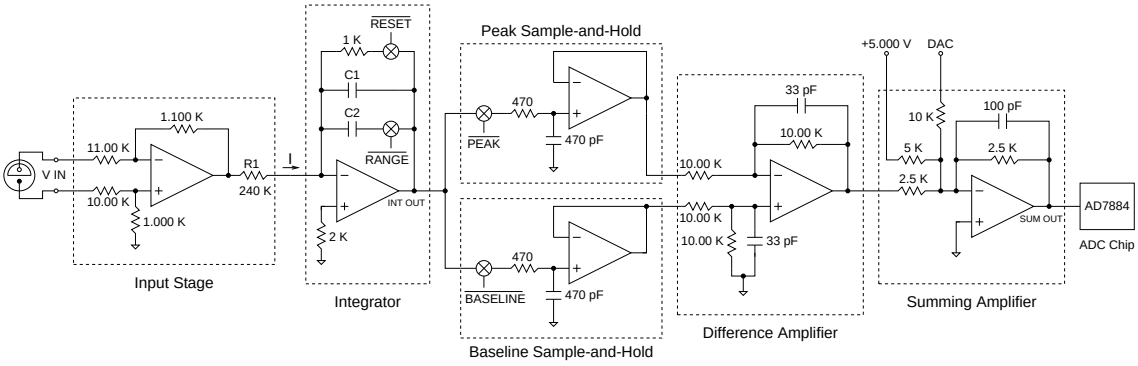

FIG. 2.23: Circuit Diagram of a HAPPEx ADC Channel.

TIR

The VME Trigger Interface (TIR) is a vital hardware component to CODA. It's job is to generate a VME bus interrupt to the ROC to begin the readout of various specified module registers, when it is provided an external ECL trigger. This module can be programmed to operate in two separate modes, stand-alone mode and trigger-supervisor mode. In stand-alone mode, the external ECL trigger arrives from the timing board at the end of the integration window. In trigger-supervisor mode, the trigger arrives from the trigger supervisor. This module also contains registers that allow for readout of input ECL (latched at trigger) and setting of output ECL to allow for control signals to other VME modules, or to be used in monitoring the size of total readout time.

Trigger Supervisor

The Trigger Supervisor is another module designed at Jefferson Lab that enables one to tie multiple crates together into the CODA framework. It acts to supply each crate with a common trigger, thus synchronizing the events between each crate. This module is located in its own crate, and due to its proximity to the Counting House crate uses the Counting House crate's trigger from its Timing Board, as an external trigger. This signals the TS to send a trigger to each ROC. Each ROC then performs a readout (with its ISR) and relays back to the TS that it has been completed (to acknowledge that it is ready for a new trigger).

To check the synchronization of each crate, a synchronization system was constructed, checked and verified frequently during the experiment (Appendix C).

CHAPTER 3

Analysis

Jefferson Laboratory experiment E00-114, HAPPEx-^{4}He, took data in June, 2004. This chapter will describe the analysis of the raw data to extract physically meaningful information. First, the extraction and correction of the detected asymmetry will be described. This will be followed by determination of the central 4-momentum transfer squared (Q^2) and the beam polarization. Details on the analysis of backgrounds and linearity will be discussed. Also, a prescription on the determination of the effective kinematics will be presented. This chapter concludes by putting all this information together to extract the measured physics asymmetry.

3.1 Asymmetry Analysis

3.1.1 Raw Asymmetry

Raw detector asymmetry analysis was mainly performed using the Parity Analyzer (PAN) [51]. This analysis software, written in C++ utilizing ROOT [52] libraries, performed a variety of low-level analysis tasks:

- Decode raw CODA data and map these to defined monitors and detectors.

- Pedestal and DAC noise subtraction for ADC and scaler channels.
- Remove the 8-window delay from the delayed helicity signal received from the polarized source, and synchronize the helicity signal with events.
- Define cut intervals and perform cuts entirely based on the raw beam parameters.
- Form helicity asymmetries and differences from pairs of helicity windows and their complement.

Cuts on the data at this stage were performed before helicity pairs were used to calculate asymmetries and differences, and were made up of three separate categories:

- Incorrect helicity sequence.
- Beam current below a set threshold.
- Beam intensity shifts beyond a set threshold.

Each cut category was associated with a cut interval, to remove a set number of helicity-windows preceding the cut condition as well as a set number of helicity-windows allowing for recovery from the cut condition. Figure 3.1 shows a sample cut interval imposed when the beam current dropped below a set threshold. Cuts performed outside of the PAN framework were also made for longer periods of time due to equipment malfunction: DAQ failures, spectrometer magnet trips, and incorrect spectrometer field settings.

The raw asymmetry was calculated for each detector, for each window pair, by:

$$A_{raw} = \frac{D_R/I_R - D_L/I_L}{D_R/I_R + D_L/I_L} \tag{3.1}$$

where R, L indicate the assigned helicity for the window and D/I is the digitized detector signal divided by the digitized signal from the beam current monitor. Figure 3.2 shows the resulting raw asymmetry for each detector. The difference in RMS width between the left and right arm is primarily due to their slight difference in Q^2. This motivated the decision to weight the final corrected asymmetry by Q^2 for

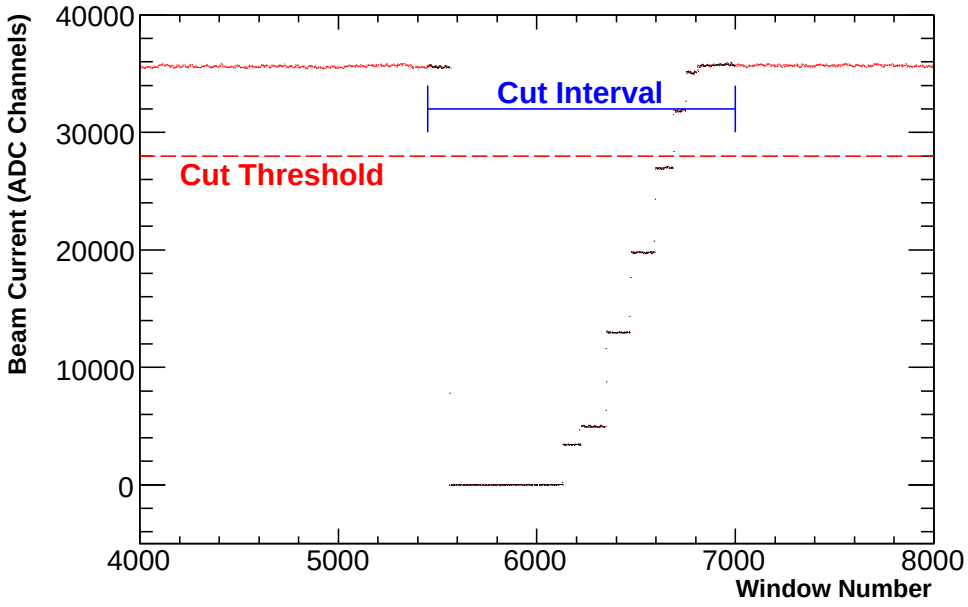

FIG. 3.1: Sample plot of beam current versus helicity-window number, showing how cut intervals are imposed. Windows outside of the interval are included in the calculation of asymmetries, whereas those inside are excluded. The cut interval in this plot is exaggerated for clarity.

each spectrometer arm. The difference in the number of pairs is primarily due to spectrometer magnet trips and incorrect spectrometer field settings. Non-statistical tails in the distributions were found to be correlated to helicity-correlated beam position differences and were later removed with the beam modulation correction (Section 3.1.3).

3.1.2 Passive Helicity Reversal

The insertion of the $\lambda/2$-plate at the polarized source (as described in Section 2.2.1) was toggled roughly every 24 hours, so that nearly half of the data were taken in each state. Because the DAQ and analysis software is unaware of this passive flip, the sign of the physics asymmetry flips but it's magnitude remains the same. Observation of this flip for the measured asymmetry becomes an important test and provides significant cancellation of possible false asymmetry contributions, as many

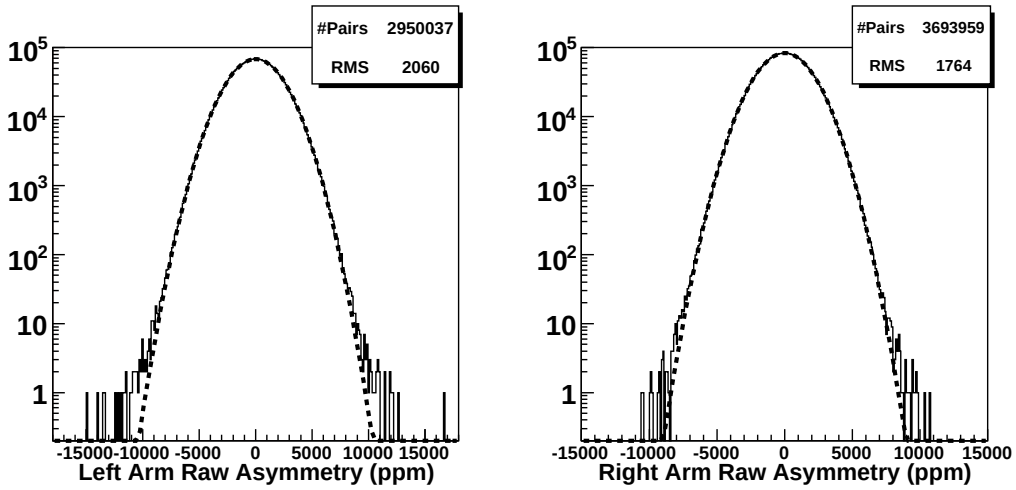

FIG. 3.2: Raw detector asymmetry for each spectrometer arm. The non-statistical tails in the distributions were found to be removed with the beam modulation correction. The dashed line is a fit to a Gaussian function.

helicity-correlated beam systematics are unaffected by this change.

The measured raw asymmetry for each $\lambda/2$ dataset is shown in Figure 3.3. A clear correlation between the raw asymmetry and $\lambda/2$ state is observed.

3.1.3 Beam Modulation Analysis

The false component of the raw asymmetry arising from helicity-correlated variations in the beam position, angle, and energy on target was calculated and corrected for using the beam modulation technique outlined in 2.4.3. With carefully set up beam optics along the transport line to the target, beam position monitors **4BX**, **4BY**, **4AX**, **4AY**, and **12X** provide a nearly orthogonal set of observables that span the space of the above-mentioned beam parameters. Utilizing this, the asymmetry correction was calculated from

$$\Delta A = \sum_{i=1}^{5} \left(\frac{\partial \sigma}{\partial M_i} \right) \Delta M_i, \tag{3.2}$$

where the slope, $\partial\sigma/\partial M_i$, is the normalized detector sensitivity to the i^{th} beam position monitor, and ΔM is the measured helicity-correlated beam position difference.

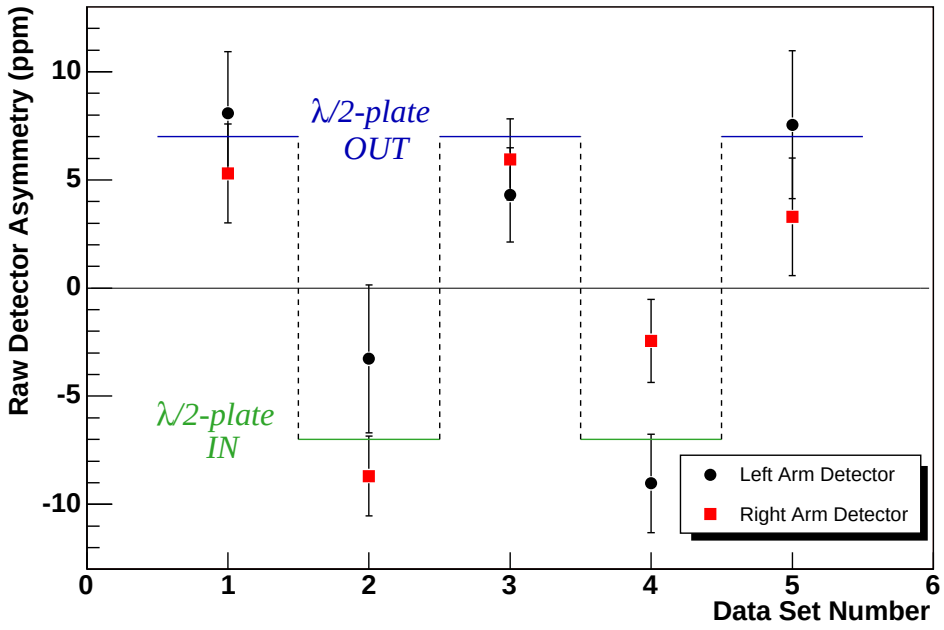

FIG. 3.3: Raw detector asymmetry for each $\lambda/2$ dataset, for each spectrometer arm. The $\lambda/2$ plate is inserted for each even-numbered dataset and the data clearly show the expected sign-change in the detected physics asymmetry.

The slopes were determined by first considering an expansion of the normalized detector sensitivity to the j^{th} modulation coil in terms of the beam position monitors,

$$\frac{\partial\sigma}{\partial C_j} = \sum_{i=1}^{5} \left(\frac{\partial\sigma}{\partial M_i}\right)\left(\frac{\partial M_i}{\partial C_j}\right). \tag{3.3}$$

Extraction of $\partial\sigma/\partial M_i$ was obtained by defining the χ^2:

$$\chi^2 = \sum_j \left[\left(\frac{\partial\sigma}{\partial C_j} - \sum_{i=1}^{5} \frac{\partial\sigma}{\partial M_i}\frac{\partial M_i}{\partial M_i}\right)/\sigma^2\right]^2, \tag{3.4}$$

and minimizing it with respect to $\partial\sigma/\partial M_i$ to find

$$\sum_j \left(\frac{\partial\sigma}{\partial C_j}\frac{\partial M_k}{\partial C_j}\right)/\sigma^2 = \frac{\partial\sigma}{\partial M_i}\sum_j \left(\frac{\partial M_i}{\partial C_j}\frac{\partial M_k}{\partial C_j}\right)/\sigma^2. \tag{3.5}$$

This is rewritten in matrix form as

$$\mathbf{D_C} = \mathbf{D_M}\mathbf{M_C}, \tag{3.6}$$

by making the following definitions:

$$\begin{aligned} \mathbf{D_C} &= \sum_j \left(\frac{\partial \sigma}{\partial C_j} \frac{\partial M_k}{\partial C_j} \right) / \sigma^2 \\ \mathbf{D_M} &= \frac{\partial \sigma}{\partial M_i} \\ \mathbf{M_C} &= \sum_j \left(\frac{\partial M_i}{\partial C_j} \frac{\partial M_k}{\partial C_j} \right) / \sigma^2. \end{aligned} \tag{3.7}$$

Calculation of the detector sensitivities $\mathbf{D_M}$ involves just a matrix inversion:

$$\mathbf{D_M} = \mathbf{D_C} \mathbf{M_C^{-1}}. \tag{3.8}$$

It is apparent here that it is crucial that the beam optics do not result in a singular $\mathbf{M_C}$ (i.e. $|\mathbf{M_C}| \neq 0$). Measured normalized detector sensitivities ($\partial\sigma/\partial M_i$) are shown in Table 3.1.

The signs and magnitudes of these sensitivites are indicative of the how symmetric the spectrometers are aligned. Because the spectrometers bend electrons away from the horizonal plane, each X sensitivity should have opposite signs between the two arms, with larger magnitudes than the Y sensitivites. The sensitivities to the energy dispersive BPM (12X) is the same sign between the two arms, because of the nearly identical magnetic optical properties of the spectrometers. Differences in the magnitudes between specific sensitivites are attibuted to the difference in Q^2 between each arm, and slightly different detector alignments in the spectrometer focal planes.

Each measured raw detector asymmetry pair was corrected using the measured slopes, to reduce the asymmetry width and remove non-statistical tails caused by helicity-correlated beam systematics, according to

$$A_{\text{corr}} = A_{\text{meas}} - \Delta A. \tag{3.9}$$

Figure 3.4 shows the result of this correction. These results were compared to those obtained using the matrix regression method outlined in Appendix B, in order to

Monitor	Left Arm Detector Sensitivity (ppm/μm)	Right Arm Detector Sensitivity (ppm/μm)
4BX	-34.3 ± 0.2	34.5 ± 0.2
4BY	2.6 ± 0.3	0.6 ± 0.3
4AX	21.2 ± 0.1	-9.8 ± 0.1
4AY	-0.6 ± 0.1	-0.1 ± 0.1
12X	-2.58 ± 0.02	-1.91 ± 0.02

TABLE 3.1: Normalized detector sensitivities to beam parameters as obtained from the beam modulation analysis. Errors here are statistical.

Monitor	Left Arm Detector Correction (ppm)	Right Arm Detector Correction (ppm)
4BX	0.29	-0.21
4BY	0.00	0.00
4AX	0.32	-0.09
4AY	-0.01	0.00
12X	-0.07	-0.03
Total	0.53	-0.32

TABLE 3.2: Detector asymmetry corrections to beam parameters using the beam modulation analysis.

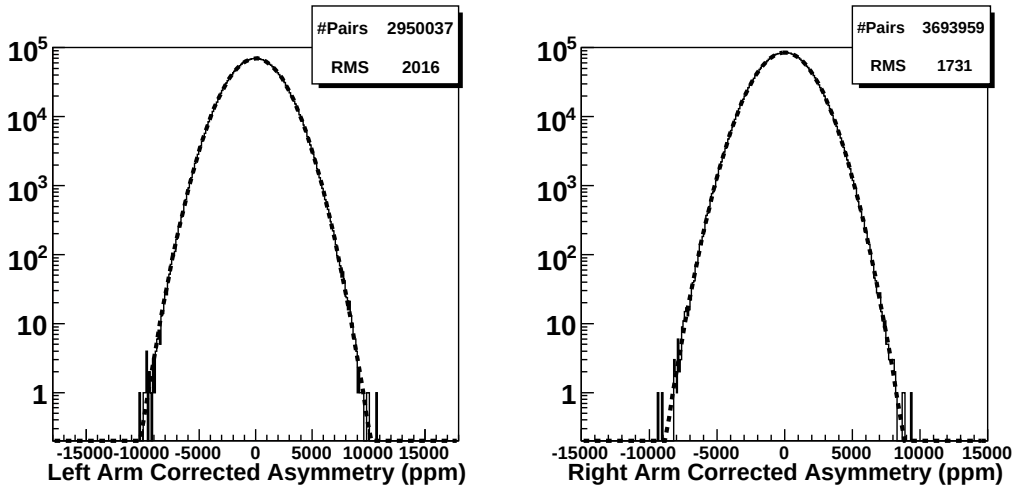

FIG. 3.4: Detector asymmetry for each spectrometer arm, corrected using the beam modulation analysis. The dashed line is a fit to a Gauassian function. Note the absence of the non-Gaussian tails observed in Figure 3.2.

gauge the size of the systematic error of this correction. Table 3.3 shows a summary of this comparison. The size of the correction made using the beam modulation method for each detector for each monitor is shown in Table 3.2. Each correction is much smaller than the overall statistical error in the measured asymmetry. Given the stability of the detector sensitivies over time, the systematic error due to this correction was conservatively estimated as 0.070 ppm for the position and angle BPMs (4B and 4A) and 0.050 ppm for the energy dispersive BPM (12X).

Spectrometer Arm	Raw (ppm)	Beam Modulation Corrected (ppm)	Regression Corrected (ppm)
Left	6.37 ± 1.18	5.84 ± 1.16	5.77 ± 1.16
Right	5.18 ± 0.91	5.50 ± 0.89	5.47 ± 0.89

TABLE 3.3: Comparison of the raw, beam modulation corrected, and regression corrected asymmetry for each spectrometer arm. Errors shown are statistical.

3.2 Q^2 determination

The four-momentum transfer (Q^2) is a measure of the 4-momentum transferred via a virtual particle from the incident electron to the target nucleus. For elastic scattering,

$$Q^2 = -\left(\mathbf{E} - \mathbf{E}'\right)^2 = 2EE'(1 - \cos\theta), \tag{3.10}$$

where E is the incident electron energy, E' is the scattered electron energy ($E' \gg m_e$), and θ is the scattering angle. This section details how E, E', and $\cos\theta$ were measured, to provide a determination of Q^2. Precise determination of this value is crucial since the asymmetry (from Equation 1.68) is a linear function of Q^2

3.2.1 Beam Energy

The energy of the beam was determined by measuring the deflection of the beam in the arc region of the beamline. This region is comprised of eight dipole magnets that bend the electron beam from the linac by a nominal 34.3° into Hall A [33]. When the beam is tuned into the so-called "dispersive" mode in this region, the momentum p of the beam is determined by

$$p = k\frac{\int \vec{B} \cdot \vec{dl}}{\theta}, \tag{3.11}$$

where $k = 0.299792\,\text{GeV rad T}^{-1}\,\text{m}^{-1}\,\text{c}^{-1}$, the numerator is the dipole field integral, and θ is the bend angle (in radians).

The procedure [33] is made up of concurrent measurements of the magnetic field integral and bend angle. An identical ninth dipole, separate from the beamline, is used to measure the field integral. The bend angle is measured by using wire scanners to determine the position of the beam throughout the arc.

During this experiment, one measurement was performed, which yielded the

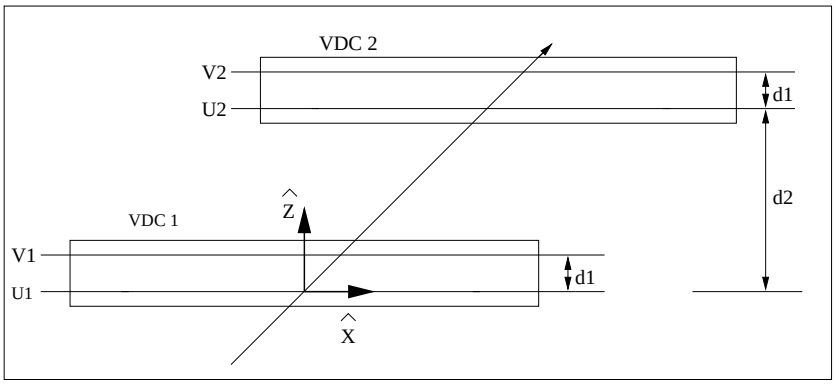

FIG. 3.5: Detector Coordinate System. The origin, as shown, is defined at the intersection of wire 184 of the VDC1 U1 plane and the perpendicular projection of wire 184 of the VDC1 V1 plane. The $\hat{y}$-axis is into the page.

result

$$E = 3.0258 \pm 0.00032 \text{ (stat)} \pm 0.0006 \text{ (syst) GeV}.$$

A final error of 3 MeV was ascribed to beam energy for the running period. This larger error is conservative, based on the history of energy measurements and drifts in the accelerator setup, but accounts for some uncertainty in dE/dx energy losses in the target.

3.2.2 Optics Optimization

Using the "Counting Mode" DAQ, events located by the vertical drift chambers of each spectrometer, yield two spatial coordinates (x_{det} and y_{det}) and two angular coordinates (θ_{det} and ϕ_{det}) (shown in Figure 3.5), defining an event track. These tracks are then corrected for any detector offsets from the ideal central track and transformed into the focal plane coordinates (x_{fp}, y_{fp}, θ_{fp}, ϕ_{fp}). A complete description of the coordinate systems used in Hall A are found in Ref. [53]. These track observables are used to calculate the coordinates at the target (y_{tg}, θ_{tg}, ϕ_{tg}, δ) shown in Figure 3.6.

Optimization of the determination of these target variables is done through a procedure using foil targets (which define a set of well-defined interaction points

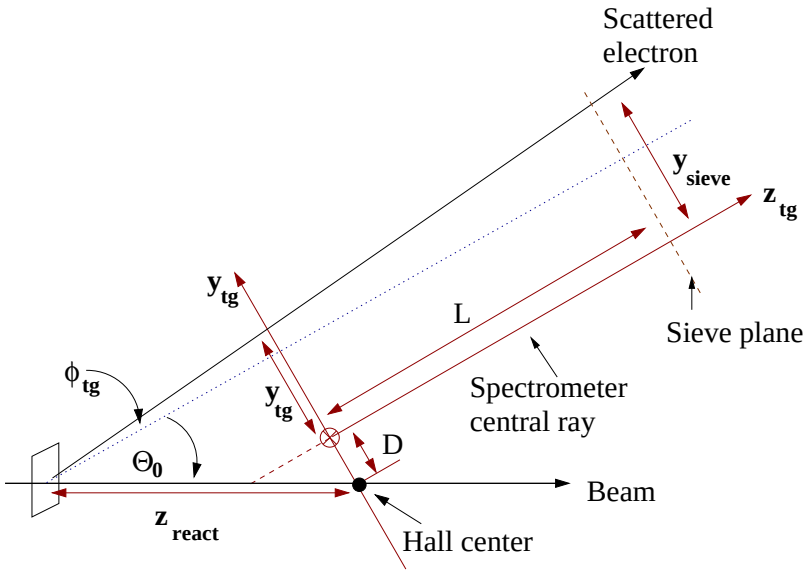

FIG. 3.6: Target Coordinate System

along the beam) and a sieve-slit collimator (Fig. 3.7) located at the entrance to the first magnetic element of each spectrometer. A set of tensors (Y_{jkl}, T_{jkl}, P_{jkl}, D_{jkl}) links the focal plane coordinates to the target coordinates according to [53]

$$y_{tg} = \sum_{jkl} Y_{jkl} \theta_{fp}^j y_{fp}^k \phi_{fp}^l \tag{3.12a}$$

$$\theta_{tg} = \sum_{jkl} T_{jkl} \theta_{fp}^j y_{fp}^k \phi_{fp}^l \tag{3.12b}$$

$$\phi_{tg} = \sum_{jkl} P_{jkl} \theta_{fp}^j y_{fp}^k \phi_{fp}^l \tag{3.12c}$$

$$\delta = \sum_{jkl} D_{jkl} \theta_{fp}^j y_{fp}^k \phi_{fp}^l, \tag{3.12d}$$

where the tensors are polynomials in x_{fp}, e.g.

$$Y_{jkl} = \left(\sum_{i=0}^{m} C_i x_{fp}^i \right)_{jkl} . \tag{3.13}$$

In practice, these polynomials can be up to fifth order. A χ^2 minimization, utilizing MINUIT [52], is used to determine best tensor values. These data are obtained

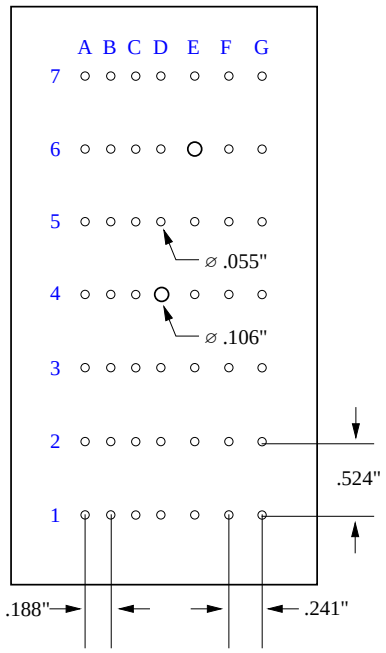

FIG. 3.7: Sieve Slit geometry.

from special optics runs, utilizing the sieve-slits, using three separate target configurations: a single ^{12}C foil, two ^{12}C foils with 12 cm spacing, and two ^{12}C foils with 24 cm spacing.

Optimized sieve patterns (θ_{tg} vs. ϕ_{tg}), for the left and right spectrometers, using the single ^{12}C foil are shown in Fig. 3.8. Line crossings in this figure indicate the calculated sieve hole locations. Optimized sieve patterns for the left spectrometer using the two ^{12}C foils with 12 cm spacing are also shown in Fig. 3.9.

For the most part, the data line up well with the expected sieve slit hole locations. The central row, however, appears to be shifted compared to the other rows. This "kink" is believed to be an artifact of an imperfection in the septum coil windings on the beamline side, which is difficult to model with polynomials.

A determination of the contribution to the systematic error in Q^2 due to imperfect spectrometer optics was made by applying *ad hoc* corrections to the observed patterns in order to remove the small deviations from their expected locations. For the optimization calibrated at the nominal target center ($z = 0$) the

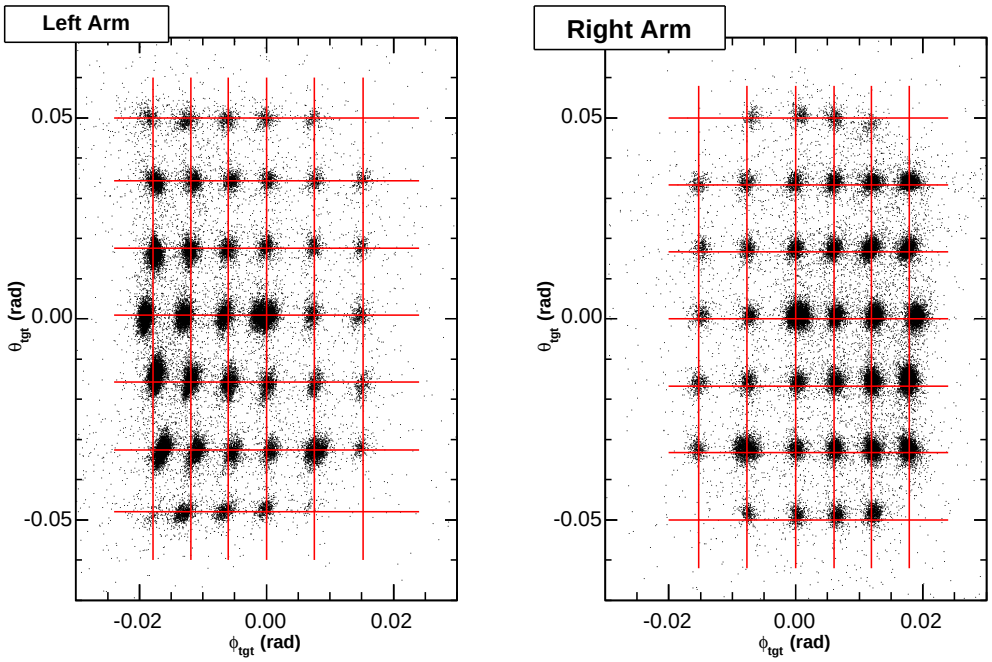

FIG. 3.8: Sieve Slit data from the single ^{12}C foil target.

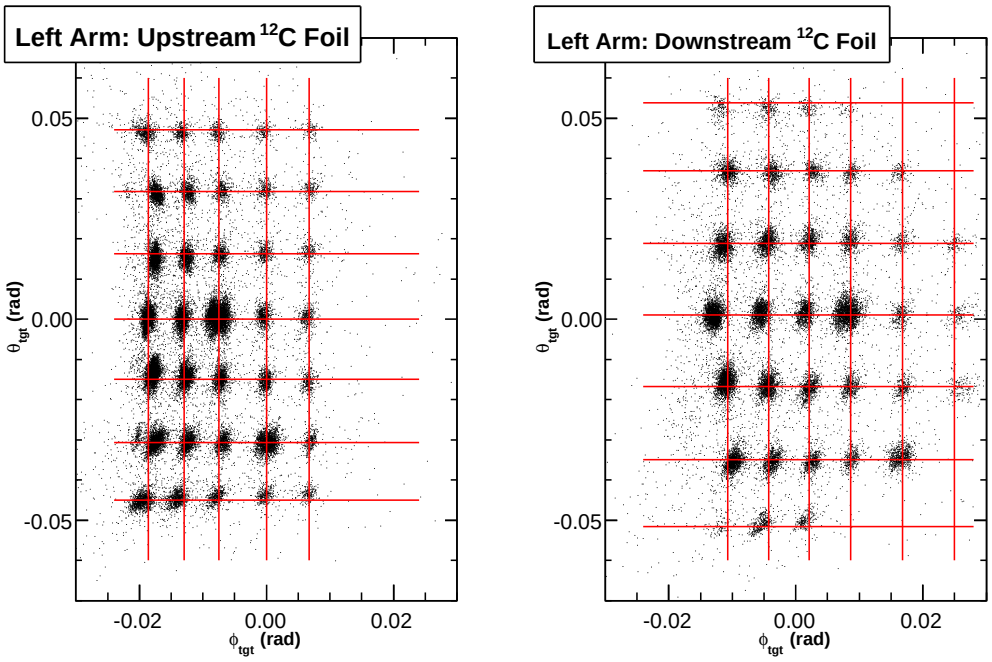

FIG. 3.9: Sieve Slit data for the Left Arm from carbon foils, 6 cm upstream and downstream from the nominal target center.

average of these small deviations was found to be $\Delta\phi_{tg} = 0.081 \pm 0.58$ mrad and $\Delta\theta_{tg} = 0.66 \pm 1.40$ mrad for the left spectrometer, and $\Delta\phi_{tg} = 0.017 \pm 0.41$ mrad and $\Delta\theta_{tg} = 0.89 \pm 1.10$ mrad for the right spectrometer. Applying these corrections to the measured angles, Q^2 was observed to shift by 0.1%. This shift was assigned as the systematic error for the $z = 0$ optics optimization, however the correction was not applied for the final Q^2 result.

A similar procedure was used to determine the z-dependence of the optics optimization error, using the optimization calibrated with extreme target foil locations ($z = \pm 12$ cm). The observed shift was 0.5% of Q^2 and was taken as a conservative estimate of the systematic error.

3.2.3 Central Scattering Angle

Particular attention was paid to the determination of the central scattering angle, due to it possibly being the largest contributor to the systematic error in Q^2. Relying on an optical survey accuracy of 0.05° would have resulted in a systematic error contribution of 1.3%. A new method, relying on measurement of scattered electrons from different target nuclei, yielded better accuracy for the spectrometer central angles. A water cell was used for this measurement, due to its large momentum lever arm between the hydrogen and iron scattering states. This target was a 0.5 mm thick container of flowing water, with 1 mil steel windows.

The relation between the energy of the scattered electron (E'), beam energy (E_0), the mass of the target nucleus (m), and the scattering angle (θ) is obtained from:

$$E' + \epsilon' = \frac{E_0 - \epsilon_0 - \frac{1}{2m}(m^{*^2} - m^2)}{1 + (E_0 - \epsilon_0)/m(1 - \cos\theta)}, \tag{3.14}$$

where m^* indicates the mass of the recoil state, and ϵ_0 and ϵ' are energy losses due to ionization within the target. Table 3.4 provides a summary of the targets used in

Target	Material	Density (mg/cm^2)	Ionization dE (MeV)
Single Carbon foil	^{12}C	200	0.66
Water cell	0.001 inch Steel window	20	0.06
	5mm H_2O	500	1.87
	0.001 inch Steel window	20	0.06
	Total:	540	1.99

TABLE 3.4: Target density and energy loss due to ionization for the targets used for the central scattering angle determination.

the angle determination, along with an estimate of the energy loss due to ionization (calculated from the Bethe-Block equation). The total energy loss due to ionization (dE) was assumed to be equally divided between ϵ_0 and ϵ'.

The reconstructed scattered electron energy for each peak in the spectra from the carbon and water-cell targets was fit, for the central sieve hole, using

$$f(E') = \sqrt{\frac{\pi}{2}}\frac{\sigma}{\alpha}\exp\big[\frac{1}{2\alpha}(\sigma^2/\alpha + 2(b-E'))\big]\mathrm{Erfc}(\frac{|\alpha|}{\sqrt{2}\sigma\alpha}(\sigma^2/\alpha + (b-E'))), \quad (3.15)$$

where α describes an exponential fall-off, σ is the width of the Gaussian, b is the peak of the un-smeared distribution, $\mathrm{Erfc}(z)$ is the complimentary error function, and E' is the reconstructed energy of the scattered electron,

$$E' = P_0(1 + \delta + \Delta\delta). \quad (3.16)$$

P_0 is the central momentum setting of the spectrometer, δ is the fractional difference of the reconstructed momentum from P_0, and $\Delta\delta$ is a second-order correction to take into account local imperfections in the optics optimization. The sieve holes are open to a finite range of scattering angle, leading to a correlation between the observed in-plane scattering angle θ_{tg} and δ (as shown in Figure 3.10). A *kinematic correction* was found to be required for the hydrogen elastic peak due to its large nuclear recoil. This correction to the central hole was calculated based on the observed correlation

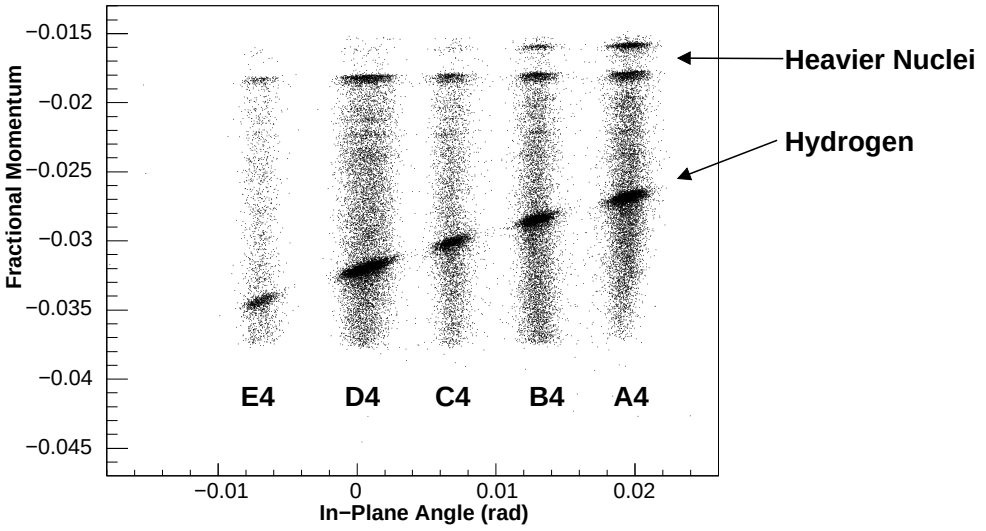

FIG. 3.10: Observed correlation between the relative scattered momentum δ and the in-plane scattering angle $\theta_{\rm tg}$, for the water-cell target. Scattering from hydrogen has a noticably larger correlation than the heavier nuclei (^{16}O, ^{56}Fe), due to larger target recoil. Data shown are for scattered electrons through the central sieve slit row (4) for the right spectrometer.

in the central row of holes, and resulted in a systematic shift in the central scattering angle of 0.015°. Figure 3.11 shows a sample scattered momentum distribution with the fit generated from Eqn. 3.15. Table 3.5 shows the beam energy and nuclear masses used as fixed parameters to this fit.

The overall average angle observed by the spectrometers, for the optics runs on the single ^{12}C foil and water-cell, was found to be $5.94 \pm 0.02°$ for the right and $6.13 \pm 0.02°$ for the left. These are comparable, but not in agreement within errors, to the results from survey: $5.87 \pm 0.05°$ and $6.05 \pm 0.05°$.

3.2.4 ADC Weighting

In production mode, the asymmetry measurement is implicitly weighted by the energy deposited by the incoming electron into the HAPPEx detector. This energy is dependent on the angle of the Cherenkov cone (and therefore the angle of the incoming electron), as well as the distance of the incoming electron from the PMT.

Parameters	Value (MeV)
E_0	3025.0
$m(^1\mathrm{H})$	938.27
$m(^{16}\mathrm{O})$	14895.08
$m(^{16}\mathrm{O}_{3^-}) - m(^{16}\mathrm{O})$	6.13
$m(^{16}\mathrm{O}_{2^+/1^-}) - m(^{16}\mathrm{O})$	7.12
$m(^{12}\mathrm{C})$	11174.86
$m(^{12}\mathrm{C}_{2^+}) - m(^{12}\mathrm{C})$	4.44
$m(^{12}\mathrm{C}_{0^+}) - m(^{12}\mathrm{C})$	7.65
$m(^{12}\mathrm{C}_{3^-}) - m(^{12}\mathrm{C})$	9.64
$m(^{56}\mathrm{Fe})$	52089.78
$m(^{56}\mathrm{Fe}_{2^+}) - m(^{56}\mathrm{Fe})$	4.32

TABLE 3.5: The parameters fixed parameters used in the fit of the E' distributions. Nuclear masses and mass differences obtained from Ref. [54].

To account for the integrated detector signal weighting, the reconstructed Q^2 was weighted by the detector's ADC value using

$$Q^2 = \frac{\sum Q_i^2 W_i}{\sum W_i}, \tag{3.17}$$

where W_i is a weight factor for event i and Q_i^2 is the corresponding measurement. The weight factor is simply the detector ADC value with its pedestal subtracted. It was found that this scheme resulted in a shift in Q^2 of $(-0.1 \pm 0.1)\%$. The assigned 0.1% systematic error was conservatively made from the size of the shift.

3.2.5 Miscellaneous Errors

Absolute calibration of the spectrometer momentum scale was accomplished when the spectrometers were commissioned [55]. The error in this scale was assumed to be 5 MeV, which is consistent with the shifts in missing mass observed during the 2004 Hydrogen measurement [56].

Drifts in Q^2 could not be directly observed, because the limited running time of the 2004 Helium dataset allowed for only one measurement. However, the drift in Q^2 from the longer running 2004 Hydrogen measurement was found to range

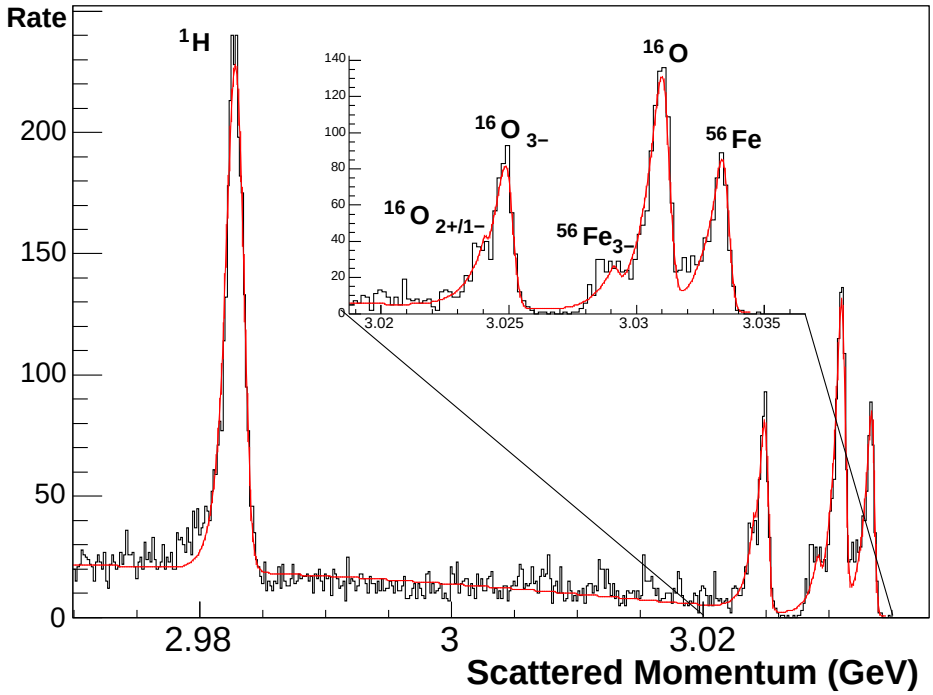

FIG. 3.11: A fit to the reconstructed scattered electron energy from the central sieve hole of the Right HRS, using the water-cell target, after kinematic corrections.

from -0.1% to 0.4%. Qualitatively, these could have been caused by drifts in the spectrometer and septum fields or difference in the incident beam angle on target. Using this observation, a generous systematic error of 0.2% due to these drifts was assigned.

The effect of "pileup", events which contained more than one VDC track, was estimated by comparing the Q^2 of single track events versus that obtained by allowing multiple tracks. A shift of $(-0.23 \pm 0.10)\%$ was observed, where the systematic error was taken from the error assigned to this correction from multiple runs for the 2004 Hydrogen measurement.

	Left	Right
Central Angle	$5.94^\circ \pm 0.02^\circ$	$6.13^\circ \pm 0.02^\circ$
Q^2 ((GeV/c)^2)	0.0939 ± 0.0009	0.0892 ± 0.0009

TABLE 3.6: Central Angle and Q^2 Summary for each spectrometer

Error Source	Error (in source units)	Percent Error in Q^2
Beam Energy	3 MeV	0.1%
Optics Optimization:		
At Z = 0		0.1%
Z dependence		0.5%
Scattering Angle	0.02°	0.7%
ADC Weighting		0.1%
HRS Momentum Scale	5 MeV	0.2%
Drifts in Time		0.2%
Pileup		0.1%
Total Systematic Error		1.0%
Statistical Error		$\leq$0.1%
TOTAL ERROR		1.0%

TABLE 3.7: Summary of Errors in Q^2

3.2.6 Q^2 Summary

Figure 3.12 shows the Q^2 distribution (before ADC weighting) for each spectrometer arm. Table 3.6 shows a summary of the central angle and resulting Q^2 after weighting and corrections are applied. Table 3.7 presents a summary of the error budget for the Q^2 determination.

3.3 Beam Polarization

The Compton Polarimeter, described in Section 2.3.3, provided continuous, non-invasive beam polarization measurements used to normalize the corrected asymmetry. Analysis of the scattered electron events was complicated due to imprecise knowledge of the field integral of the third dipole, as well as the relative vertical position of the electron detector above the beamline. Therefore, due to the limited

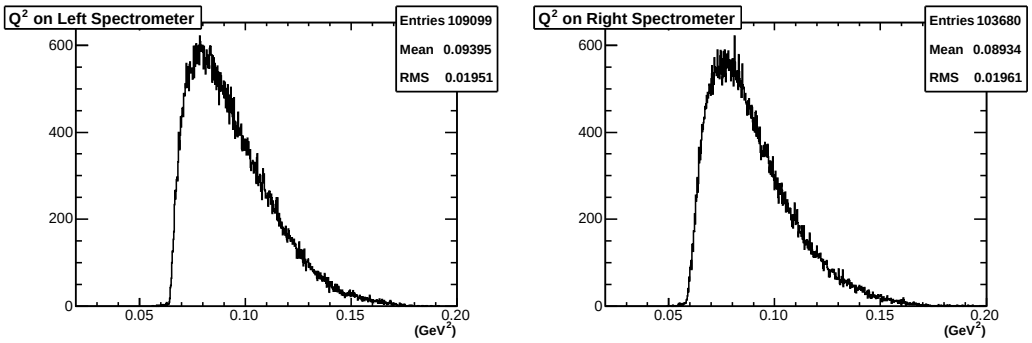

FIG. 3.12: Q^2 distribution for the 2004 run, before ADC weighting.

statistical precision of the helium physics asymmetry, further work beyond the online analysis was not performed, and the beam polarization was extracted from the online analysis of the scattered photon asymmetry from the photon calorimeter.

The average beam polarization, obtained from the photon analysis, over the entire dataset was $(86.9 \pm 1.7)\%$. The dominant systematic contributing to this error arose from knowledge of the laser polarization at the Compton interaction point (CIP). The degree of circular polarization (DOCP), at this point, was inferred from measurements of the DOCP at the laser exit line (as shown in Figure 3.13) utilizing a $\lambda/4$-plate and two Integrating Spheres. This DOCP was then translated to the CIP by use of a transfer function that was carefully studied and measured when the system was installed [35].

This result is consistent within error with the independent measurement of $(85.9 \pm 3.0)\%$ obtained with the Møller Polarimeter (Section 2.3.2). The stability of the beam polarization as measured by the Compton Polarimeter is shown in Figure 3.14. This was sufficiently stale over this short run so that a single average value for the polarization for the entire data set could be adopted.

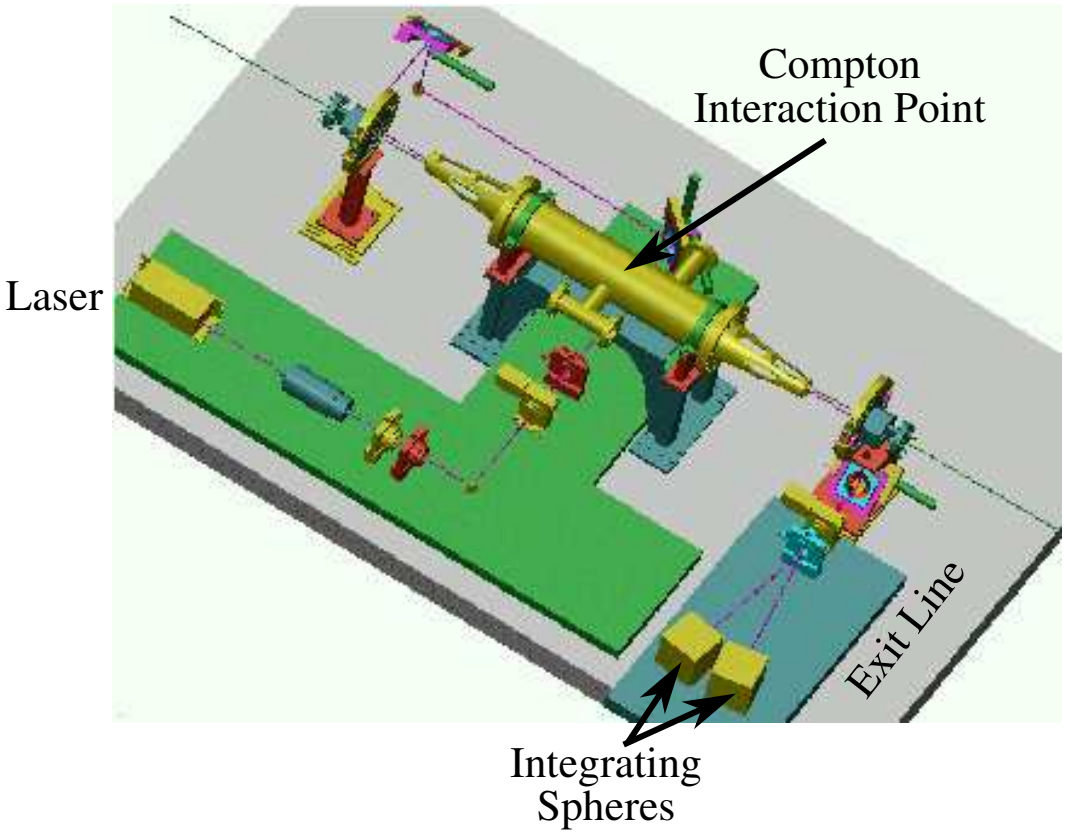

FIG. 3.13: Compton Polarimeter Optics Setup.

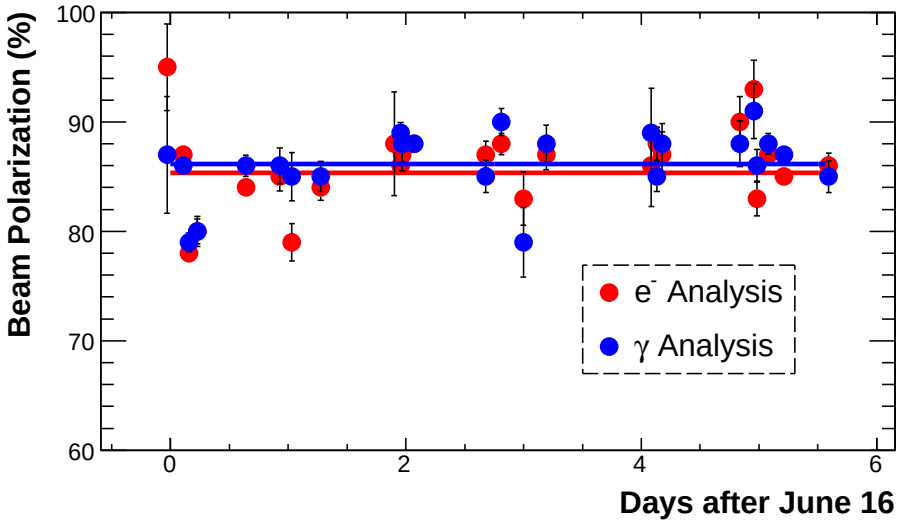

FIG. 3.14: Plot of the beam polarization as measured by the Compton Polarimeter versus time.

3.4 Backgrounds

One challenge for a measurement of an asymmetry using integrated signals is the estimation of background contamination. The advantage of using the high resolution spectrometers is that the dispersion of the dipole maps kinematic separation at the target into spatial separation at the focal plane. Detectors can then be oriented to maximize signal from the elastic peak, while minimizing contribution from inelastically scattered background. The dominant backgrounds for this experiment were quasielastic scattering from the target aluminum end-windows, quasielastic scattering from ^{4}He, inelastic scattering through the Δ resonance, and pole-tip scattering of the spectrometer magnets.

3.4.1 Target Aluminum End-Windows

Quasielastic scattering from the target aluminum end-windows was estimated with the use of two aluminum foils separated by 20 cm, nick-named the Aluminum Dummy. The ratio of the thickness of the target end-windows to the foil thickness was $x_t = 0.098 \pm 0.014$. This roughly accounted for the dE/dx radiative losses of the Helium within the ^{4}He target cell. To determine the fraction of aluminum quasielastic events that contributed to the integrated detector signal we used the relation

$$f_{\mathrm{Al}} = x_t \frac{D_{\mathrm{Al}}}{D_{^4\mathrm{He}}}, \tag{3.18}$$

where D_{Al} is the normalized rate of detected events from the Aluminum Dummy, and $D_{^4\mathrm{He}}$ is the normalized rate from the ^{4}He target cell. Using the "Integrating Mode" DAQ, this fraction was measured to be $(0.67 \pm 0.10)\%$ and $(0.65 \pm 0.10)\%$ for the left and right arm detectors, respectively. The asymmetry from quasielastic scattering from aluminum was calculated [17] to be -1.6 ppm with a 50% error assumed. The parity-violating asymmetry from quasielastic scattering from aluminum was not

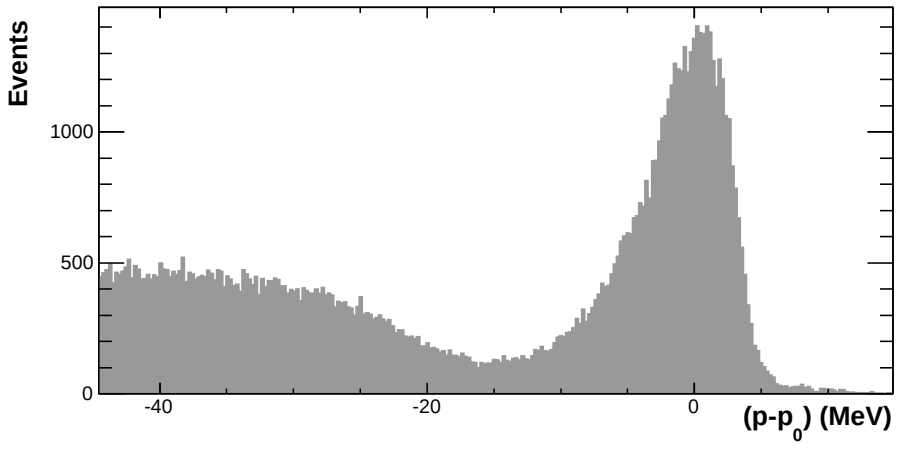

FIG. 3.15: Measured momentum difference from the central momentum (p_0) of one spectrometer from ^{4}He. Quasielastic scattering from ^{4}He dominates the spectrum at low momenta.

measured because of the small size of the background fraction and the enormous amount of time to required to acquire enough statistics.

3.4.2 ^{4}He Quasielastic Scattering

The largest component of the asymmetry background was from inelastic scattering from ^{4}He. The energy threshold for quasielastic scattering from ^{4}He has been calculated to be 19.7 MeV [57]. The reconstructed momentum spectrum in Figure 3.15, as acquired from the "Counting Mode" DAQ, shows that this limit is close to where a rise above the radiative tail from the elastic peak (caused by radiative losses, such as ionization) is observed. It is also evident, in this spectrum, that the elastic peak is cleanly separated from the quasielastic threshold. Bound excited states which also should appear around -19.5 MeV, are not visible due to either poor resolution or having a small cross-section at the experimental kinematics.

Because the spectrometers map the electron's scattered momentum into the dispersive coordinate of the focal plane, the quasielastic background fraction was estimated in this coordinate system by observing its rise near the low-momentum

edge of the detector.

Detector Location and Orientation

The HAPPEx detector was installed in the spectrometer focal plane, centered on the expected central ray of the spectrometer. To evaluate its absolute position and angle in focal plane coordinates, a series of low beam current, counting mode DAQ (2.6.1) runs were taken with carbon and aluminum foil targets as well as the ^{4}He cell. The spectrometer momentum set-point was selected in order to place the relatively flat quasi-elastic spectrum in the center of the focal plane, fully illuminating the region covering the HAPPEx detector. A resulting focal plane distribution from the racetrack cell is shown in Figure 3.16. The HAPPEx detector angles, were found to be consistent for each target configuration, and were -24.5° and 23.0° for the right and left arm spectrometers, respectively. The focal plane coordinates were then rotated by these angles to arrive into the HAPPEx detector coordinate system. The resulting distribution in this coordinate system provides insight into the detector acceptance along its dispersive coordinate.

Detector Edge Model

Figure 3.17 shows the HAPPEx detector triggering from quasielastic scattering from carbon as observed along the detector's dispersive axis. The rate has been normalized to the flat center of the detector where it is not affected by the detector edges. The fall-off on either side of the dispersive axis is indicative of loss of deposited energy and loss of trigger rate from the detector hardware supporting the copper and quartz plates. This fall-off is modeled using a third-order polynomial (fit shown in red) to the low-momentum edge of the detector, which is the edge closest to the ^{4}He quasielastic region when the elastic peak is centered on the HAPPEx detector.

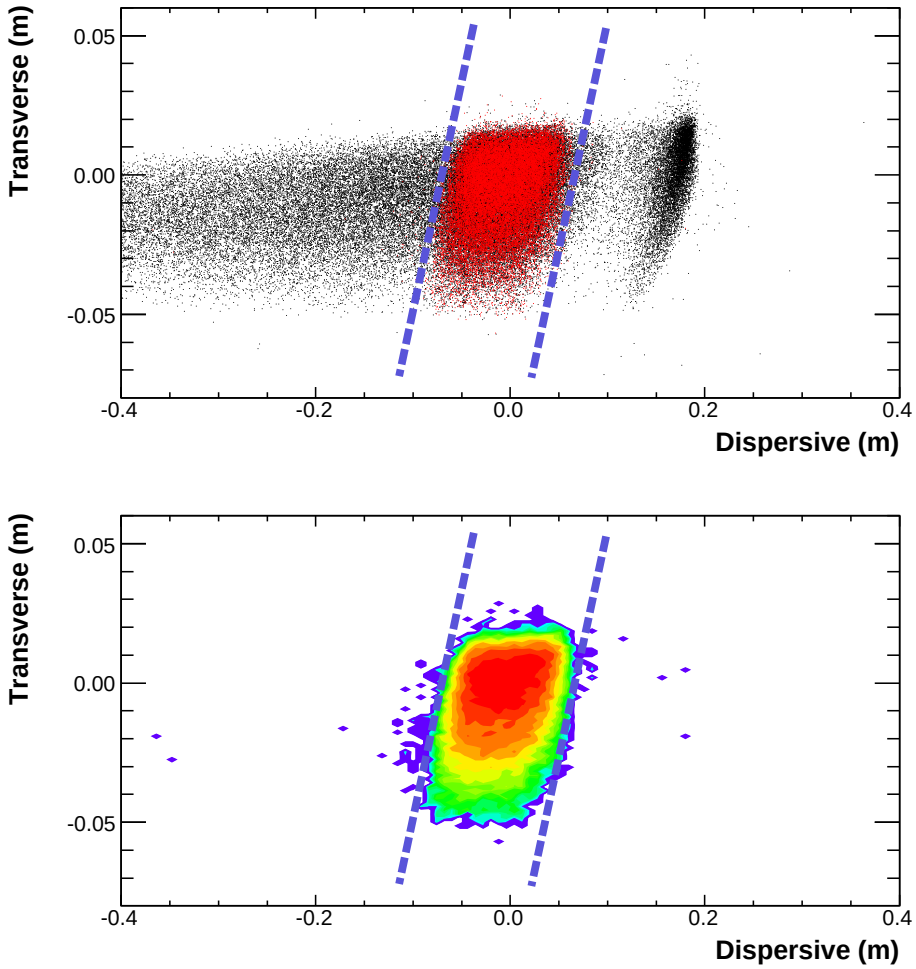

FIG. 3.16: Dispersive and Transverse vs. Dispersive distribution in the focal plane of the Left Spectrometer when its central momentum is deliberately set 2.8% higher than the production momentum setting. Top plot shows all triggers in black, HAPPEx detector triggers in red. Bottom logarithmic contour plot contains only HAPPEx detector triggers. Dashed lines, in both plots, show the estimated angle of the detector edges.

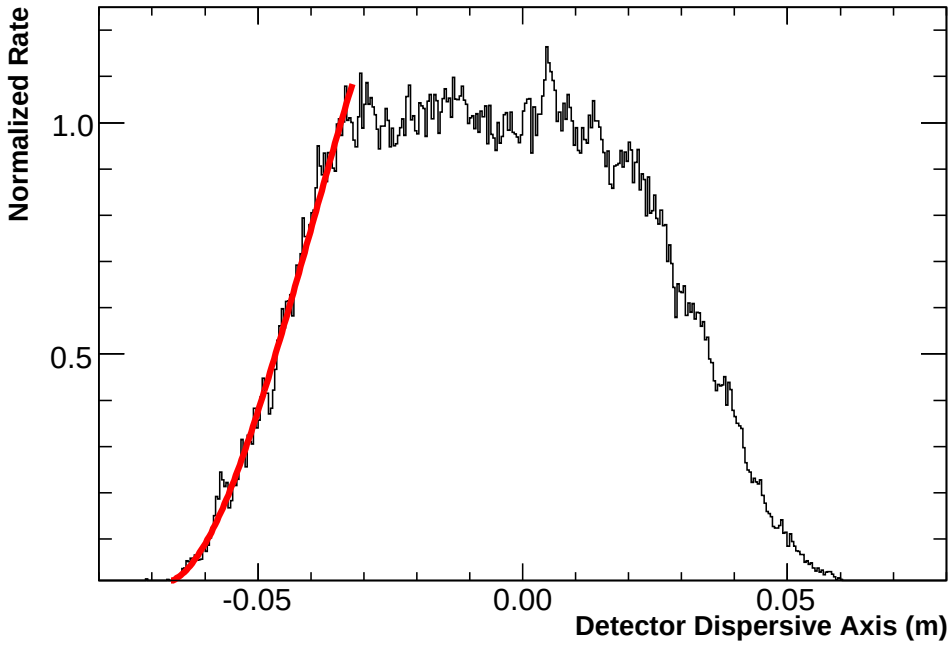

FIG. 3.17: One-dimensional profile of the dispersive axis of the HAPPEx detector, when the focal plane is illuminated with quasielastically scattered electrons.

Translation of 0% momentum setting to −2% momentum setting

As shown in Figure 2.17, the HAPPEx detector was installed in the space between the VDCs and the S2 scintillator plane, intersecting the nominal central ray in the focal plane. Because the HAPPEx detector was a total absorption detector it effectively casted a shadow of itself on S2, blocking the event rate that S2 would have normally observed in its center. Detection efficiencies were considerably different between these two detectors, creating a trigger bias when attempting to view the event distribution in the entire focal plane.

To determine an unbiased estimate of the helium elastic and quasielastic distribution on the HAPPEx detector, a counting mode measurement was made with the HRS momentum deliberately set about −2%, placing the distribution cleanly off of the HAPPEx detector, and fully on the S2 plane. The translation of the low momentum detector edge to this set-point was determined by using the measured

correlation between the fractional momentum and the dispersive detector axis.

Quasielastic high momentum falloff model

The distribution of scattered events in the detector dispersive axis using the ^{4}He target is shown in Figure 3.18. To determine the amount of quasielastic events that seep into the left edge of the detector, a model of the quasielastic falloff was assumed. The high momentum distribution was assumed fall off fairly linearly, because the quasielastic process has a single definite threshold. When this distribution is modeled with a line, the fraction that arrives within the detector's acceptance should be considered as an upper limit to the quasielastic background because there must be contribution to this rate from the elastic radiative tail.

The linear model is folded together with the detector resolution (determined using a Gaussian fit to determine the width of the super-elastic side), along with the HAPPEx detector acceptance model. This model is compared to small offsets in the detector edge location, in order to obtain an estimate for the systematic error. This model is shown in Figure 3.19. Using this prescription, the contamination fraction was determined to be $(2.0 \pm 1.0)\%$ and $(1.0 \pm 0.5)\%$ for the right and left arms, respectively. This results in a Q^2-weighted background fraction from this source of $(1.6 \pm 0.8)\%$.

Asymmetry

The parity-violating asymmetry from ^{4}He quasielastic scattering was evaluated using the same model used for Aluminum quasielastic scattering [17]. This asymmetry was calculated to be -1.6 ppm with a 50% error assumed.

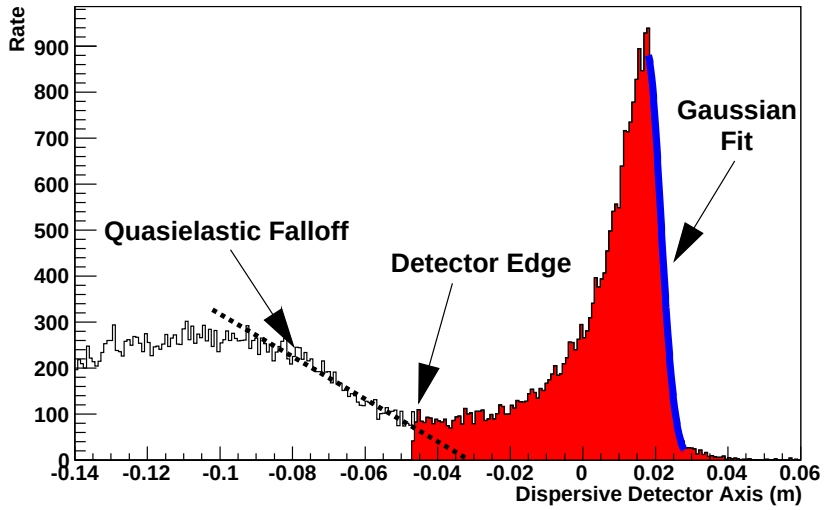

FIG. 3.18: Helium distribution in the detector dispersive axis, with the HRS momentum deliberately set low. The (red) filled region indicates the amount that falls within the detector. Dash line shows the quasielastic falloff hypothesis, solid line is a Gaussian fit to the "Super"-elastic side to determine the resolution in this axis.

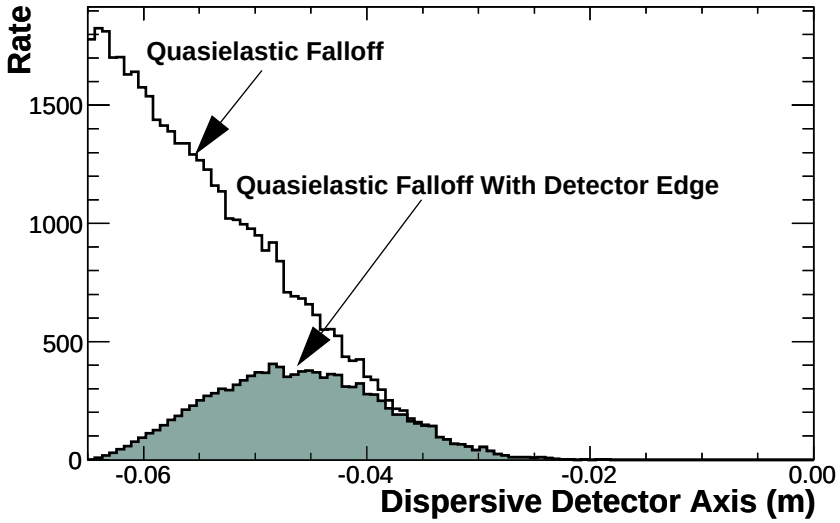

FIG. 3.19: Plot of the quasielastic falloff model (unfilled) and falloff model including the detector edge model (filled).

Lesson Learned

The presence of a trigger bias between the HAPPEx detector and the S2 plane created difficulty in the determination of the quasielastic background, as well as in the alignment of the elastic peak on to the HAPPEx detector during the calibration of the experiment. Increased difficulty in an experimental method is typically associated with increased systematic error in the measurement. With this in mind, a new detector was constructed for the 2005 dataset which provided an un-biased trigger over the entire focal plane. This new detector was referred to as the HAPPEx S0 detector.

The HAPPEx S0 detector (discussed in Appendix D) provided a means for clearly identifying the deviation of inelastic events from the expected elastic kinematics and lead to a better alignment of the elastic peak, as well as a much better determination (smaller systematic error [58]) of the quasielastic background into the HAPPEx detector .

3.4.3 Rescattering in the Spectrometer

Another type of background comes from inelastic scattering of the beam electrons from the target walls or ^{4}He nuclei, then rescattering inside of the spectrometer. The main portion of this background appears as low-energy charged or neutral particles that end up contributing to the integrated signal in the HAPPEx detector. To determine the extent of this background, a rescattering model was developed that assumes that the background is given by

$$f_{\rm rs} = \int_{E_{\rm min}}^{E_{\rm max}} dE\ P_{\rm rs}(E)\ R(E), \tag{3.19}$$

where the probability of rescatter ($P_{\rm rs}$) in the spectrometer is weighted by the Energy deposited ($E_{\rm dep}$) into the detector, normalized to the energy deposited by elastically

scattered electrons (E_0):

$$P_{\rm rs}(E) = (\text{rescatter probability}) \times \left(\frac{E_{\rm dep}}{E_0}\right), \tag{3.20}$$

and $R(E)$ is the ratio of the inelastic to the elastic cross section:

$$R(E) = \frac{\left(\frac{d\sigma}{d\Omega dE}\right)_{\rm inelastic}}{\left(\frac{d\sigma}{d\Omega}\right)_{\rm elastic}}. \tag{3.21}$$

The limits of Equation 3.19 go from the inelastic threshold ($E_{\rm min}$) to the estimated maximum inelastically-scattered electron energy that could contribute ($E_{\rm max}$).

Measurement of $P_{\rm rs}$ was done by incrementally increasing the dipole field in order to force the elastic trajectories to follow the path of the inelastic trajectories. This procedure was done utilizing the "Integrating Mode" DAQ because it automatically has the proper energy weighting, as required in Equation 3.20. Due to time constraints, this scan was performed using the Hydrogen target and HAPPEx-Hydrogen detector. This detector is twice as long as the ^{4}He detector (as described in Section 2.5.3) and spans a larger region of the spectrometer focal plane. The inelastic cross section was inferred from a model of the measured quasielastic distribution and an estimated Δ resonance distribution.

The resulting background fraction attributed to rescattering in the spectrometer was found to be 0.6%, where a conservative systematic error of 0.6% was made to account for the uncertainty in the model of $R(E)$ and probable over-estimate of the measured $P_{\rm rs}$. This fraction is dominated by ^{4}He quasielastic with a very small contribution from the Δ resonance ($\sim 10^{-4}$), thus the asymmetry of this background is assumed to be the same as for the non-rescatter quasielastic asymmetry (-1.6 ± 0.8 ppm).

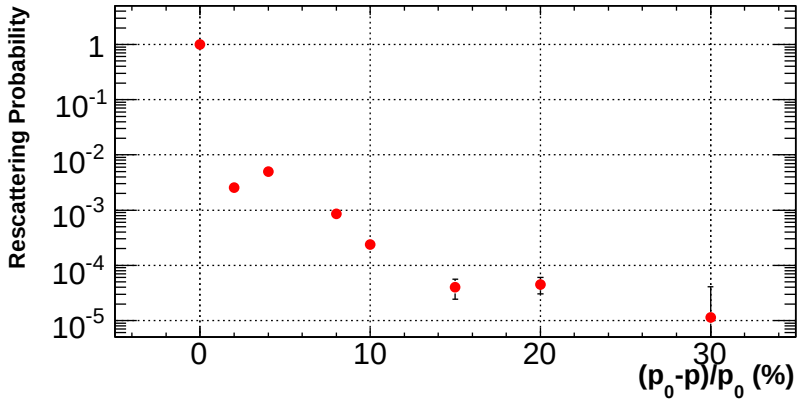

FIG. 3.20: Rescattering Probability as a function of the percent change in momentum of the spectrometer. Data shown was acquired from a hydrogen target using the HAPPEx-Hydrogen detector.

3.5 Linearity

Integrated signals from the beam monitoring devices and HAPPEx detectors are, ideally, proportional to the rates observed by those devices. In reality, any non-linearity in the device causes the measured signal to behave in a quadratic (or higher order) model:

$$S_{\text{meas}}(R) = \Delta P + \alpha R + \beta R^2, \tag{3.22}$$

where ΔP is the error in the subtracted ADC pedestal, R is actual rate, α is a linear coefficient, and β is the first non-linear coefficient. The measured asymmetry of this signal between two adjacent helicity windows is then

$$A(R) \simeq A_{\text{true}} \left(1 + \frac{\beta}{\alpha} R - \frac{P}{\alpha R}\right), \tag{3.23}$$

assuming that the linear term of Equation 3.22 is much larger than that of the other terms. The raw detector asymmetry A_{raw} is obtained from their signals normalized to the beam current, which is approximately given by:

$$A_{\text{raw}} \simeq A_{\text{DET}} - A_{\text{BCM}}, \tag{3.24}$$

where A_{DET} is the measured detector asymmetry, and A_{BCM} is the measured asymmetry from the beam current monitor (BCM).

Here's the main conclusions from those two equations:

- The Pedestals of the device must be accurately determined.
- β/α must be maintained below the statistical error of the measurement. The goal of this experiment was $\beta/\alpha < 2\%$.
- The systematic error scales with the larger of the two asymmetries ($A_{\rm DET}$ and $A_{\rm BCM}$). Since $A_{\rm DET}$ is essentially fixed by kinematics, $A_{\rm BCM}$ must be minimized. This was done by Charge Asymmetry Feedback.

For the detectors, the non-linearity of the photo-multiplier tubes was studied in detail [59, 60] and was found to be less than 1%. Detector pedestals were also easily determined by measuring the ADC signal during times when the beam is off. The same was achieved for the Unser monitor. Beam current monitor pedestals were calibrated by fitting their ADC signal versus that of the Unser monitor and extrapolating down to zero current.

BCM linearity was then determined by observing the difference in asymmetries between the up- and down-stream current monitors (described in Section 2.4.1)

$$\text{Double Difference} = A_{\rm BCM\_up} - A_{\rm BCM\_down}. \tag{3.25}$$

This so-called "double-difference", provided a measure of the β/α term from these monitors, and resulted in an upper limit to the systematic error from BCM linearity of 1%. Normalized detector linearity was then evaluated by fitting the normalized detector asymmetry versus the beam intensity asymmetry (Figure 3.21), with a deviation from a slope of 0 being an indication of non-linearity (the ϵF term of Equation 2.4). The systematic error on linearity was assumed to be the magnitude of this measured slope (0.6%).

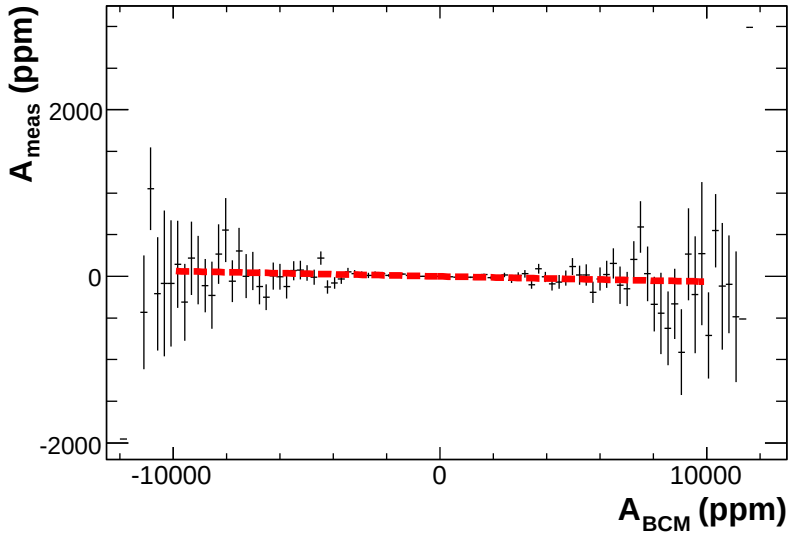

FIG. 3.21: Measured normalized asymmetry from the right arm HAPPEx detector versus the beam intensity asymmetry measured from the BCM. Dashed line is a fit to the data

3.6 Effective Kinematics

The finite acceptance of the spectrometer, combined with radiative energy losses and multiple scattering in the target cell, convolutes the measured asymmetry over a range of Q^2. To represent the measured value of the asymmetry at a single value of Q^2, this effect must be taken into account. To find the effective kinematics factor K needed to correct the measured asymmetry, a Monte Carlo simulation was used.

The event generator of the Monte Carlo, named "gener_cone" [61], is illustrated in Figure 3.22 follows the following algorithm:

- A pair of coordinates, transverse to the beam direction, is randomly selected according to a specified raster distribution.
- A coordinate, along the long axis of the target, is randomly selected between the target endcaps. Together with the coordinates from (1), this serves as the location of the interaction vertex.
- Polar (θ) and azimuthal (ϕ) angles are randomly generated using uniform

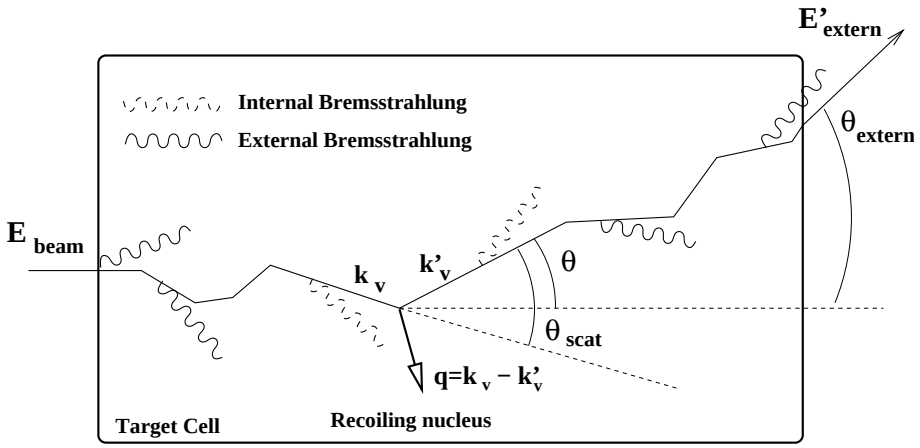

FIG. 3.22: Sequence of event generation in the Monte Carlo simulation.

distributions in $\cos\theta$ and ϕ. Limits on the range of these angles are set using the geometry of the main acceptance-defining collimator of the spectrometer. The geometry of this collimator is made slightly larger, (~ 1 mm, in each direction) to account for effects from multiple scattering (described below).

- Multiple scattering is applied to these angles, before the interaction vertex, using the Gaussian approximation prescribed in Section 23.3 of Ref. [62].

- Radiative energy losses for the incident electron are calculated from the target endcaps and material. These losses include those from ionization (collisional), external photon radiation, and internal photon radiation.

- Calculation of the vertex kinematics of the elastically scattered electron along the direction of (θ, ϕ): the physical scattering angle $\theta_{\rm scat}$, the cross section $d\sigma/d\Omega$ of the target nuclei, the corresponding Q^2 and parity-violating asymmetry $A_{\rm PV}$.

- Calculation of radiative energy losses (similar to calculated energy losses before the vertex), for the scattered electron exiting the target cell.

- Application of multiple scattering to the angles generated after the interaction

vertex. This forms the observed (experimental) scattering angle (θ_{extern}).

- Acceptance or rejection of the event generated, by determining if the path of the scattered electron falls within the defined geometry of the acceptance of the spectrometer.

- Propagation of the scattered electron from the target to the focal plane using an optics model of the spectrometer.

- Determination if the optically-transported electron intersects the simulated HAPPEx detector in the focal plane. The geometry of the detector is fixed, but the location and orientation can be varied.

A comparison of the simulation with data taken in counting mode for various observables is shown in Figure 3.23. It shows that the simulation can accurately generate events that are qualitatively the same as in the experimental setup.

The effective kinematics factor K is calculated from:

$$K = \frac{A_{PV}\left(\langle Q^2_{det}\rangle\right)}{\langle A_{PV}(Q^2_{vx})\rangle} \tag{3.26}$$

where the numerator is the parity-violating asymmetry calculated at the mean Q^2 as observed by events that hit the HAPPEx detector, and the denominator is the average parity-violating asymmetry for any Q^2 in the acceptance, evaluated at the interaction vertex. The resulting value is $K = 1.000 \pm 0.001$, where the sensitivity of this factor due to small changes in collimator position, detector orientation, and septum magnet field setting were found to be negligible. This value for K is the expected results for ^{4}He because A_{PV} is linear in Q^2. Any deviation from 1 would be an indication that radiative energy losses and multiple scattering are important. This calculation provides a good cross-check on this procedure that was originally developed for calculation of K for a LH_2 target, where A_{PV} is a function of Q^2 and θ and the calculated effective kinematics factor was $K = 0.979 \pm 0.002$.

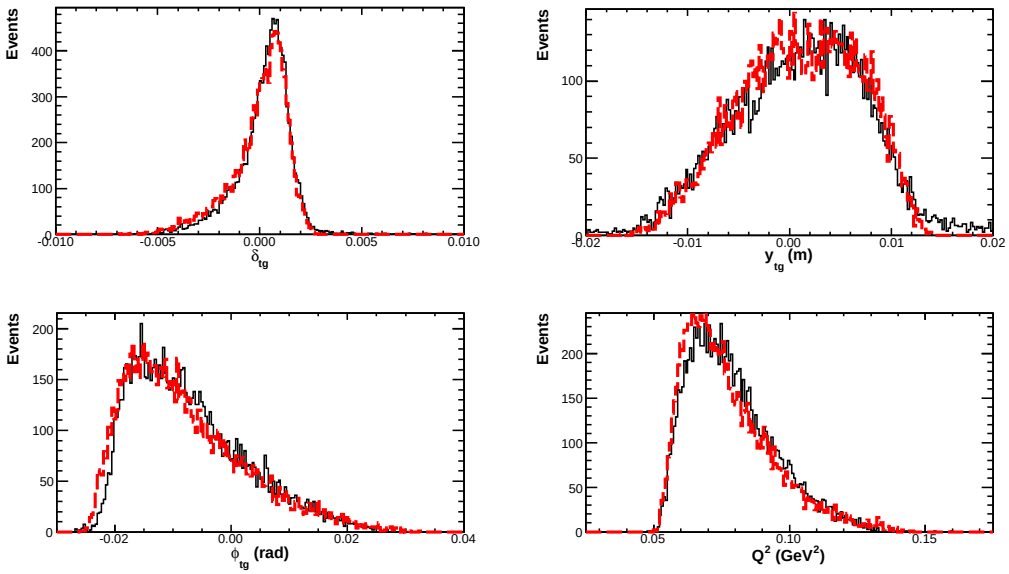

FIG. 3.23: Comparison of reconstructed target parameters ($\delta, y_{tg}, \phi_{tg}, Q^2$) obtained from a Counting Mode measurement (black, solid) and those simulated with the Monte Carlo simulation (red, dashed).

A more detailed analysis was performed for the 2005 dataset, where the results showed similar insensitivity to simulation parameters (as shown in Figure 3.24).

3.7 Final Experimental Asymmetry

The physics asymmetry A_{phys} is formed from A_{corr} by correcting for beam polarization P_b, background fractions f_i and their corresponding asymmetries A_i, linearity L, and a term to account for effective kinematics K as follows:

$$A_{\text{phys}} = \frac{KL}{P_b} \frac{A_{\text{corr}} - P_b \sum_i A_i f_i}{1 - \sum_i f_i}. \tag{3.27}$$

Table 3.8 presents a summary of the various factors in Equation 3.27. The statistical error of A_{phys} is entirely determined from that of A_{corr}, with the proper weighting from the values K,L, and P_b. The systematic error is evaluated by adding the associated systematic errors for each term (weighted by their corresponding partials) in quadrature.

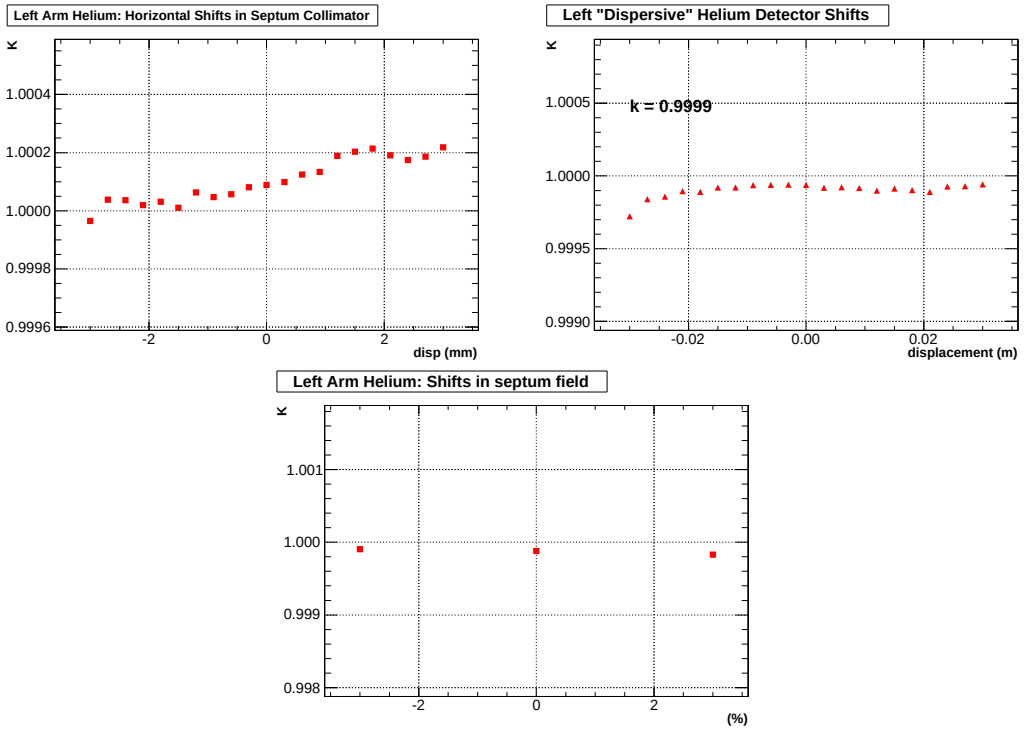

FIG. 3.24: Sensitivity of effective kinematics factor K to simulation parameters.

After all corrections, the parity-violating asymmetry from ^{4}He is found to be

$$A_{\text{phys}} = 6.72 \pm 0.84\ (\text{stat}) \pm 0.21\ (\text{syst})\ \text{ppm}, \tag{3.28}$$

representing a 12.9% measurement of this parity-violating asymmetry. This result represents the *first* measurement of a parity-violating asymmetry from ^{4}He. Individual contributions to the systematic error are detailed in Table 3.9.

Term	Description	Value	Error	Units
f_1	Al-QE fraction	0.0066	0.0010	
A_1	Al-QE asymmetry	-1.7	-1.7	ppm
f_2	He-QE fraction	0.0158	0.0079	
A_2	He-QE asymmetry	-1.6	-0.8	ppm
f_3	He-QE rescatter fraction	0.0060	0.0060	
A_3	He-QE rescatter asymmetry	-1.6	-1.6	ppm
P_b	Beam Polarization	0.869	0.017	
L	Linearity (BCM)	1.	0.010	
L	Linearity (Det/BCM)	1.	0.006	
K	Effective Kinematics	1.	0.001	

TABLE 3.8: Corrections to $A_{\rm corr}$ and systematic errors.

Description	Error Contribution (ppb)	
	Individual	Total
False Asymmetry		103
Energy	50	
Position/Angle	70	
Q^2		66
Backgrounds		88
Al-QE	14	
He-QE	69	
He-QE rescatter	52	
Delta rescatter	6	
Beam Polarization		115
Linearity		78
BCM	67	
Det/BCM	40	
Finite Acceptance		7
Total Systematic Error		205

TABLE 3.9: Systematic error contributions to the systematic error of $A_{\rm phys}$.

CHAPTER 4

Results and Discussion

We conclude this paper by extracting the strange electric form factor (G_E^s) from the obtained experimental asymmetry. This result will then be put into context with the results from other experiments examining the same type of physics. A global fit of the data obtained at and near $Q^2 = 0.1$ (GeV/c)^2 will be shown, then compared to recent theoretical predictions. Finally, a final discussion of implications of these results on the effect on future experiments will be presented.

4.1 Extraction of Strange Electric Form Factor

The parity violating asymmetry, including the radiative corrections to the coupling constants in the Electroweak Lagrangian, is given by (from Equations 1.68 and 1.69)

$$A_{\mathrm{PV}} = \frac{G_F Q^2}{4\pi\alpha\sqrt{2}} \left[4\rho'\kappa' \sin^2\theta_W + 6\left(\lambda_{1u} + \lambda_{1d}\right) + \left[\rho' + 2(\lambda_{1u} + \lambda_{1d} + \lambda_{1s})\right] \frac{2G_E^s}{G_E^{\gamma p} + G_E^{\gamma n}} \right] \tag{4.1}$$

where the Isospin mixing of nuclear states term, $\Gamma(Q^2)$, has been neglected and will only be considered as a systematic error. The values for the constants in Equation 4.1

are shown in Table 4.1. At the average kinematics for this measurement, this reduces Equation 4.1 to:

$$A_{\mathrm{PV}} = (7.483 + 20.01 G_E^s) \text{ ppm} \tag{4.2}$$

where the values for the electromagnetic form factors ($G_E^{\gamma p}$ and $G_E^{\gamma n}$) were obtained from a phenomological fit to the existing world data [14]. Comparing Equation 4.2 to Equation 3.28, the value of the strange electric form factor is extracted:

$$G_E^s = -0.038 \pm 0.042 \text{ (stat)} \pm 0.010 \text{ (syst)} \tag{4.3}$$

which is consistent with zero.

Term	Value
$\sin^2\theta_W$	0.23117
ρ'	0.9881
κ'	1.0027
λ_{1u}	-1.85×10^{-5}
λ_{1d}	3.70×10^{-5}
λ_{1s}	0.0

TABLE 4.1: Values for Coupling contants in the Electroweak Lagrangian as they are expressed in the Standard Model. These are obtained from Table 10.2 of [22].

4.2 World Data

Several other experiments have been dedicated to the measurement of the vector strange form factors of the nucleon. Each uses significantly different techniques for measuring the parity-violating asymmetry, and at the same time produces remarkably consistent results.

4.2.1 HAPPEx

The first HAPPEx measurements [23] were performed at Jefferson Lab's Hall A in 1998-1999, using a nearly identical experimental setup as described in this

paper. Scattered electrons from a liquid hydrogen target were detected at an average scattering angle of 12.5°. With an electron beam energy of ~ 3.3 GeV, the measurement of the parity-violating asymmetry was made at $Q^2 = 0.477$ (GeV/c)^2. The detectors, placed in the focal plane of the High Resolution Spectrometers, were composed of alternating layers of acrylic and lead, oriented to direct Cherenkov light into a single photo-multiplier tube.

The largest systematic error from these measurements arose from the uncertainties in the beam polarization as measured by the Hall A Møller and Compton polarimeters. Backgrounds were highly suppressed by the dispersion and focussing properties of the spectrometer. The resulting strange form factor linear combination was extracted

$$Q^2 = 0.477 \text{ (GeV/c)}^2 : \quad G_E^s + \eta G_M^s = 0.014 \pm 0.020 \text{ (tot)} \pm 0.010 \text{ (FF)}, \tag{4.4}$$

where the first error is the total experimental error (systematic and statistical added in quadrature) and the second error due to uncertainties in the electromagnetic form factors. The common factor η, used to express this linear combination is defined as

$$\eta = \frac{\tau G^{\gamma p}}{\epsilon G^{\gamma p}}. \tag{4.5}$$

The "sibling" experiment to HAPPEx-^{4}He, was the measurement of the parity-violating asymmetry from liquid hydrogen at nearly the same $Q^2 = 0.099$ (GeV/c)^2 which took data in 2004 directly after the HAPPEx-^{4}He measurement. Details of the apparatus and analysis are found in Ref. [63]. The resulting strange form factor combination from this measurement yielded

$$Q^2 = 0.099 \text{ (GeV/c)}^2 : \quad G_E^s + \eta G_M^s = 0.030 \pm 0.026 \text{ (tot)} \pm 0.012 \text{ (FF)}. \tag{4.6}$$

Both of these measurements, from hydrogen and helium, obtained more data in 2005 [58]. Resulting in

$$Q^2 = 0.077 \text{ (GeV/c)}^2 : \quad G_E^s = 0.002 \pm 0.014 \text{ (stat)} \pm 0.007 \text{ (syst)}, \tag{4.7}$$

for the helium measurement, and for the hydrogen measurement

$$Q^2 = 0.109 \text{ (GeV/c)}^2 : \quad G_E^s + \eta G_M^s = 0.007 \pm 0.012 \text{ (tot)} \pm 0.005 \text{ (FF)}. \tag{4.8}$$

4.2.2 SAMPLE

The SAMPLE experiment was performed at the MIT-Bates accelerator facility. A schematic of the SAMPLE apparatus is shown in Figure 4.1. Scattered electrons from a 40 cm liquid hydrogen target at 138° to 160° generated Cherenkov light in an air medium. This light was focused by 10 ellipsoidal mirrors into 10 8-inch photo-multiplier tubes. The PMTs were encased in lead cylinders to minimize background from electromagnetic radiation. Extra borated polyethylene shielding, for the deuterium measurements, was added between the target and PMTs to reduce background from neutrons from the target.

Detector signals were integrated over each beam pulse (25 μs) utilizing current-to-voltage amplifiers into a 16-bit ADC. Backgrounds, from non-Cherenkov light, was measured regularly during the course of the experiments in dedicated runs using PMT shutters. A detailed description of the analysis is found in Ref. [64]. From the kinematics from these measurements, the asymmetry has a stronger sensitivity to G_M^s and $G_A^{e\,(T=1)}$. The resulting proton measurement yielded:

$$G_M^s(Q^2 = 0.1) = 0.37 \pm 0.20 \text{ (stat)} \pm 0.26 \text{ (syst)} \pm 0.07 \text{ (FF)} \tag{4.9}$$

4.2.3 A4

Measurements of the forward angle parity violating asymmetry from the proton at $Q^2 = 0.108, 0.230$ (GeV/c)^2 were also performed using the A4 apparatus at the Mainzer Mikrotron accelerator (MAMI) [49, 48]. The accelerator provided a 20 μA, 570.4, 854.3 MeV, $\sim$ 80% polarized beam. Scattered electrons at $30 - 40°$ from

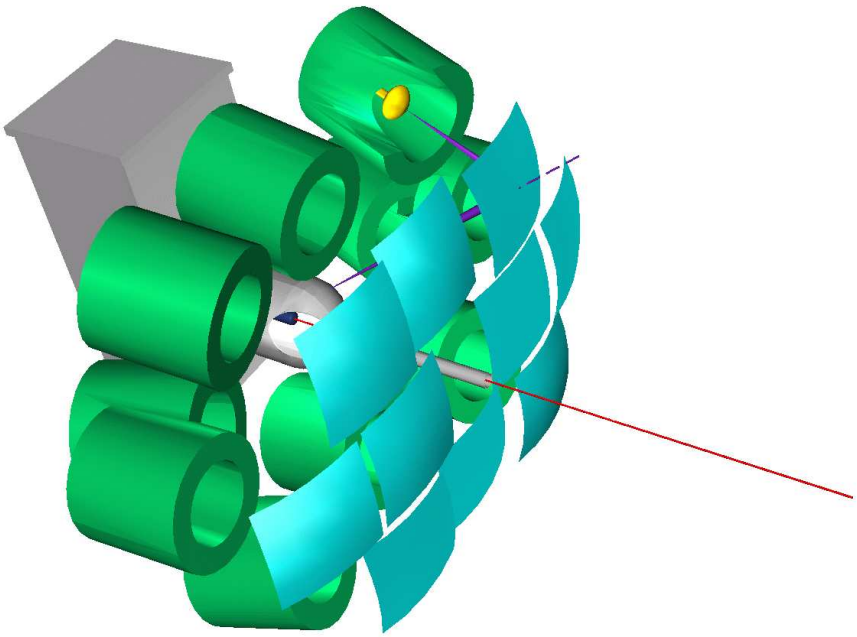

FIG. 4.1: Schematic of the SAMPLE Spectrometer.

a 10 cm hydrogen target were detected by a fast counting lead fluoride (PbF_2) calormeter. The energy resolution ($3.9\%/\sqrt{E}$) of the calorimeter along with the readout electronics, allowed for isolation of the elastic events from the inelastic spectra without the need of a magnetic spectrometer.

Corrections to the detected counting asymmetry due to beam false asymmetries were done using a regression analysis (similar to the approach described in Appendix B). The largest corrections to the physics asymmetry were from beam charge asymmetry and polarization, where the largest source of systematic error were from beam polarization measurement and interpolation and target density luminosity. The final results, from the two measurements was:

$$Q^2 = 0.108 \text{ (GeV/c)}^2 : \quad G_E^s + 0.106 G_M^s = 0.071 \pm 0.036, \tag{4.10}$$

$$Q^2 = 0.230 \text{ (GeV/c)}^2 : \quad G_E^s + 0.225 G_M^s = 0.039 \pm 0.034. \tag{4.11}$$

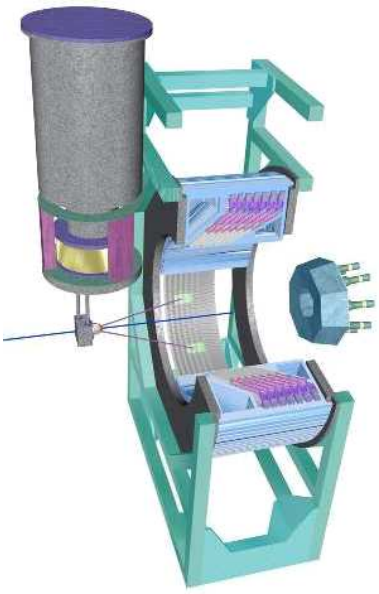

FIG. 4.2: Schematic of the A4 Spectrometer.

Measurement of the parity violating asymmetry for backward scattered electrons ($\theta_{\text{lab}} \sim 145°$) has recently been made, providing the extraction of G_M^s and G_A at $Q^2 = 0.23$ (GeV/c)^2. Results from these measurements should be quite intriguing because the precision is expected to be much higher than the SAMPLE measurements.

4.2.4 G^0

The G^0 experiment was run in Hall C at Jefferson Lab. It utilized 40 μA polarized beam at an energy of 3.03 GeV. It features a large toroidal magnet, designed to bend forward angle recoil protons into eight sets of scintillator detectors (as depicted in Figure 4.3). This allowed for a simultaneous measurement of a wide range of $Q^2 = [0.12, 1.0]$ (GeV/c)^2 of the linear combination of vector strange form factors ($G_E^s + \eta G_M^s$). Each octant of the spectrometer contained 16 scintillator detectors, oriented such that the first 13 are independent bins of Q^2, where the 14$^{\text{th}}$ and 15$^{\text{th}}$ covered larger ranges of the upper bound of the Q^2 acceptance. The final

detector (16), allowed for measurement of background.

Elastic protons were separated from inelastic background (inelastic protons and pions) by constructing a time-of-flight spectrum formed by the difference in time between the beam arrival signal and the detected particle signal. The TOF difference between the elastic proton peak and pion peak allowed for determination of Q^2 through incorporation of the known spectrometer field integral.

Individual proton events were counted. Thus the detected asymmetry was formed from the fractional difference between the counting rate between the two electron helicity states. This rates were corrected for helicity correlated beam systematics using linear regression (as in Appendix B) as well as DAQ dead time (measured to be about $10\% - 15\%$).

The results of the G^0 forward angle measurement [65] comprises a majority of the data points shown in Figure 4.5. The largest systematic contribution to the error bars shown is from inelastic background and inadvertent beam (leakage beam) meant for the other experimental halls.

A backward angle measurement, being performed at the time of this paper, of elastic scattering from the proton and deuteron targets aims to extract the linear combination of G_M^s and G_A at $Q^2 = 0.23, 0.6$ (GeV/c)^2.

4.2.5 Summary of Strange Form Factor Measurements

Figure 4.4 presents the world data for the measurement of G_E^s and G_M^s at $Q^2 \sim 0.1$ (GeV/c)^2. Of particular interest is the measurements performed by the HAPPEx Collaboration on Hydrogen and Helium targets from 2005. Constraints from these experiments dominate the overall size of the 95% confidence level ellipse that is generated using the data from all of the experiments that provided measurements near $Q^2 = 0.1$ (GeV/c)^2. From the ellipse, the vector strange form factors

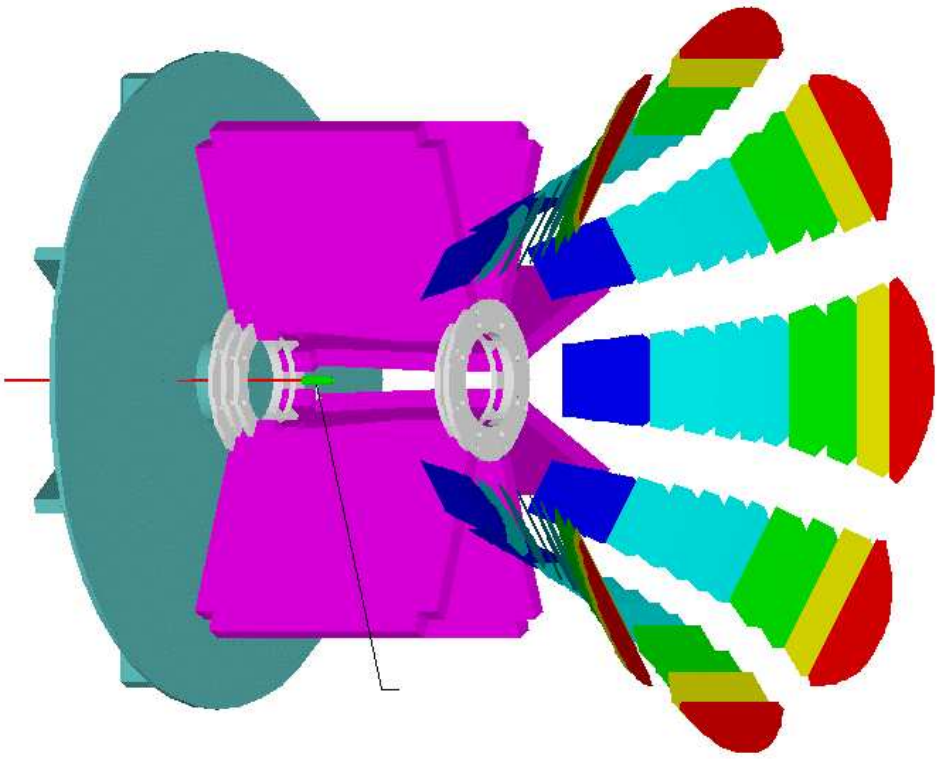

FIG. 4.3: Schematic of the G^0 Spectrometer.

have been extracted:

$$G_E^s = -0.006 \pm 0.016 \tag{4.12a}$$

$$G_M^s = 0.28 \pm 0.20. \tag{4.12b}$$

The Q^2 evolution of the linear combination $G_E^s + \eta G_M^s$ is shown in Figure 4.5. Only forward angle measurements performed on a Hydrogen target are shown, due to the possible contributions from the axial form factor G_A that has more sensitivity in backward angle and deuterium measurements. The inclusion of the HAPPEx-H (2005) data severly constrains the strange form factor combination at low Q^2. The "bump" at $Q^2 \sim 0.1$ (GeV/c)^2 and possible cancellation effect at $Q^2 \sim 0.2$ (GeV/c)^2 that generated some excitement, appears to now be ruled out. It remains to be seen if there remains to be some effect due to some enhancement from the A4 measurement

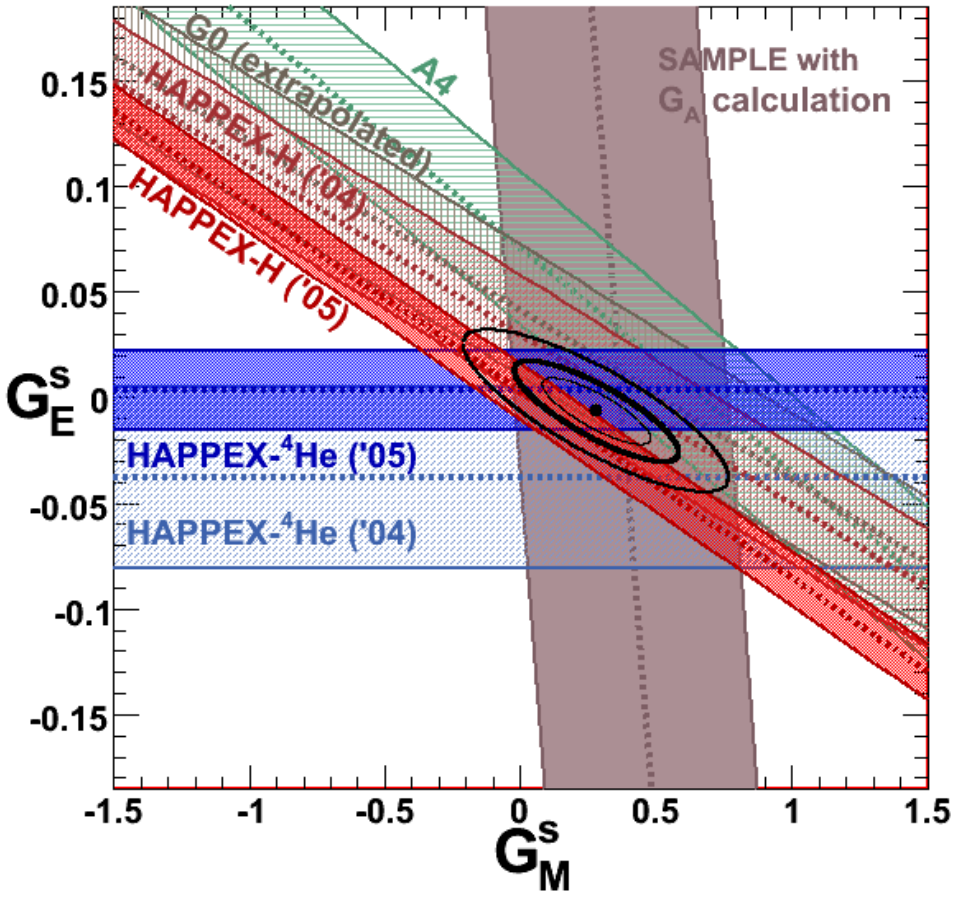

FIG. 4.4: World data of G_E^s versus G_M^s at $Q^2 = 0.1$ (GeV/c)^2. All experimental 1-σ bands are the quadrature sum of statistical and systematic errors. Results from the analysis presented in this paper are indicated by the label "HAPPEX-^{4}He ('04)". Inner and outer ellipses show 95% and 68% confidence level constraints.

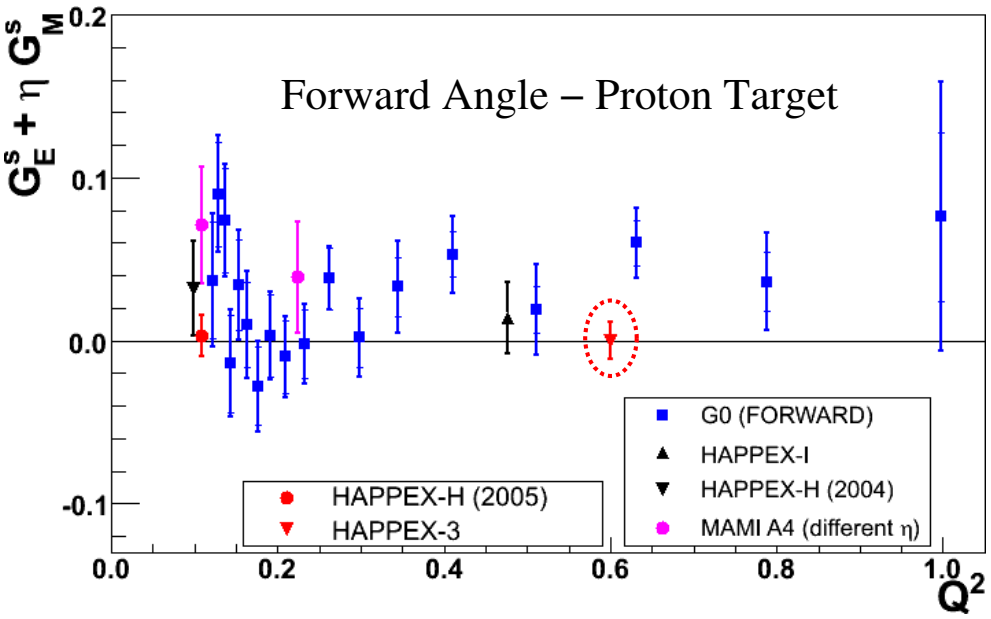

FIG. 4.5: World data of $G_E^s + \eta G_M^s$ at forward angle on proton targets as a function of Q^2.

from G_A (performed at a larger scattering angle).

Ongoing and future experiments (G^0 and A4 backward angle measurments, and HAPPEx-III) will further constrain measurements at higher Q^2. Provided the measurements at low Q^2, and the the predicted behavior of these strange form factors as a function of Q^2 (Equation 1.52), these measurements still have the possibility of measuring a strange contribution to the nucleon form factors at the $2-3\sigma$ level.

4.3 Theoretical Implications

To illustrate the impact of the HAPPEx measurements on knowledge of the strange form factors at $Q^2 \sim 0.1$ (GeV/c)^2, the 2004 and 2005 measurements are combined and shown in Figure 4.6. A small interpolation of each measurement to a common Q^2 was made assuming that $G_E^s \propto Q^2$ and G_M^s remained constant. The 95% and 68% confidence level ellipses provide a means for comparison to theoretical

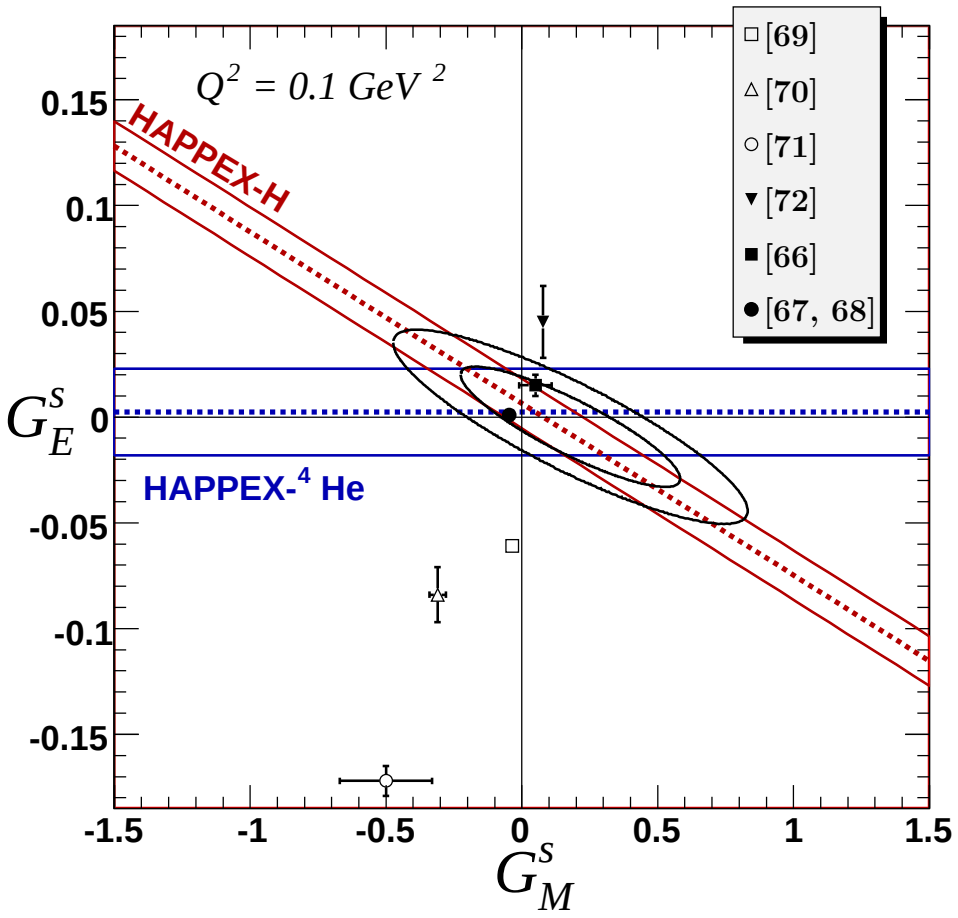

FIG. 4.6: Combined data from the 2004 and 2005 HAPPEx runs on hydrogen and helium for G_E^s versus G_M^s at $Q^2 = 0.1$ (GeV/c)^2. All experimental 1-σ bands are the quadrature sum of statistical and systematic errors. Inner and outer ellipses show 95% and 68% confidence level constraints.

expectations. From the 95% ellipse

$$\begin{aligned} G_E^s &= -0.005 \pm 0.019 \\ G_M^s &= 0.18 \pm 0.27. \end{aligned} \tag{4.13}$$

Also plotted in this figure are predictions from selected theoretical models. Table 4.3 summarizes these models. Those that predict little strange quark dynamics in the vector form factors are strongly favored (most notably the results from low-energy quenched lattice QCD simulations from Ref. [66, 67, 68]).

Source	G_E^s	G_M^s	Reference
Skyrme Model	-0.061	-0.036	[69]
Dispersion Relation	-0.084 ± 0.013	-0.310 ± 0.030	[70]
Dispersion Relation	-0.172 ± 0.007	-0.500 ± 0.170	[71]
Chiral Quark Soliton Model	$+0.045 \pm 0.017$	$+0.078 \pm 0.012$	[72]
Lattice	$+0.015 \pm 0.005$	$+0.050 \pm 0.060$	[66]
Lattice + Charge Symmetry	$+0.001 \pm 0.006$	-0.046 ± 0.019	[67, 68]

TABLE 4.2: Various theoretical predictions for strangeness in the nucleon.

4.4 Future Related Experiments

Jefferson Lab experiment E00-003, nick-named PREx, will measure the parity-violating asymmetry via scattering from ^{208}Pb [73]. The result will provide the measurement of the neutron radius of a heavy nucleus at 1% precision, and may have important implications for the understanding the structure of the crust of neutron stars [74]. The relative statistical precision on the asymmetry ($\sim$ 3%) means that Q^2 and beam polarization must be measured to about the 1% level, while the absolute precision of about 15 ppb means that false asymmetries must be minimized and understood well below this level.

Measurement of the weak charge of the proton by Jefferson Lab experiment E02-020 (Q_{weak}) [75], endeavors to constrain the running of $\sin^2\theta_W$ to 10σ of the Standard Model. This provides the result with signficant sensitivity to new types of physics, including additional gauge bosons, supersymmetry, and leptoquarks. The experiment is designed to detect elastically scattered electrons from the proton at $7 - 10^\circ$ at $Q^2 = 0.03$ (GeV/c)^2. Aside from the experimental challenges that mirror those of PREx, uncertainty in strange quark contributions to the vector form factors muddles the experimental interpret-ability. Constraints to these so-called "hadronic-background" contributions, made by the experiments mentioned in Section 4.2, have nearly settled this issue.

4.5 Conclusion

In this paper, we have reported on the extraction of the strange electric form factor G_E^s from the first measurement of the parity-violating asymmetry from the elastic scattering of longitudinally polarized electrons from ^{4}He. These constraints on the strange electric and magnetic form factors at low Q^2 have increased our knowledge and understanding of nucleon structure. A description of the experimental technique and apparatus, as well as the analysis of the data obtained from this measurement, has been provided to support the credibility of its result. Future ambitious parity-violation experiments not only benefit in the interpret-ability of their results from this measurement, but have the advantage of incorporating some of the techniques mentioned in this paper to minimize the sources of systematic errors that are important in these types of experiments.

APPENDIX A

2004 HAPPEX Collaboration

2004 HAPPEX Collaboration

X. Zheng
Argonne National Laboratory, Argonne, Illinois, 60439, USA

K. A. Aniol, D. J. Margaziotis
California State University, Los Angeles, Los Angeles, California 90032, USA

E. Burtin, D. Lhuillier, C. Munoz-Camacho, D. Neyret, A. Vacheret
CEA Saclay, DAPNIA/SPhN, F-91191 Gif-sur-Yvette, France

D. S. Armstrong, T. Averett, J. M. Finn, T. Holmstrom, A. Kelleher, B. Moffit, V. Sulkosky
College of William and Mary, Williamsburg, Virginia 23187, USA

R. Wilson
Harvard University, Cambridge, Massachusetts 02138, USA

F. Cusanno, S. Frullani, F. Garibaldi, G. M. Urciuoli
INFN, Sezione Sanità, 00161 Roma, Italy

R. Subedi
Kent State University, Kent, Ohio 44242, USA

A. Glamazdin, V. Gorbenko, R. Pomatsalyuk
Kharkov Institute of Physics and Technology, Kharkov 310108, Ukraine

M. Mazouz, E. Voutier
Laboratoire de Physique Subatomique et de Cosmologie, 38026 Grenoble, France

S. Kowalski, P. Monaghan, Y. Qiang, R. Suleiman
Massachusetts Institute of Technology, Cambridge, Massachusetts 02139, USA

D. Deepa, H. Ibrahim
Old Dominion University, Norfolk, Virginia 23508, USA

X. Jiang, K. McCormick
Rutgers, The State University of New Jersey, Piscataway, New Jersey 08855, USA

P. Decowski, D. Lambert
Smith College, Northampton, Massachusetts 01063, USA

H. Benaoum, R. Holmes, P. A. Souder
Syracuse University, Syracuse, New York 13244, USA

Seonho Choi, Z.-E. Meziani
Temple University, Philadelphia, Pennsylvania 19122, USA

Y.-C. Chao, J.-P. Chen, E. Chudakov, R. J. Feuerbach, R. Gilman, J. M. Grames, J. Hansknecht, D. W. Higinbotham, C. W. de Jager, J. LeRose, D. G. Meekins, R. Michaels, S. Nanda, M. Poelker, B. Reitz, J. Roche, A. Saha, B. Wojtsekhowski
Thomas Jefferson National Accelerator Facility, Newport News, Virginia 23606, USA

P. Y. Bertin, C. Ferdi
Université Blaise Pascal/CNRS-IN2P3, F-63177 Aubière, France

T. B. Humensky
University of Chicago, Chicago, Illinois 60637, USA

A. Kolarkar
University of Kentucky, Lexington, Kentucky 40506, USA

C. C. Chang
University of Maryland, College Park, Maryland 20742, USA

J. Cahoon, K. Fuoti, L. J. Kaufman, K. S. Kumar, P. LaViolette, K. D. Paschke
University of Massachusetts Amherst, Amherst, Massachusetts 01003, USA

G. D. Cates, B. Craver, N. Liyanage, V. Nelyubin, J. Singh, R. Snyder, W. A. Tobias, K. Wang
University of Virginia, Charlottesville, Virginia 22904, USA

APPENDIX B

Regression Analysis

Formalism

One method for removing helicity correlations from beam position, angle, and energy from the detected asymmetry involves using the "natural" motion of the beam. This method is referred to as the regression method, because the slope of each beam parameter is determined using a least-squares (or linear χ^2 minimization) algorithm. For a one parameter regression, the slope is calculated in the usual way:

$$b = \frac{\sum_i (y_i - < y >)(x_i - < x >)}{\sum_i (x_i - < x >)^2} \tag{B.1}$$

where y is the dependent variable, and x is the independent variable. The dependent variable, is now regressed by removing its above calculated sensitivity to x:

$$y_i^{reg} = y_i - bx_i \tag{B.2}$$

For a two or more parameter regression, an interation of this algorithm may be done, utilizing the regressed dependent variable in each step. For example, a three parameter regression:

$$\begin{aligned} y_i^{reg2} &= y_i^{reg} - b_1(x_1)_i \\ y_i^{reg3} &= y_i^{reg2} - b_2(x_2)_i \end{aligned}$$

This process must be repeated, at least twice, for each calculated slope if there exists correlations between each independent variable.

A non-iterative method that effectively diagonalizes the space spanned by the independent variables is referred to as the Matrix Inversion algorithm. Here, the deviation of the mean of the independent variable is expected to be linearly dependent on the deviation from the means of the dependent variables:

$$y = \sum_{k=1}^{m} B_k x_k \tag{B.3}$$

Where m is the total number of independent variables. Assuming Gaussian statistics, the probability of measuring y_i given B_k:

$$P_{B_k} = \prod_i \left(\frac{1}{\sqrt{2\pi}\sigma_i} \right) \exp\left(-\frac{1}{2} \sum_i \frac{y_i - \sum_k^m B_k (x_k)_i}{\sigma_i^2} \right) \tag{B.4}$$

where $(x_k)_i$ is the i^{th} measurement of the k^{th} independent variable. This provides access to the χ^2:

$$\chi^2 = \sum_i \left(\frac{y_i - \sum_k^m B_k (x_k)_i}{\sigma_i^2} \right)^2 \tag{B.5}$$

which is then minimized with respect to each coefficient B_k:

$$\frac{\partial \chi^2}{\partial B_k} = -2 \sum_i \left(\frac{(x_k)_i}{\sigma_i^2} [y_i - \sum_k^m B_k (x_k)_i] \right) = 0 \tag{B.6}$$

Assuming that the variance is the same, point to point, one arrives at the expression:

$$\sum_i y_i (x_l)_i = \sum_{k=1}^{m} B_k \sum_i (x_l)_i (x_k)_i \tag{B.7}$$

which is represented in matrix form:

$$\begin{aligned} \mathbf{Y} &= Y_l &&= \sum_i y_i (x_l)_i \\ \mathbf{X} &= X_{lk} &&= \sum_i (x_l)_i (x_k)_i \\ \mathbf{Y} &= \mathbf{BX} \end{aligned}$$

Inversion of $\mathbf{X}$ then provides a calculation of the regression coefficients:

$$\mathbf{B} = \mathbf{Y}\mathbf{X}^{-\mathbf{1}} \tag{B.8}$$

It can be shown that the error in these coefficients is related to the diagonal elements of the inverted $\mathbf{X}$:

$$\sigma_{B_k} = \frac{1}{\sigma}\sqrt{(X_{kk})^{-1}} \tag{B.9}$$

APPENDIX C

Synchronization Monitor

The upgrade of the original HAPPEx data acquisition [24] to a multi-crate system called for a means for measuring the synchronization of the integration gates between HAPPEx timing board in each crate. To provide this service, a synchronization monitor was constructed to send two complimentary and pseudo-random frequency signals to each crate. The resulting analysis of these signals provided information on the difference in length of each gate and variations in start time.

C.1 Setup

The main controlling signals of the synchronization monitor were the MPS signal from the polarized source and the digital-to-analog voltage converter (DAC) output of the timing board in the counting house. These signals were routed through various NIM modules, as outlined in Figure C.1. The MPS signal was sent to a gate generator, where the start of the gate was delayed sufficiently to keep it within the 300 μs "settle time". The end of the gate was adjusted such that it fell within the first half of the helicity window (Figure C.2). This signal (GATE) and its compliment ($\overline{\text{GATE}}$) were then routed to a logic module.

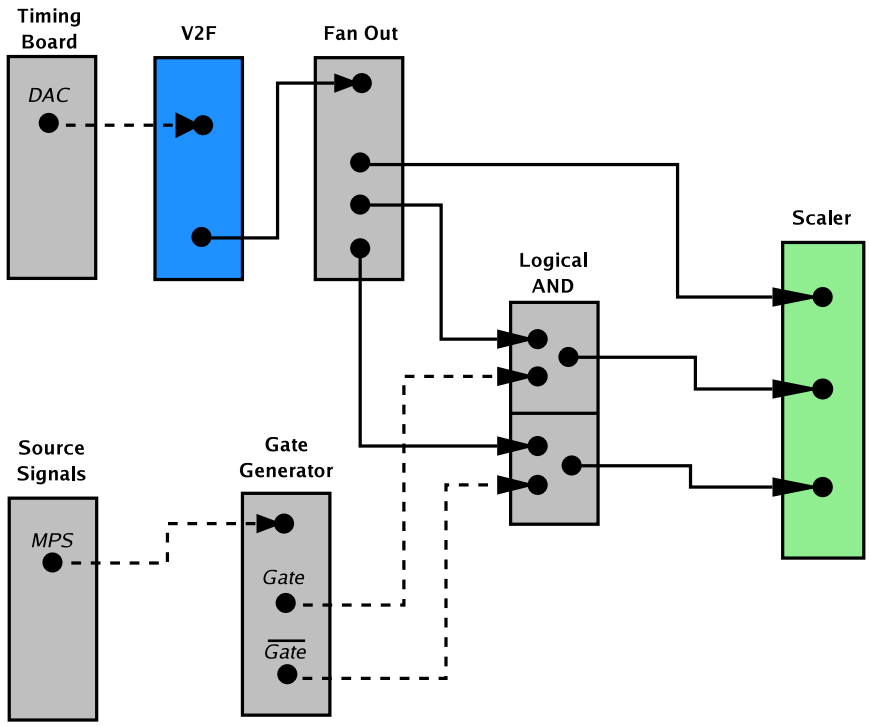

FIG. C.1: Schematic of the signal generation within the synchronization monitor.

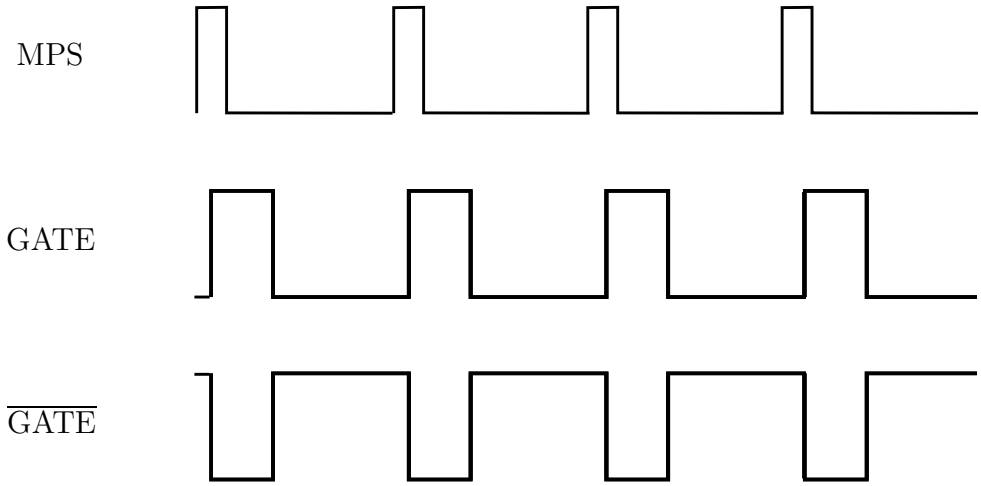

FIG. C.2: Schematic of the gating signals in the synchronization monitor.

The DAC signal from the timing board was routed to a TRIUMF voltage-to-frequency converter. The resulting frequency signal was then fanned out to the logic module containing the GATE and $\overline{\text{GATE}}$. The resulting logical AND between this frequency signal and GATE was then sent to a scaler channel, to be integrated by the HAPPEx DAQ. The same was done for $\overline{\text{GATE}}$. We refer to the GATE integrated frequency as f_1 and the $\overline{\text{GATE}}$ integrated frequency as f_2. The DAC voltage, supplied by the timing board, was changed during the DAQ readout cycle by a pseudo-random number generator. This provided an extra means of checking the window synchronization, without having to supply each crate with the helicity signal.

Each crate (Counting House, Right, and Left Spectrometer) were supplied f_1 and f_2. A reference frequency (f_r), un-gated by the logic modules, was supplied also supplied to the Counting House crate. A frequency proportional to this reference frequency (provided by an optical frequency output of the timing board) was sent to the Injector crate using optical fiber.

C.2 Analysis

A "zeroth" order check of the synchronization is performed by observing the perfect correlation between each gated signal in each crate (Figure C.3). Failure of synchronization would result in zero correlation scatter plot, and an indication that one of the crates was integrating over a different helicity window relative to another. This failure was never observed during the running of this experiment.

The next check is to insure that the integration gate lengths are the same for each crate. This is measured by comparing the sum of f_1 and f_2 with the Counting House Crate reference frequency f_r. Figure C.4 shows this comparison by plotting $(f_1 + f_2) - f_r$ (converted into μs) versus f_r. For perfect synchronization all events

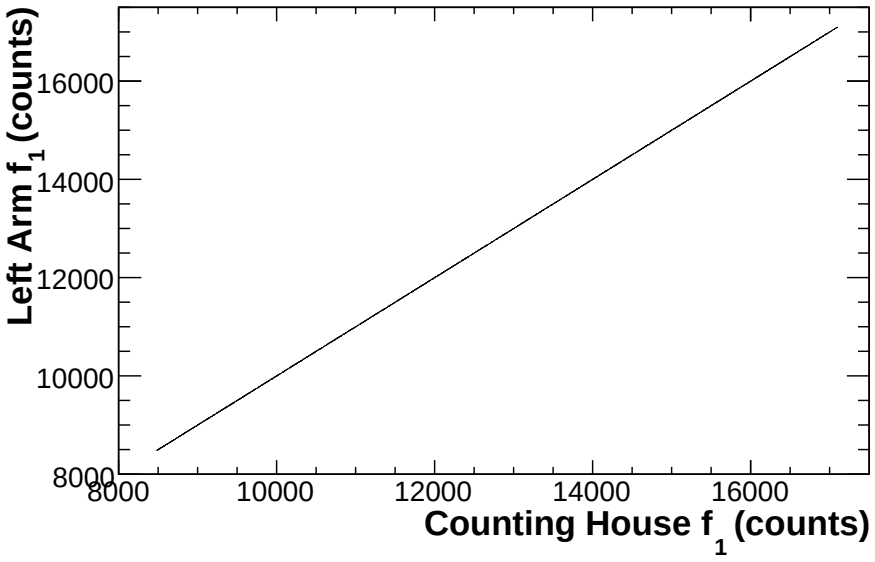

FIG. C.3: A sample plot showing a zeroth order check for DAQ synchronization. Shown is the perfect correlation between the integrated frequency pulses of f_1 as observed by the Left Arm and Counting House crates.

are located 0 μs. The $1/f_r$ dependent events off of 0 μs occur from single missed frequency pulses from either crate that lie too close to the beginning or the end of the integration gate. These expectedly converge, as the reference frequency increases.

The final check is of the relative beginning and end of the integration gate between the crates. This is simply performed, e.g. for comparing the Right Arm with the Left Arm crates, by observing the differences

$$\begin{aligned} \text{Starting time}: \quad & f_1^R - f_1^L \\ \text{Ending time}: \quad & f_2^R - f_2^L, \end{aligned} \tag{C.1}$$

shown in Figure C.5. Perfect synchronization is indicated by events located a 0 μs, with the $1/f_r$ dependent events off of 0 μs also arising from single missed frequency pulses.

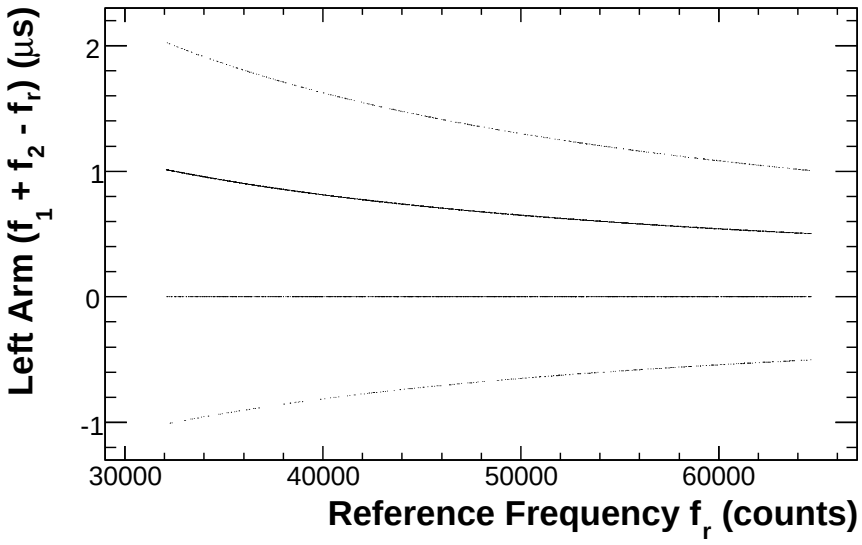

FIG. C.4: A sample plot showing a synchronization check of the difference in integration gate length between the Left Arm Crate and the Counting House Crate.

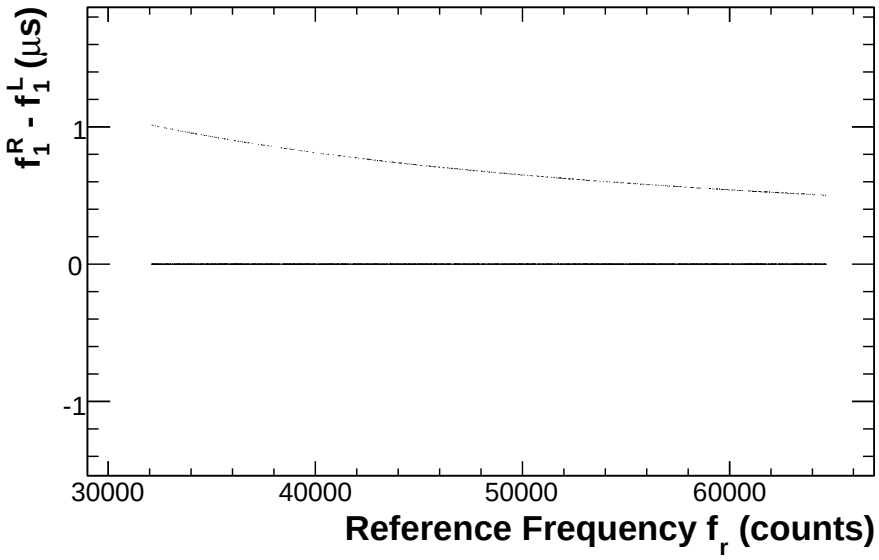

FIG. C.5: A sample plot showing a synchronization check of the difference in integration gate start times between the Right and Left Arm Crates.

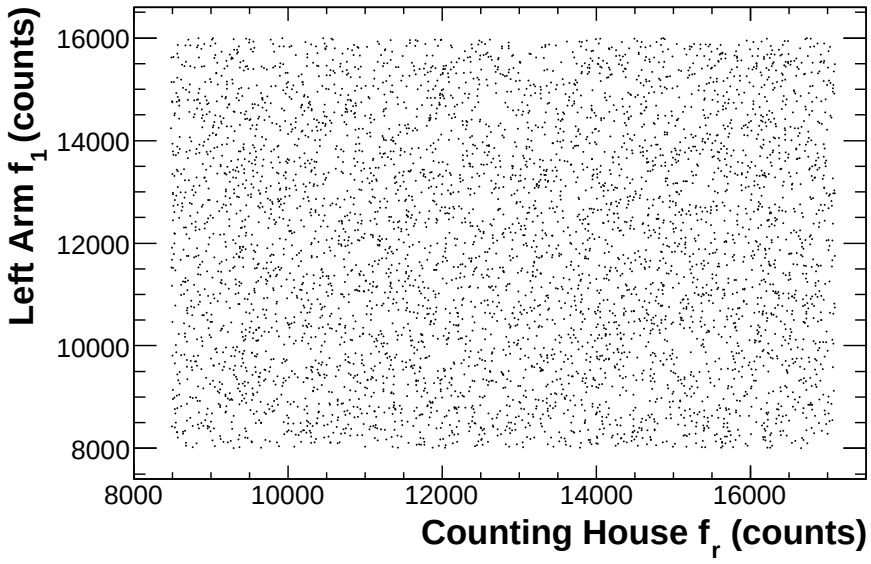

FIG. C.6: A simulated plot showing a failure in the zeroth order synchronization between the Left Arm and Counting House Crates.

C.3 Examples: When something is wrong

A simple plot of failure of the zeroth order synchronization is shown in Figure C.6. Here, there is no correlation between f_1 and the f_r. This data is simulated, since this was never observed during the running of the experiment.

A failure in the relative start time of integration gates between two crates was observed, during the commissioning of this experiment (before Production running). Figure C.7 shows an indication that the Right Arm Crate integration start time was nearly 2.5 μs later than the Left Arm Crate. The cause of this was tracked down to an unterminated BNC cable causing a reflection in the MPS signal sent to the Right Arm Crate timing board. This effectively caused a voltage distortion of this logic pulse, causing the timing board to trigger a late integration gate. This problem was remedied well before the production running of this experiment, and was never again observed.

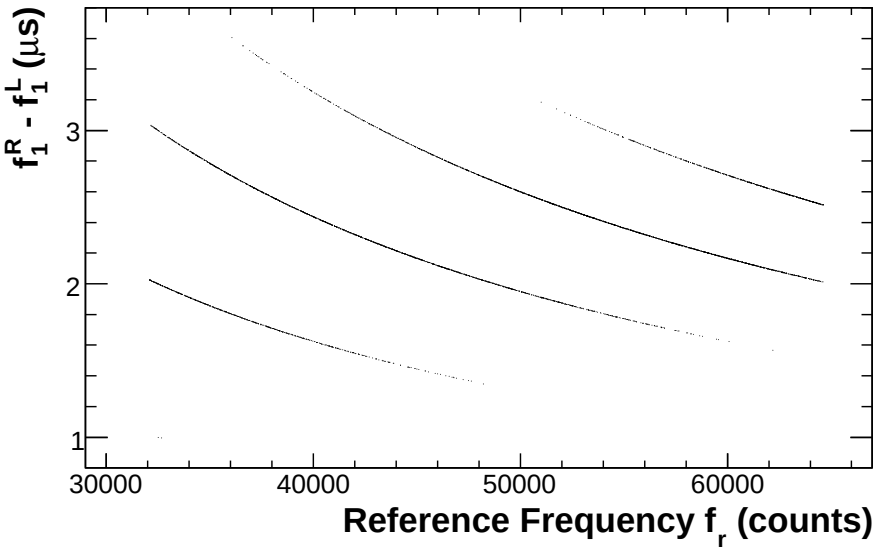

FIG. C.7: A sample plot showing a failure in the synchronization of the starting time of the integration gate between the Left and Right Arm Crates.

APPENDIX D

HAPPEx S0 Detector

As discussed in Section 3.4.2, an un-biased trigger was required to provide a clear picture of the focal plane distribution in and around the HAPPEx detector without extrapolation. This section describes the HAPPEx S0 detectors, built by the author, and their performance during the 2005 HAPPEx-^{4}He measurement.

D.1 Design and Construction

The HAPPEx S0 detector was designed to be made of inexpensive parts, easily constructed within a short time frame (during the 10 month down between the 2004 and 2005 runs of HAPPEx), and with relatively light weight so that it could be placed directly on top of a protective carbon fiber cover of the vertical drift chambers. Because the cost of a detector is usually directly proportional to its complexity, a design consisting of a single plastic scintillator sheet of dimension $0.01 \times 1.85 \times 0.25$ m^3 was chosen. Instead of the light from this scintillator being guided through a typically used acrylic light-guide, a wavelength shifter bar was used to absorb this light and re-emit it into a single photo-multiplier tube on each side of the plastic scintillator. A schematic of the S0 design is shown in Figure D.1.

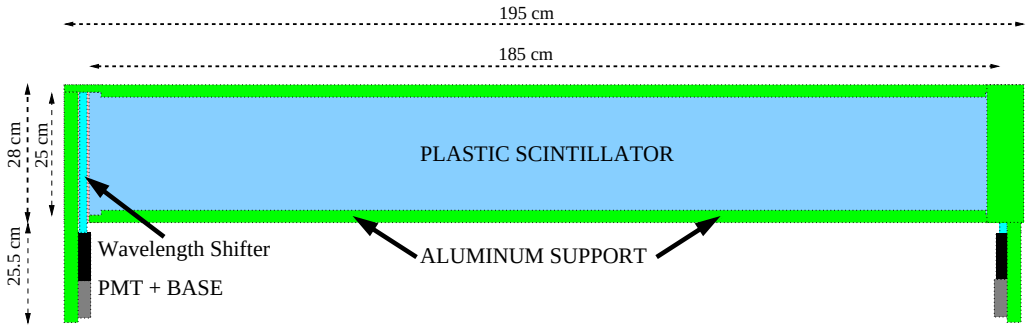

FIG. D.1: Schematic (top-view) of the HAPPEx S0 detector.

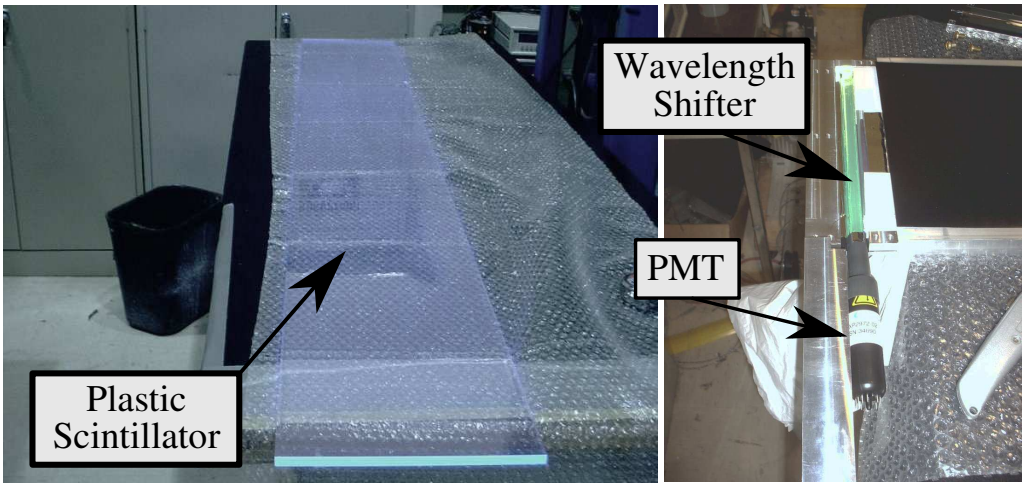

FIG. D.2: Components of the HAPPEx S0 detector.

The scintillator was supported on each of it's sides, over it's entire length, by a custom designed aluminum structure. This helped to distribute the overall weight of the detector over a larger surface area, while keeping it's main face unobstructed to reduce multiple scattering. The support structure also acted to hold the wavelength shifter bar in place, in optical contact to the plastic scintillator. The plastic scintillator (shown to the left in Fig. D.2) was of model EJ-208 from Eljen Technology. It was wrapped tightly in aluminized Mylar to ensure internal reflectivity and was padded with light cardboard to prevent it from being punctured or scratched during transport.

The wavelength shifter bar is model BC-482A from Saint-Gobain Crystals (for-

merly Bicron). One end of the bar was UV glued to the face of a 29mm diameter photo-multiplier tube (PMT model XP2972 from Photonis). Further support for this interface was made using shrink-wrap. This construction, along with a view of it's interface to the plastic scintillator, is also shown in Fig. D.2. The PMT, with it's base, was the wire-tied to the aluminum support structure.

The entire face of the detector, top and bottom, as well as the PMT was covered with a thin sheet of black vinyl that was held to the support structure with black electrical tape. This assured the entire detector to become light-tight.

D.2 Position in the spectrometer focal plane

Each HAPPEx S0 detector was installed on top of the protective carbon fiber cover of the VDCs. Precise placement of the detector was not necessary because the length and width of S0 was designed to be larger than the active area of the VDCs. Instead, the center of the short edge of the detector was aligned "by eye" with the center of the top of the VDC. The center of the long edge was aligned by extending a 45° ray from the VDC to the center of the HAPPEx detector. A photograph of the S0 placement, with respect to the HAPPEx detector and Profile Scanners [28], is shown in Fig. D.3.

D.3 Trigger Efficiency

The trigger efficiency from the HAPPEx S0 detectors was evaluated by taking a dedicated counting mode data run, where the prescale factors for each trigger were set to 1 and the focal plane was illuminated with quasi-elastic scattered electrons from ^{12}C. For each event, a ratio between S0 triggers and overlapping triggers from either the S2 plane or the HAPPEx detector. These triggers were correlated with

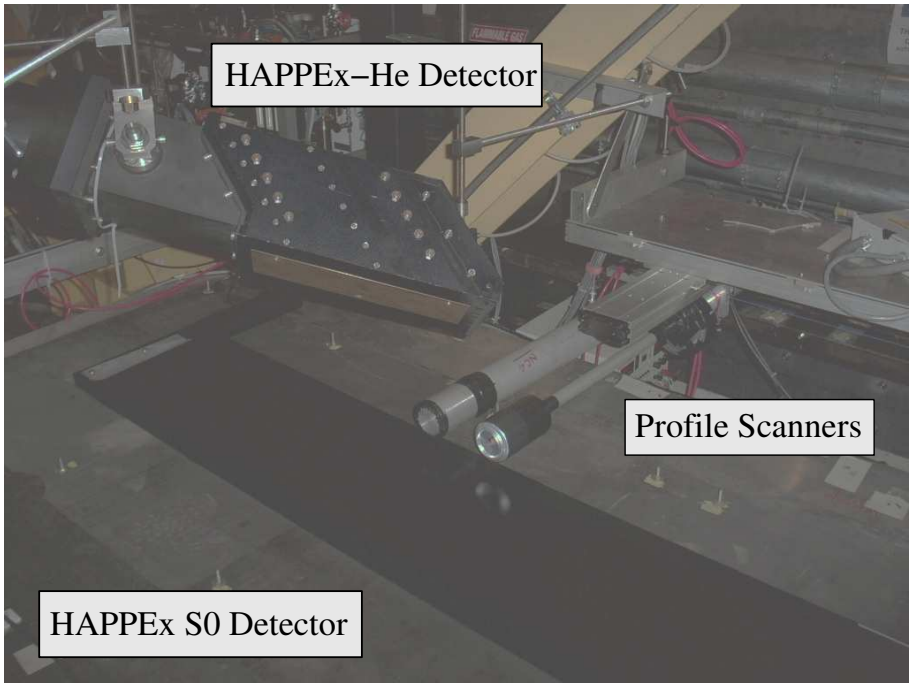

FIG. D.3: Photograph showing detector configuration during 2005 run. Profile scanners are not described in this document.

the drift chamber readout to provide the position of the track along the dispersive axis of the focal plane. Fig. D.4 shows this ratio for the HAPPEx S0 detector in each spectrometer arm as a function of this track position. Cuts to the data were made to insure that each track fell within the known acceptance of the spectrometer.

The result shows that the trigger efficiency (relative to the other focal plane trigger detectors) is very close to 1 over a majority of the length of the detector. The rise in efficiency near the center, between -0.1 m and 0.1 m, is due to the HAPPEx detector inefficiency near its own support structure (discussed in the analysis of the ^{4}He quasi-elastic background, Section 3.4.2).

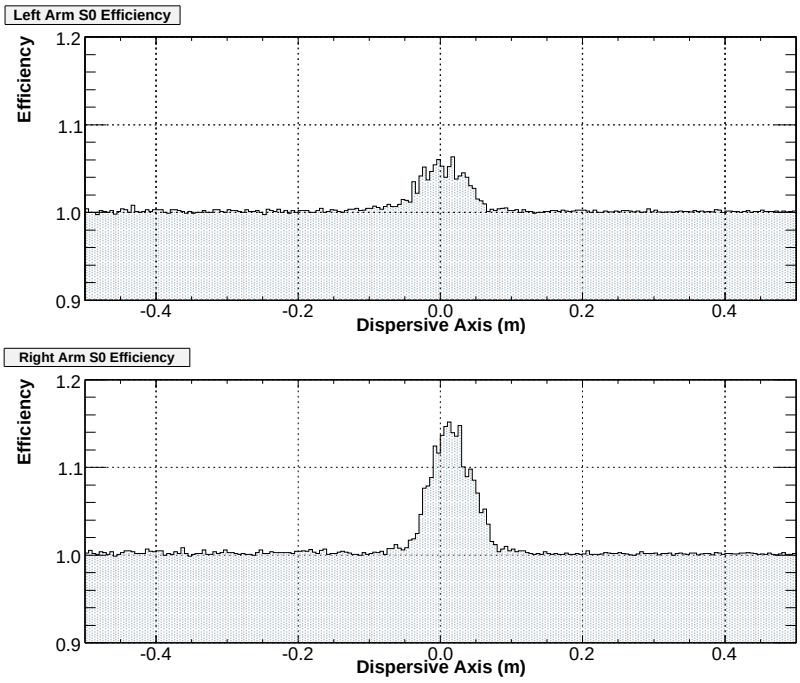

FIG. D.4: HAPPEx S0 trigger efficiency relative to the S2 trigger and HAPPEx detector trigger. Central region rise (between -0.1 m and 0.1 m) is due to the HAPPEx detector trigger inefficiency.

BIBLIOGRAPHY

[1] R. Frisch and O. Stern, Zeits. f. Physik **85**, 4 (1933).

[2] I. Estermann and O. Stern, Phys. Rev. **45**, 761 (1934).

[3] R. W. McAllister and R. Hofstadter, Phys. Rev. **102**, 851 (1956).

[4] A. O. Bazarko *et al.*, Z. Phys. **C65**, 189 (1995).

[5] A. D. Martin *et al.*, Phys. Lett. **B604**, 61 (2004).

[6] B. Adeva *et al.*, Phys. Lett. B **412**, 414 (1997).

[7] S. F. Pate, Eur. Phys. J. A **24**, 67 (2005).

[8] M. E. Sainio, Eur. Phys. J. A **24**, 89 (2005).

[9] M. M. Pavan, R. A. Arndt, R. L. Workman, and I. I. Strakovsky, , prepared for 3rd Workshop on Chiral Dynamics - Chiral Dynamics 2000: Theory and Experiment, Newport News, Virginia, 17-22 Jul 2000.

[10] J. D. Walecka, *Electron Scattering for Nuclear and Nucleon Structure* (Cambridge University Press, Cambridge, UK, 2001).

[11] R. G. Sachs, Phys. Rev. **126**, 2256 (1962).

[12] C. E. Hyde-Wright and K. de Jager, Annu. Rev. Nucl. Sci **54**, 217 (2004).

[13] S. Galster *et al.*, Nucl. Phys. **B32**, 221 (1971).

[14] J. Friedrich and T. Walcher, Eur. Phys. J. A **17**, 607 (2003).

[15] J. J. Kelly, Phys. Rev. C **70**, 068202 (2004).

[16] J. D. Walecka, *Theoretical Nuclear and Subnuclear Physics* (World Scientific Publishing Co. Pte. Ltd., Singapore, 2004).

[17] M. J. Musolf *et al.*, Phys. Rep. **239**, 1 (1994).

[18] T. W. Donnelly, J. Dubach, and I. Sick, Nucl. Phys. **A503**, 589 (1989).

[19] G. Feinberg, Phys. Rev. D **12**, 3575 (1975).

[20] S. Ramavataram, E. Hadjimichael, and T. W. Donnelly, Phys. Rev. **C50**, 1175 (1994).

[21] M. J. Musolf, R. Schiavilla, and T. W. Donnelly, Phys. Rev. **C50**, 2173 (1994).

[22] S. Eidelman *et al.*, Phys. Lett. **B592**, 1 (2004).

[23] K. A. Aniol *et al.*, Phys. Rev. C **69**, 065501 (2004).

[24] G. W. Miller IV, Ph.D. thesis, Princeton University, 2001.

[25] G. D. Cates, Eur. Phys. J. A **24**, 109 (2005).

[26] B. Humensky, L. Kaufman, and K. Paschke, Injector Beam Studies April 25-26, 2003, 2003, Internal HAPPEx Technote.

[27] T. B. Humensky *et al.*, Nucl. Instr. and Meth. **A521**, 261 (2004).

[28] L. J. Kaufman, Ph.D. thesis, University of Massachusetts, Amherst, 2007.

[29] T. Maruyama *et al.*, Appl. Phys. Lett. **85**, 2640 (2004).

[30] L. H. Thomas, Nature **117**, 514 (1926).

[31] M. Salomaa and H. A. Enge, Nucl. Instr. and Meth. **145**, 279 (1977).

[32] N. F. Mott, Proc. R. Soc. Lond. **124**, 425 (1929).

[33] J. Alcorn *et al.*, Nucl. Instr. and Meth. **A 522**, 294 (2004).

[34] M. Baylac *et al.*, Phys. Lett. B **539**, 8 (2002).

[35] N. Falletto *et al.*, Nucl. Instr. and Meth. A **459**, 412 (2001).

[36] D. Neyret *et al.*, Nucl. Instr. and Meth. A **443**, 231 (2000).

[37] J. P. Jorda *et al.*, Nucl. Instr. and Meth. A **412**, 1 (1998).

[38] K. Unser, IEEE Trans. Nucl. Sci. NS **28**, 2344 (1981).

[39] W. Barry, J. Heefner, and J. Perry, Electronic systems for beam position monitors at CEBAF, October 1990, Technical Report CEBAF-PR-90-023.

[40] W. Barry, A general analysis of thin wire pickups for high frequency beam position monitors, October 1990, Technical Report CEBAF-PR-90-024.

[41] C. Yan, N. Sinkine, and R. Wojcik, Nucl. Instr. and Meth. **A539**, 1 (2005).

[42] D. Margaziotis *et al.*, Racetrack Cells for HAPPEx.

[43] D. Armstrong, Target Fan Speed and Operating Temperature Study, 2004, http://hallaweb.jlab.org/adaq/log/html/0406_archive/040614194240.html.

[44] L. Glesener, Target Density Fluctuation Monitorring in the HAPPEX Helium Parity Violation Experiment, 2005, Internal HAPPEx Technote.

[45] P. Brindza *et al.*, IEEE Trans. Appl. Supercond. **11**, 1594 (2001).

[46] K. G. Fissum *et al.*, Nucl. Instr. and Meth. **A474**, 108 (2001).

[47] A. Vacheret and D. Lhuillier, Detector for Parity Experiments in Hall A at Jefferson Laboratory, 2002, Internal Technical Document.

[48] F. E. Maas *et al.*, Phys. Rev. Lett. **93**, 022002 (2004).

[49] F. E. Maas *et al.*, Phys. Rev. Lett. **94**, 152001 (2005).

[50] V. Gyurjyan *et al.*, (2004), presented at Computing in High-Energy Physics (CHEP '04), Interlaken, Switzerland, 27 Sep - 1 Oct 2004.

[51] R. Holmes *et al.*, Pan: The Parity Analyzer, 2006, http://physics.syr.edu/ rsholmes/happex/pan/html/index.html.

[52] R. Brun and F. Rademakers, Nucl. Instr. and Meth. **A389**, 81 (1997).

[53] N. Liyanage, Optics Calibration of the Hall A High Resolution Spectrometers using the new C++ Optimizer, 2002, Jefferson Lab TN 02-012.

[54] Data extracted from the Evaluated Nuclear Structure Data File, maintained by the National Nuclear Data Center, Brookhaven National Laboratory, Upton, NY 11973 USA, on behalf of the international Nuclear Structure Decay

Data Evaluators Network: file as of 14 February 2005; data retrieved from http://www.nndc.bnl.gov/ensdf.

[55] N. Liyanage, Spectrometer constant determination for the Hall A HRS pair, 2001, JLab - TN-01-049.

[56] T. Holmstrom, R. Feuerbach, and R. Michaels, Q^2 for HAPPEX-2, 2005, Internal Technical Document.

[57] J. K. Tuli, Nuclear Wallet Cards, 7th ed. (2005), www.nndc.bnl.gov/wallet.

[58] A. Acha *et al.*, nucl-ex/0609002 (2006).

[59] A. Vacheret, HAPPEX-2 Photo-tubes Linearity, 2003, Internal Technical Document.

[60] L. Kaufman, D. Lhuillier, and R. Suleiman, Linearity test of HAPPEx PMTs, 2005, Internal Technical Document.

[61] D. Lhuillier, Author of simulation: "gener_cone", 2003, Private Communication.

[62] D. E. Groom *et al.*, Eur. Phys. J. C **15**, 1 (2000).

[63] K. A. Aniol *et al.*, Phys. Lett. B **635**, 275 (2006).

[64] E. J. Beise, M. L. Pitt, and D. T. Spayde, Progr. Part. Nucl. Phys. **54**, 289 (2005).

[65] D. S. Armstrong *et al.*, Phys. Rev. Lett. **95**, 092001 (2005).

[66] R. Lewis *et al.*, Phys. Rev. D **67**, 013003 (2003).

[67] D. B. Leinweber *et al.*, Phys. Rev. Lett **94**, 212001 (2005).

[68] D. B. Leinweber *et al.*, Phys. Rev. Lett. **97**, 022001 (2006).

[69] N. W. Park and H. Weigel, Nucl. Phys. A **541**, 453 (1992).

[70] H. W. Hammer, U. G. Meissner, and D. Drechsel, Phys. Lett. B **367**, 323 (1996).

[71] H. W. Hammer and M. J. Ramset-Musolf, Phys. Rev. C **60**, 045204 (1999).

[72] A. Silva *et al.*, Phys. Rev. D **65**, 014016 (2001).

[73] R. Michaels, P. Souder, and R. Urciuoli, Jefferson Lab experiment 00-003.

[74] C. J. Horowitz and J. Piekarewicz, Phys. Rev. Lett. **86**, 5647 (2001).

[75] J. Bowman *et al.*, Jefferson Lab experiment 02-020.

VITA

Bryan James Moffit

Bryan James Moffit was born in Okinawa, Japan on April 4, 1976. He graduated from Horizon High School, in Scottsdale, AZ, in June 1994. After attending one year at the Colorado School of Mines, Bryan enrolled at Arizona State University in Tempe, AZ. Here, he received his B.S. in Physics in May 2000. In Fall of 2000, he enrolled in the graduate program in Physics at the College of William and Mary in Williamsburg, VA. After receiving his M.S. in December 2001, he joined the Hadronic Physics Group under the supervision of Professor David Armstrong. Bryan Moffit defended his thesis on October 11, 2006. He is currently working for the Massachusetts Institute of Technology-Laboratory of Nuclear Science as a Postdoctoral Associate at the Thomas Jefferson National Accelerator Facility in Newport News, Virginia.

ELASTIC SCATTERING OF LONGITUDINALLY POLARIZED ELECTRONS FROM ^{4}He

A measurement of G_E^s at $Q^2 = 0.1$ (GeV/c)^2

ABSTRACT

We have performed the first measurement of the parity-violating asymmetry in the elastic scattering of longitudinally polarized electrons from ^{4}He. The kinematics chosen ($Q^2 = 0.1$ (GeV/c)^2) provide a direct sensitivity to the strange electric form factor G_E^s with negligible contributions from competing effects. This experiment was performed in June 2004 and July-September 2005 in Hall A at Jefferson Lab. This work represents the experimental setup and analysis of the 2004 dataset.

The final statistical precision, from the combined datasets, put stringent requirements on the systematic errors that normalize the asymmetry (e.g. Q^2, beam polarization, backgrounds). The experimental and analysis techniques, presented in this thesis, resulted in a 12.9% relative measure of the parity-violating asymmetry for the 2004 dataset, and a 4.1% relative measure for the 2005 dataset (the most precise measurement of a parity-violating asymmetry ever obtained).

The 2004 measured result, $A^{PV} = 6.72 \pm 0.84$ (stat) ± 0.21 (syst) ppm, allows for the extraction of the electric strange form factor: $G_E^s(Q^2 = 0.1) = -0.038 \pm 0.042$ (stat) ± 0.010 (syst). When combined with results from previous experiments, at nearly the same kinematics, a clear picture of the contribution of strange quarks to the nucleon's electric and magnetic form factors emerges.

BRYAN J. MOFFIT

DEPARTMENT OF PHYSICS

THE COLLEGE OF WILLIAM AND MARY IN VIRGINIA

DAVID S. ARMSTRONG

PROFESSOR OF PHYSICS